DESIGN OF CENTRIFUGAL BLOOD PUMP

A Thesis Submitted to
the Graduate School of Engineering and Sciences of
İzmir Institute of Technology
in Partial Fulfillment of Requirements for the Degree of

MASTER OF SCIENCE

in Mechanical Engineering

by
Ceren SARIZEYBEK

December 2020
İZMİR

ACKNOWLEDGMENTS

Firstly I would like to thank my supervisor Assoc. Prof. Dr. Ünver Özkol for leading me in this thesis. I have learned to how to conduct a scientific study in a right way by him.

Dr. Sercan Acarer has helped me for a great deal with CFD studies. I thank him for his time and contributions.

My dear colleagues Nazanin Yekkelam and Serkan Erol have supported me thorough out this study. In addition, I would like to express my thanks to Özgün Özalp and Mustafa Can Yenigün for their friendship and support.

I also thank to my mother Hülya Sarızeybek, and my siblings Arda Sarızeybek, İlayda Nil Akbaba who has supported me for my decision to come back university education after four years of active work life.

Lastly a great thankful for my husband Mehmet Zaki Bilgi, who has given me courage and shared knowledge.

ABSTRACT

DESIGN OF CENTRIFUGAL BLOOD PUMP

In this thesis a centrifugal blood pump is studied numerically which will be used in ECMO systems. Pump mechanically designed to be compatible with 3D printer production and magnetic levitation will be used to drive rotor. Aim was to design a pump with 3.3 L/min at 5000 rpm having 200 mmHg head. Estimation of pump dimensions, are calculated by hand by following Igor J. KARASSIK's "Pump Handbook". These dimensions are modelled 3D by SolidWorks. This 3D model then used in ANSYS to make CFD calculations. In calculations, pump head and hydraulic pump efficiency are compared for different blade discharge angle and up-clearance. Model mesh is created by using first layer thickness inflation method for boundary layers. Meshed model than simulated by ANSYS Fluent. Realizable enhanced wall k-epsilon turbulence model is used. Blood is considered as Newtonian fluid, because expected shear rates are over 100 s^{-1} where blood viscosity remains constant according to shear rate. Fluid is defined as water to model incompressible fluid flow, but density and viscosity of fluid changed to 1060 kg/m^3 and 4.0 cP respectively to represent blood properties. At pump inlet boundary condition is given as pressure and at pump outlet boundary condition is given as mass flow. Model convergence is accepted at $1x10^{-3}$ residual. Blade discharge angle values between 20^0 and 40^0 degrees are simulated with 5^0 intervals and 35^0 is found to be the most appropriate for hydraulic efficiency and head. Likewise, six different up-clearance values between 2.0mm and 0.1mm are studied to see effect of up-clearance on head and efficiency. Up-clearance value is decided as 0.1mm to reach required head. Designed pump is found to have 198mmHg head at 3.3 L/min and 5000 rpm with 20% hydraulic efficiency for 35^0 blade discharge angle and 0.1 mm up-clearance. Also to predict hemolysis is studied at 5.8 L/min for different up-clearance values by employing Giersiepen power law hemolysis model with Lagrangian approach. Because of approach shortcomings reasonable values could not be obtained for hemolysis prediction. Designed pump is found to have 4% hemolysis for one pass.

ÖZET

SANTRİFÜJ KAN POMPASI DİZAYNI

Bu tezde ECMO sisteminde kullanılacak olan santrifüj kan pompası üzerinde nümerik olarak çalışılmıştır. Rotorun dönüşü manyetik levitasyon ile sağlanacaktır. Hidrolik tasarım kriterleri; 3.3 L/dk, 5000 rpm ve 200 mmHg basma yüksekliğidir. Pompa dizayn ölçüleri Igor J. KARASSIK'in "Pump Handbook" kitabı kullanılarak hesaplanmıştır. Pompa mekanik olarak 3D yazıcıdan çıkarılmaya uygun bir şekilde SolidWork'de tasarlanmıştır. Tasarım tamamlandıktan sonra HAD (hesaplamalı akışkanlar dinamiği) yapabilmek için ANSYS kullanılmıştır. Hesaplamalarda, farklı çıkış kanat açıları ve üst boşluk mesafesi (üst salyangoz ve kanat tepesi arasındaki mesafe) değiştirilerek pompa basma yüksekliği ve hidrolik pompa verimliliği karşılaştırılmıştır. First layer thickness inflation metodu kullanılarak mesh atılmış ve simülasyon için ANSYS Fluent'e yüklenmiştir. Buradaki hesaplamalarda realizable enhanced wall k-epsilon türbülans modeli kullanılmıştır. ANSYS Fluent'de akışkan tanımı su olarak seçilmiş fakat yoğunluğu ve viskozitesi, kanın özelliği olan 1060 kg/m^3 ve 4 cP olarak değiştirilmiştir. Giriş sınır koşulu olarak basınç, çıkış sınır koşulu olarak kütlesel debi verilmiştir. Sonuçlar 1x10^{-3} yakınsaklığına ulaşıldığında alınmıştır. Çıkış kanat açısı 20^0'den 40^0'ye kadar 5^0 arttırılarak denenmiş ve 35^{0}lik kanat çıkış açısının, pompa yüksekliği ve hidrolik verim açısından en uygun olduğu gözlenmiştir. Sonraki aşamada 35^{0}lik çıkış açısına sahip pompa için 2.00 mm'den 0.10 mm'ye kadar 6 farklı üst boşluk mesafesi için denemeler yapılmıştır. Bu denemeler sonucunda 0.10 mmlik üst boşluk mesafesi olan pompanın istenen basma yüksekliğine ulaştığı gözlenmiş ve bu sebeple 0.1mmlik pompa dizaynı çalışma için uygun görülmüştür. Sonuç olarak; kanat çıkış açısı 35^0 ve üst boşluk mesafesi 0.10 mm olarak dizayn edilen pompa 5000 rpm'de 3.3 L/dk akış debisinde %20lik bir hidrolik verimlilik ile 198 mmHg basma yüksekliğine ulaşmaktadır. Ek olarak, farklı up-clearance değerleri için Giersiepen kuvvet yasası kullanılarak hemoliz hesabı yapılmıştır. Bu hesaplamada Lagrangian yaklaşımı uygulanmıştır. Seçilen pompada hemoliz değeri bir geçiş için %4 olarak bulunmuştur.

TABLE OF CONTENTS

LIST OF FIGURES……vii

LIST OF TABLES……xi

NOMENCLATURE……xii

CHAPTER 1. INTRODUCTION……1

1.1. Basic Concepts……1

1.2. Purpose of the Study……2

1.3. Outline of the Thesis……3

CHAPTER 2. LITERATURE SURVEY……4

2.1. Cardiovascular System……4

2.2. General Information of Blood……6

2.3. Blood Rheology……8

2.4. Movement of RBCs……11

2.5. Blood Damage……12

2.6. Pump Types……14

2.7. History of Blood Pumps……17

2.7.1. Early Pumping Devices for Blood……17

2.7.2. First Generation VADs (1965-1990) ……18

2.7.3. Second Generation VADs (1990-2000) ……20

2.7.4. Third Generation VADs (2000-present) ……20

2.8. Blood Pump Types……23

CHAPTER 3. CENTRIFUGAL PUMP DESIGN……27

3.1. Pump Sizing……27

3.2. Designed Pump Shape Considerations……39

CHAPTER 4. CFD Modelling……41

CHAPTER 5. CFD Results & Discussion……...……51

REFERENCES……..……..…69

APPENDICES……...……..…75
APPENDIX A. CALCULATION FOR DESIGN……...…….……75
APPENDIX B. MESH STRUCTURE……..…...78
APPENDIX C. PRESSURE & VELOCITY PROFILES FOR DIFFERENT β_2…...…...79
APPENDIX D. PRESSURE & VELOCITY PROFILES FOR DIFFERENT
UP-CLERANCES……..…83

LIST OF FIGURES

Figure **Page**

Figure 1.1. Number of deaths by cause, World, 2017……...2
Figure 1.2. Number of deaths by cause, Turkey, 2017……..2
Figure 2.1. Structure of heart and blood circulation in heart…….5
Figure 2.2. Certain vessels in cardiovascular system……..…..5
Figure 2.3. Representation of shear stress and shear rate in 2D……5
Figure 2.4. Top view and cross section of RBC……7
Figure 2.5. Rouleaux formation…….7
Figure 2.6. Visualization of aggregation……...…9
Figure 2.7. Human blood viscosity vs shear rate for 45% hematocrit at 37 ^{0}C……...10
Figure 2.8. Human blood viscosity vs shear rate for different hematocrit……..……10
Figure 2.9. Human blood viscosity vs shear rate for different temperature……11
Figure 2.10. Tank-treading motion of an RBC in shear flow……..12
Figure 2.11. RBC deformation in shear flow……..12
Figure 2.12. Different hemolysis model and experimental result for different shear rate for 7200s…….14
Figure 2.13. Classification of pumps……...15
Figure 2.14. Basic reciprocating pumps design……...15
Figure 2.15. Basic rotary pumps design……..16
Figure 2.16. Basic centrifugal pumps design ……..…16
Figure 2.17. Pioneer of today's heart-lung machine……...17
Figure 2.18. Electrical pendular cock developed by Hammel (1889)…….18
Figure 2.19. Left-, right- and biventricular assist devices……...19
Figure 2.20. Heartmate XVE LVAS - example of first generation LVADs……...…19
Figure 2.21. Second Generation VADS (a)Eveheart (b)Jarvik 2000……..20
Figure 2.22. Spiral groove bearing profile……..21
Figure 2.23. Passive magnetic bearing with permanent magnets……21
Figure 2.24. Blood pump with hydrodynamic levitation…….22
Figure 2.25. Maglev centrifugal pump……22

Figure **Page**

Figure 2.26. Active magnetic bearings……22
Figure 2.27. Simple sketch of TAH……23
Figure 2.28. Simple sketch of VADs (a) Extracorporeal VADs
(b)Intracorporeal VADs……..24
Figure 2.29. Simple sketch of two different percutaneous methods for
VADs treatment (a)Venovenous type (b)Venoarterial type……...24
Figure 2.30. Number of implant VADs between 2006 and 2014, reported
in INTERMACS database……...26
Figure 3.1. Impeller design for different specific speed……..28
Figure 3.2. Impeller discharge angle vs specific speed……...29
Figure 3.3. Hydraulic efficiency vs volumetric flow rate of PediVAS
compared with CentriMag pump systems……29
Figure 3.4. c_{m3}/u_2 vs N_{sm}……..30
Figure 3.5. Velocity triangles……..31
Figure 3.6. Impeller cross-section……...31
Figure 3.7. Schematic illustrating r_1 measurement……..33
Figure 3.8. Drawing of single blade by using single arc method……35
Figure 3.9. C_{thr}/u_2 vs N_{sm}……36
Figure 3.10. Cross-sectional area of 3D centrifugal pump from SolidWorks……37
Figure 3.11. Volute casing……...38
Figure 3.12. Volute casing from SolidWorks……..38
Figure 3.13. Upper and lower volutes……39
Figure 3.14. Rotor height and radius……...40
Figure 3.15. Lower volute height and diameter……...40
Figure 3.16. (a) Pump section view (b) Suction and discharge radius……40
Figure 4.1. 2D interface drawing in Ansys SpaceClaim……41
Figure 4.2. 3D isometric and cross-sectional view of interface in Ansys
DesignModeler……42
Figure 4.3. Schematically equilateral cell……..….42
Figure 4.4. Representation of y^+ in 2D……43
Figure 4.5. U^+ vs y^+……44

Figure **Page**

Figure 4.6. Inlet and outlet boundary conditions……45
Figure 4.7. Models in ANSYS fluent……..……46
Figure 4.8. Comparison of experimental and SST k-omega numerical pressure head of the pump……48
Figure 4.9. Comparison of experimental and SST k-omega numerical pressure head of the pump……48
Figure 4.10. Comparison of experimental and enhanced k-epsilon numerical pressure head of the pump……..……49
Figure 5.1. Head vs Q for different β_2……...……..51
Figure 5.2. Efficiency vs Q for different β_2……52
Figure 5.3. Head vs Q for different up-clearance……53
Figure 5.4. Efficiency vs Q for different up-clearance……53
Figure 5.5. Stationary wall shear stress for different up-clearance for 35^0 β_2 at 5.8 L/min……...55
Figure 5.6. Rotating wall shear stress for different up-clearance for 35^0 β_2 at 5.8 L/min……...57
Figure 5.7. Scalar shear stress of all domain for different up-clearance for 35^0 β_2 at 5.8 L/min……..….59
Figure 5.8. Particle time population distribution for different up-clearance for 35^0 β_2 at 5.8 L/min……62
Figure 5.9. D-index population distribution for different up-clearance for 35^0 β_2 at 5.8 L/min……...63
Figure 5.10. Scalar shear stress on particle path lines for 35^0 β_2 at 5.8 L/min for 0.10 mm up-clearance……64
Figure 5.11. Iso-contour higher than 250 Pa for 35^0 β_2 at 5.8 L/min for 0.10 mm up-clearance……64
Figure 5.12. Trimmed inlet and outlet of pump……..65
Figure 5.13. Particle time population distribution for different particle number for 35^0 β_2 at 5.8 L/min……66

Figure **Page**

Figure 5.14. D-index population distribution for different particle number for 35^0 β_2 at 5.8 L/min……66
Figure 5.15. Particle time population distribution for different up-clearance for 35^0 β_2 at 5.8 L/min (200 particles)… ……67
Figure 5.16. D-index population distribution for different up-clearance for 35^0 β_2 at 5.8 L/min (200 particles)……68
Figure B.1. Mesh structure from top view……...78
Figure B.2. Mesh structure from side view……78
Figure C.1. Pressure profiles for different β_2 for up-clearance 2.00 mm at 5.8 L/min……...79
Figure C.2. Velocity profiles for different β_2 for up-clearance 2.00 mm at 5.8 L/min……..81
Figure D.1. Pressure profiles for different up-clearance for 35^0 β_2 at 5.8 L/min……83
Figure D.2. Velocity profiles for different up-clearance for 35^0 β_2 at 5.8 L/min……85

LIST OF TABLES

Table **Page**

Table 2.1. Wall shear rates in different vessels……6
Table 3.1. Parameters to design blade shape……..34
Table 5.1. P_{shaft} and P_{fluid} for different up-clearence at 5.8 L/min and 35^0 β_2……54
Table 5.2. Average scalar shear stress, particle time and D-index for different up-clearance for 350 β2 at 5.8 L/min…….63
Table 5.3. Average scalar shear stress for different up-clearance for 35^0 β_2 at 5.8 L/min (trimmed case)……...65
Table 5.4. Particle time and D-index for different up-clearance for 35^0 β_2 at 5.8 L/min (200 particles)……68
Table A.1. Design Parameters……75
Table A.2. Results for drawing volute……77

NOMENCLATURE

Symbol	Description	Unit
A_1	inlet area between blades	mm^2
A_2	discharge area between blades	mm^2
A_{sp}	spiral area	mm^2
A_{thr}	throat area	mm^2
A_v	volute area	mm^2
b_2	discharge impeller width	mm
c_{m0}	theoretical meridional velocity of impeller eye	m/s
c_{m3}	theoretical meridional velocity of impeller discharge	m/s
c_{thr}	throat velocity	m/s
c_{u3}	theoretical peripheral component velocity of impeller discharge	m/s
c'_{u3}	absolute peripheral component velocity of impeller discharge	m/s
D_1	impeller eye diameter	mm
D_2	impeller discharge diameter	mm
D_H	hub diameter	mm
D_S	suction diameter	mm
g	gravity acceleration	9.81 m/s^2
H	total head	mmHg or m-blood
H_{Hg}	height of mercury	mmHg
H_{blood}	height of blood	m-blood
k	hub ratio	-
N	angular velocity	rpm
N_{sm}	specific speed in SI unit	-
$NPSH_R$	net positive suction head-required	m
P	pressure	Pa
Q	volumetric flow rate	m^3/s
r_1	impeller eye radius	mm
r_{1m}	mean inlet radius	mm

r_2	impeller radius	mm
r_4	distance of the throat center from the impeller center	mm
r_H	hub radius	mm
r_{thr}	throat radius	mm
s_1	inlet blade thickness	mm
s_2	discharge blade thickness	mm
t	tongue clearance	mm
u_1	peripheral speed of impeller eye	m/s
u_2	peripheral speed of impeller discharge	m/s
v	fluid velocity	m/s
z	blade number	-
β_0	flow angle	degree
β_1	blade inlet angle	degree
β_2	blade discharge angle	degree
η	hydraulic efficiency	%
μ	slip factor	-
ρ_{blood}	density of blood	g/cm^3
ρ_{Hg}	density of mercury	g/cm^3
φ_v	central angle	degree
ψ	head coefficient	-

CHAPTER 1

INTRODUCTION

1.1. Basic Concepts

When making a health plan, governments consider the cause of mortality statistics and give priority accordingly. Since last 15 years, heart failure, also called cardiovascular disease, has been the first cause of death in the world [1]. This is clearly shown in Figure 1.1 which shows number of deaths by cause globally in 2017. Also, cardiovascular diseases leading cause of death in Turkey as it is demonstrated in Figure 1.2. According to World Health Organization (WHO), annually 23.6 million people will die by 2030 because of cardiovascular disease [2]. Therefore; studies of cardiovascular treatments have been increasing rapidly.

Today's world with technological advances, heart transplant can be done successfully. However, the main problem of heart transplant is to find suitable donor. Firstly, size of heart and blood group must match. Generally, waiting time for a suitable donor lasts more than six months. Most of patients die when waiting for a donor. To support or cure patients in this period, ventricular assist devices (VADs) are used. The most important part of VAD is blood pump.

Blood pump is also used in extracorporeal membrane oxygenation (ECMO), which is one of the mechanical circularity support device. It is used during or after surgery for patients who need to support for heart and lungs. First deoxygenated blood is pumped to outside of body and blood is oxygenated in membrane of ECMO. Then, oxygenated blood pumped back to body. This process helps to increase surgery success and patients heal more quickly by using ECMO.

As it is seen above, blood pumps are used in diverse applications and crucial for cardiovascular treatments. These pumps should be disposable and simple to produce. However, design of blood pump should be done precisely because of blood structure. Specially, parameters that damage blood like turbulence, stagnation point and high shear stress should be minimized to prevent excessive damage.

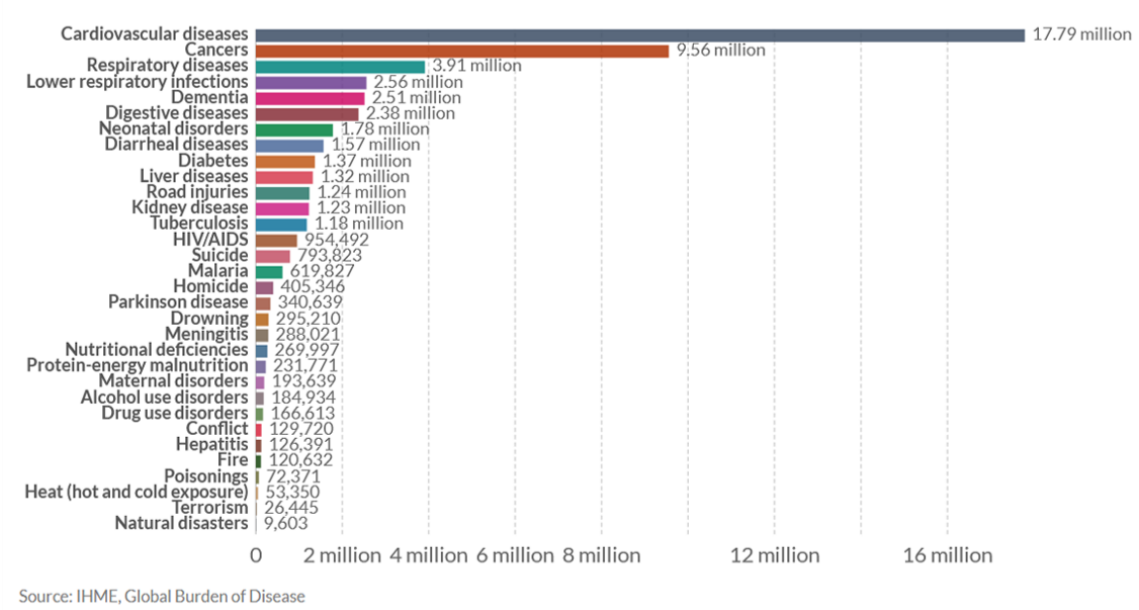

Figure 1.1. Number of deaths by cause, World, 2017 [3]

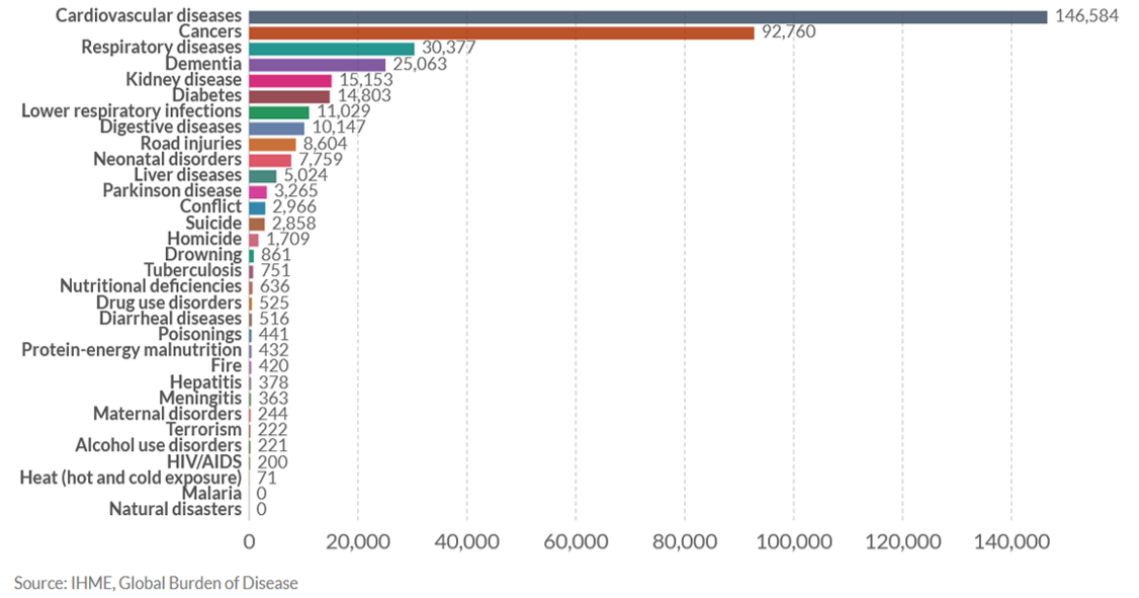

Figure 1.2. Number of deaths by cause, Turkey, 2017 [3]

1.2. Purpose of the Study

In this study, a centrifugal blood pump is designed for the use in a ECMO device. The pump is used externally and runs with magnetic levitation. It is used during or after surgery to support heart or lungs. Therefore, operating time for this pump is maximum 7

days for a patient. The main aim of this study is to design a centrifugal type blood pump which has minimum effect on blood damage. In this thesis, preliminary design of pump is done and CFD calculations are employed. By comparing with head and hydraulic efficiency for different designs, pump dimensions are determined. Blood damage analysis based on scalar shear stress is also investigated for different up clearance values.

1.3. Outline of the Thesis

After stating purpose of this study and giving a brief introduction in Chapter 1, literature research done for this study is given in Chapter 2. Information about blood structure, hemolysis conditions are stated. Also brief information about pump types and blood pump applications are given chronological. Their advantages and disadvantages are mentioned. In Chapter 3, pump is sized by hand calculation and details of this calculation are given. Also an example calculation is made in Appendix A. Next, in Chapter 4, CFD modelling logics, used software and methodology is given. Also, turbulence models are briefly discussed. In chapter 5 CFD results are stated and evaluated.

CHAPTER 2

LITERATURE SURVEY

2.1. Cardiovascular System

Cardiovascular systems include heart, blood vessels and blood. As it is known heart is the center of cardiovascular system. It acts as a pump, that have four chambers. Four chambers, four valves, aorta, pulmonary artery and blood circulation in heart are shown in Figure 2.1. These chambers are right atrium (RA), right ventricle (RV), left atrium (LA) and left ventricle (LV). RA receives deoxygenated blood. Then, blood is send to RV for carrying deoxygenated blood to lungs by pulmonary (related with lungs) artery. Blood is re-oxygenated in lungs and LA receives oxygenated blood. Later, blood moves to LV for carrying oxygenated blood to tissues, organs and muscles by aorta veins, which is the main artery. There are also check valves to prevent backflow and mixing of oxygenated-deoxygenated blood. These valves are pulmonary, tricuspid, mitral and aortic valves [4].

Heart rates, or pulse, range 60 to 100 beats per minute for healthy adults. Every beats increases pressure. Increased pressure during heartbeat, is called as systolic pressure. Between two beats heart rests, and remaining pressure is called as diastolic . For healthy adults, systolic and diastolic blood pressure are 120 and 80 mmHg, respectively [5].

Cardiovascular system consists of vessels with many different diameters, given basically in Figure 2.2. When blood passes through these veins, it is exposed to different levels of shear rate as given in Table 2.1, these values are given approximately for 5 L/min which is a normal blood flow rate for a 70 kg healthy adult at rest [7]. Basically shear rate defined as velocity difference between adjacent layers of flow, schematically given in Figure 2.3 represented as $\frac{du}{dz}$.

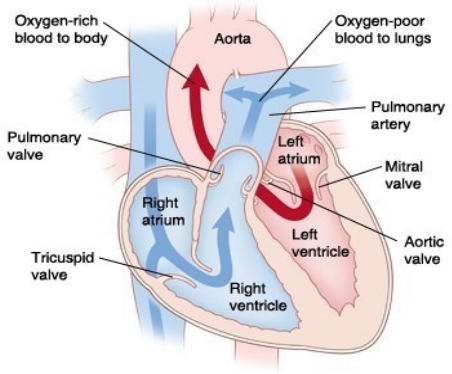

Figure 2.1. Structure of heart and blood circulation in heart [6]

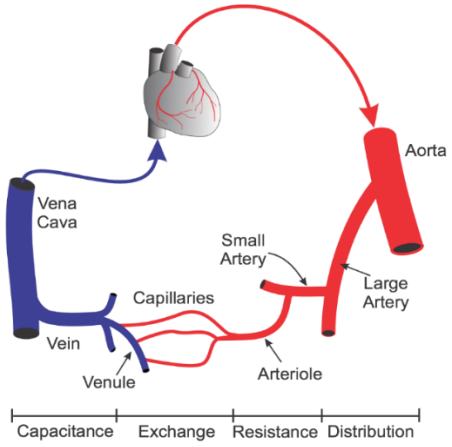

Figure 2.2. Certain vessels in cardiovascular system [8]

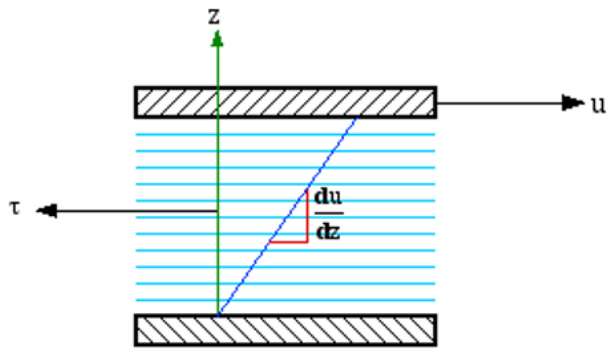

Figure 2.3. Representation of shear stress and shear rate in 2D [9]

Table 2.1. Wall shear rates in different vessels [10]

Structure	Diameter (cm)	Wall shear rate (s^{-1})
Aorta	1.0	400
Large arteries	0.3	525
Small arteries	0.1	640
Arteriole	0.002	1200
Capillaries	0.0005	-
Venule	0.003	187
Small veins	0.24	50
Large veins	0.6	48
Vena Cava	1.25	211

2.2. General Information of Blood

Blood is the most vital fluid for animals in general, that carries oxygen, nutrients, hormones, vitamins and antibody to the tissues and removes waste materials from the body. Human blood constitutes approximately 7-8% of total body weight [11] and it corresponds to about 4.5-6 liters.

Blood is a mixture of 55% plasma and 45% formed element by volume. Formed elements consist of red blood cells (erythrocytes), white blood cells (leukocytes), and platelets (thrombocytes).

Red blood cells (RBCs) make up about 99% of formed elements. They have diameter of 7-8 μm and their biconcave shape as it is illustrated in Figure 2.4. Also, they usually aggregate as rouleaux that is shown in Figure 2.5. Oxygen is carried by hemoglobin protein that present in cytoplasm of RBC. Approximately 300 million hemoglobin exist in a RBC [12]. The surface area to volume ratio of normal RBC is 40%. The ratio is greater than sphere that has same volume. Therefore, oxygen diffuses to RBCs easily [13]. In fact, 98% of oxygen going in to cells is carried by RBC and only 2% of oxygen is carried by plasma [14]. RBCs lifespan is approximately 115 days [15]. White blood cells defend body to viruses, bacteria, and other invaders. Its form is roughly spherical, and its lifespan range is from 13 to 20 days [16]. Platelets on the other hand is

used to stop bleeding. It is not exactly a cell, but only fragments of a cell. Platelets shape can be oval or rounded and their life span can range from 5 to 10 days [17].

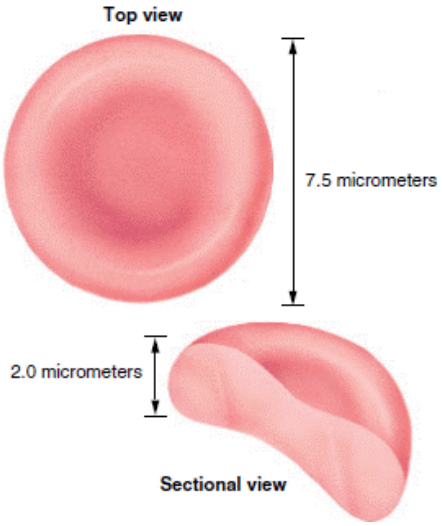

Figure 2.4. Top view and cross section of RBC [18]

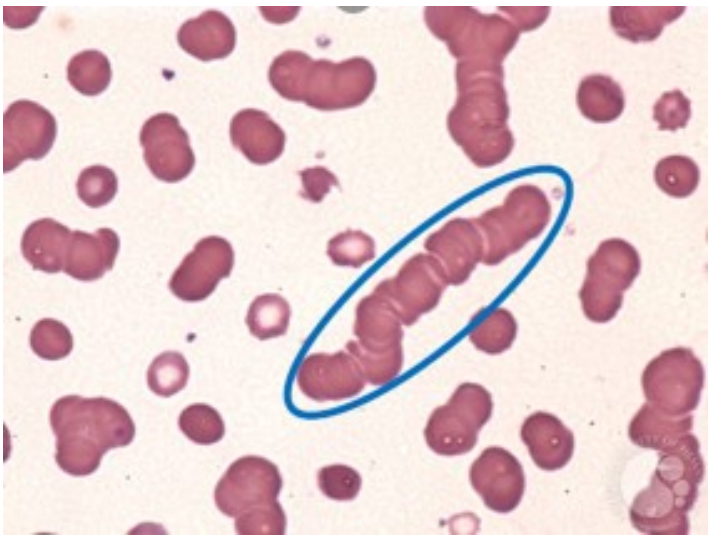

Figure 2.5. Rouleaux formation [19]

2.3. Blood Rheology

Fluid rheology branches into two main subgroups as Newtonian and non-Newtonian according to relation between shear stress and shear rate. For Newtonian fluids, shear stress increases linearly by increasing shear rate. Remembering that ratio of shear stress to shear rate is known as the fluid's viscosity, Newtonian fluids viscosity is independent of shear rate. On the contrary, viscosity of non-Newtonian fluids monotonically changes with respect to shear rate. Non-Newtonian fluids also branches subgroups as seen below.

1. **Time independent**
    - **a.** Pseudoplastic fluid's (a.k.a shear thinning fluids) viscosity decreases with shear rate. Simple viscosity model of blood is classified as pseudoplastic.
    - **b.** Dilatant fluid's (a.k.a shear thickening fluids) viscosity increases with shear rate.
    - **c.** Bingham fluids have viscoplastic properties which means at low shear rate, rigid body, at high shear rate, viscous flow are observed.

2. **Time dependent**
    - **a.** Thixotropic fluid's viscosity decreases with shear rate and are reversible with time.
    - **b.** Rheopectic fluid's viscosity increases with shear rate and are reversible with time.

3. **Viscoelastic fluid:** It has both fluid and elastic properties at the same time. Polymeric suspensions can be given as an example.

Blood is a complex fluid because of its suspension form. According to applied shear rate, its structure and therefore, it is rheological behavior changes. This characteristic makes blood a Non-Newtonian fluid. To understand effect of mechanical loading on the blood, fluid behavior should be known under specific conditions.

Therefore, we should take a closer look at some of the characteristic shear rate ranges where important structural changes occur in the blood.

- **Less than 10^{-3} s^{-1}**: In this region, shear stress can be regarded below yield stress [20]. Therefore; blood behaves like solid, so rheological state equation can't be applied. If applied stress is more than yield stress, continuous viscous flow will be observed.

- **Between 10^{-3} and 100 s^{-1}:** RBCs have a flexible structure that changes by mechanical, thermal, and chemical effects. If the shear rate increases, aggregated rouleaux structure of RBC breakup into individual cells as it is demonstrated in Figure 2.6. Because of this, viscosity of blood decreases and rheological behavior changes to viscoelastic, thixotropic and pseudoplastic until shear rate reaches to 100 s^{-1} [21].

- **Higher than 100 s^{-1}:** Despite increasing shear rate, structural changes of RBC is minimal and therefore, its viscosity does not show a significant change anymore in this region. As a result of this, blood can be modeled like Newtonian fluid at higher than 100 s^{-1} shear rate [22]. Because, erythrocytes completely separated and independently moving.

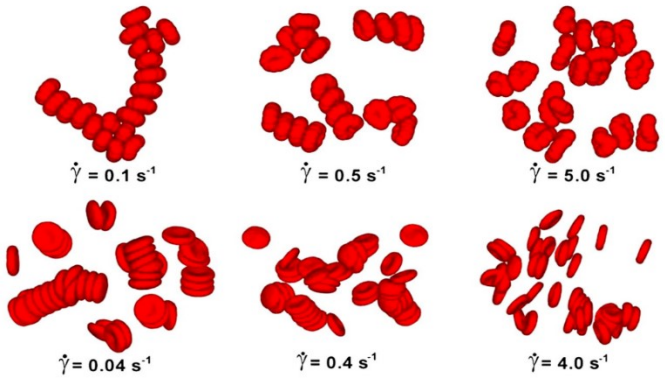

Figure 2.6. Visualization of aggregation [23]

Blood viscosity is effected not only by shear rate but also temperature, macro rheological factors such as plasma viscosity and hematocrit, micro rheological factors such as aggregation, erythrocyte deformability and activity of platelets, etc [24].

Hematocrit, which shows volume of RBC over volume of total blood, alters from 40% to 45% for healthy human blood [13]. According to experimental study, when shear rate is higher than 100 s^{-1}, viscosity of blood, shows Newtonian fluid properties, ranges between 3.5-5 cP (mPa.s), for %45 hematocrit at 37 ^{0}C as it is indicated in Figure 2.7.

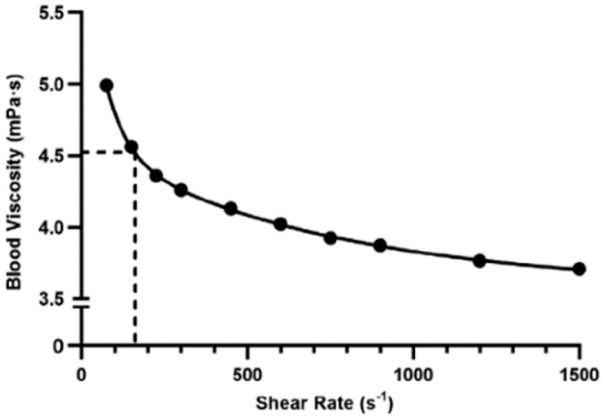

Figure 2.7. Human blood viscosity vs shear rate for 45% hematocrit at 37 ^{0}C [25]

Blood viscosity increases in directly proportional to hematocrit and inversely proportional to temperature. However, when shear rate is over 100 s^{-1}, these variations with respect to temperature and hematocrit can be negligible as shown in Figure 2.8 and Figure 2.9.

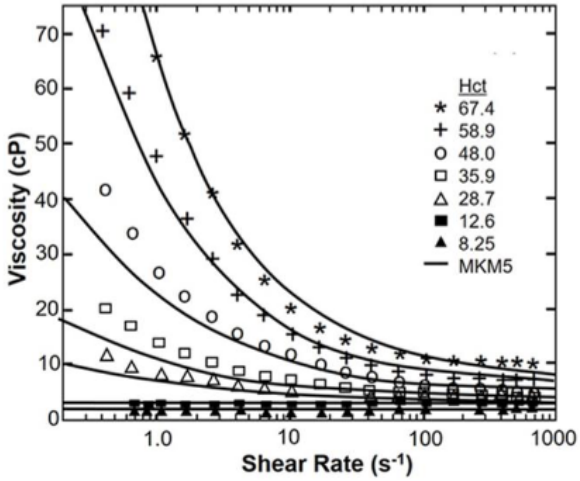

Figure 2.8. Human blood viscosity vs shear rate for different hematocrit [26]

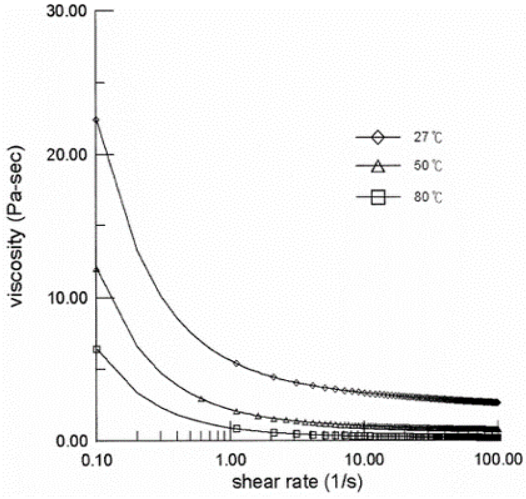

Figure 2.9. Human blood viscosity vs shear rate for different temperature [27]

2.4. Movements of RBCs

There are two characteristics motions of RBCs under shear flow, known as tumbling and tank-treading motion. Whole RBC rotates like rigid body in tumbling motion. Tumbling motion is observed if shear rate is less than 10 s^{-1} and tank-treading motion is observed for shear rates greater than 10 s^{-1} [28]. In tank-treading motion, membrane rotates around the mass center of RBC [29] as illustrated in Figure 2.10. During tank-treading motion, membrane is deformed in shape. However, RBCs revert to their resting biconcave shape when shear rate is decreased. This elastic structure provides reversible deformation until 6% of areal strain, which is ratio of increased area after deformation to original area [30]. Areal strain can be calculated with Eq.2.1. given below where ϵ_{xx}, ϵ_{yy} represents normal strain and ϵ_{xy}, ϵ_{yx} represent shear strain. Normal strain is calculated with Eq. 2.2 and shear strain is calculated by Eq. 2.3.

$$\epsilon_{areal} = \begin{bmatrix} \epsilon_{xx} & \epsilon_{xy} \\ \epsilon_{yx} & \epsilon_{yy} \end{bmatrix} \quad (2.1)\ [31]$$

$$\epsilon_{xx} = \frac{\Delta L}{L_0} = \frac{\partial u_x}{\partial X}, \quad \epsilon_{yy} = \frac{\partial u_y}{\partial Y} \quad (2.2)\ [31]$$

$$\epsilon_{xy} = \epsilon_{yx} = \frac{1}{2}\left(\frac{\partial u_y}{\partial X} + \frac{\partial u_x}{\partial Y}\right) \quad (2.3)\ [31]$$

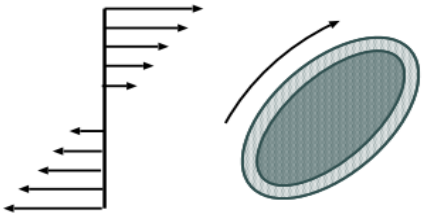

Figure 2.10. Tank-treading motion of an RBC in shear flow [32]

2.5. Blood Damage

When shear rate approaches to zero RBCs create rouleaux form. When shear rate increases, rouleaux form disperses and monodispersed RBCs begin to move with tumbling motions in biconcave shape. As shear rate continuous to increase, RBC changes shape to ellipsoidal and moves in tank-treading motion. If shear rate increases more, RBC expose to irreversible deformation and pores formed on the RBC's membrane. The process is clearly shown in Figure 2.11.

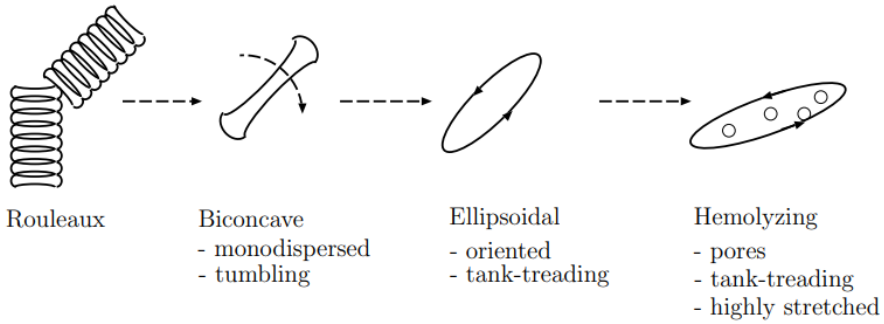

Figure 2.11. RBC deformation in shear flow [32]

After 6% areal strain limit, corresponding to 42000 s^{-1}, RBCs are damaged irreversibly at this region [30]. Hemoglobin leaks from RBCs to plasma through pores on the surface which are created because of high shear rate. This type of blood damage is called as **hemolysis**. Hemoglobin which exist in plasma, is called as free hemoglobin. Free hemoglobin can be removed from blood by kidneys easily because of its tiny size. Free hemoglobin also increases viscosity and colloidal osmotic pressure of blood. Normally human blood consists approximately 0.05 g/L free hemoglobin [33]. This free hemoglobin comes from natural rupture of RBCs after 115 days.

There are two main models to predict hemolysis analytically, strain based and stress based. Strain based models try to predict deformation of RBC membrane which results hemoglobin leak to plasma as stated above. Stress based models are originates from experimental data and because of that they are also called empirical model. Experiments are carried out with constant shear rates and increase in free hemoglobin is measured for various shear rates and exposure times. Stress based models are commonly employed as power laws because of their easy approach. Power law model is given in Eq. 2.4 where D is damage index indicating ratio of leaking hemoglobin to total hemoglobin, t is exposure time in seconds and $\bar{\tau}$ is scalar shear stress in Pa. Giersiepen et al, found C, α and β constants as 3.63×10^{-7}, 2.416 and 0.785 respectively [34] and these value are applied in this thesis. With these constant hemolysis is generally over predicted as shown in Figure 2.12. In this figure Hai Yu et al. have compared numerous models with experimental results for three different shear rates for 7200 s. C-GW indicates power law using Giersiepen constants. Over prediction provides to be in safe side for calculations.

$$D(\bar{\tau}, t) = \frac{\Delta H_b}{H_b} = C\bar{\tau}^{\alpha} t^{\beta} \qquad (2.4)\ [34]$$

In computational fluid dynamics power law model can be applied in two different approach; Lagrangian and Eulerien. In Eulerien model D is integrated over all flow domain while in Lagrangian model, D is integrated over a path line. Eulerian models gives relatively more accurate solution. But required computational time is higher and application is harder for Eulerian model. So, Lagrangian approach is chosen for this thesis and Eq 2.5 is used to calculate D index. In literature generally HI (Hemolysis Index) is used instead of D. HI is simply percentage format of D and given in Eq. 2.6. American Society for Clinical Pathology considers 2% is an acceptable value for HI [35].

$$D = \sum_{i=1}^{N} 3.62 * 10^{-7} * \bar{\tau}_{\mathrm{i}}^{2.416} * \Delta t_i^{0.785} \quad (2.5)\ [34]$$

$$HI(\%) = D * 100 \quad (2.6)\ [34]$$

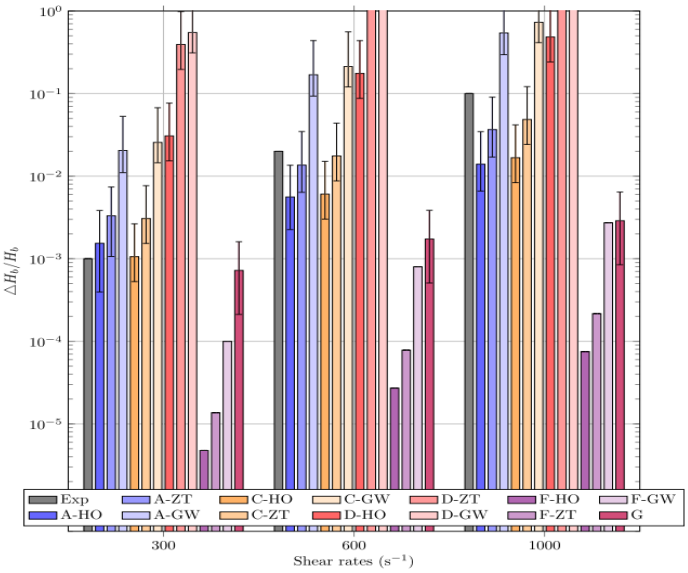

Figure 2.12. Different hemolysis model and experimental result for different shear rate for 7200s [34]

2.6. Pump Types

Pumps are classified according to working principle, flow type and flow direction as it is shown in Figure 2.13.

Positive displacement pumps create flow and this flow produces pressure. Therefore, flow rate is constant, although pressure changes [36]. Although there are many types of displacement pump, basically pump pushes fluid with a moving solid body. After pushing fluid, cavity occur in pump chamber which creates vacuum and fluid fill into chamber again. According to motion type, positive displacement pumps divided into reciprocating and rotary.

In reciprocating pumps, check valves at inlet and outlet are used. This check valves direct fluid in expanding and contacting chamber. Piston-plunger and diaphragm pumps are the most common ones, shown in Figure 2.14. When piston-plunger or diagram move to up, pressure decrease and inlet check valves open and chamber is filled with

fluid. Check valves operate for one direction, so it prevents backflow. When pressure increases, check valves at outlet open and release fluid into the system.

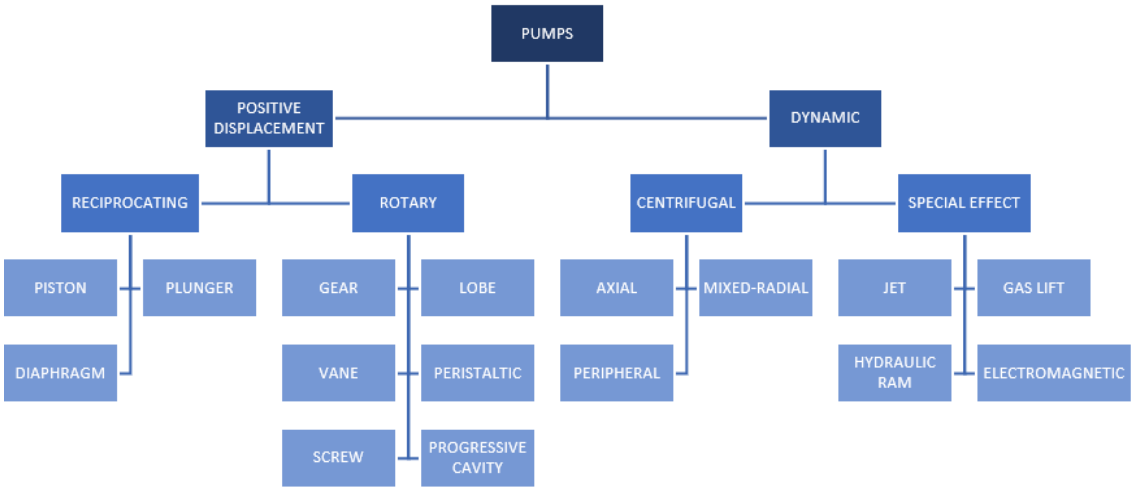

Figure 2.13. Classification of pumps [37]

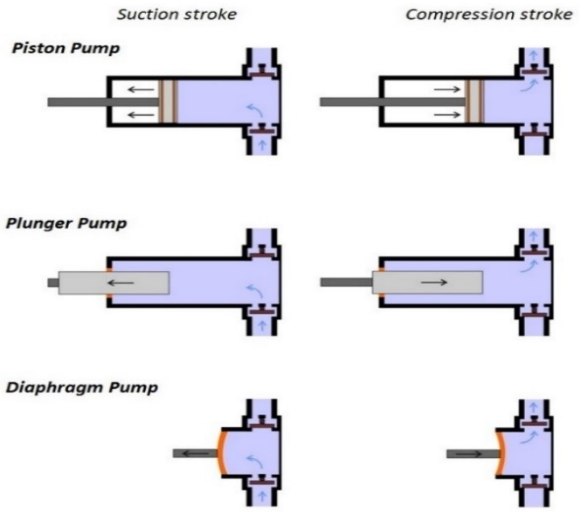

Figure 2.14. Basic reciprocating pumps design [38]

In rotary pumps, unlike reciprocating pumps, chambers are not fixed. Chambers take fluid and carry it from inlet side to outlet side. Example of rotary pumps are seen in Figure 2.15.

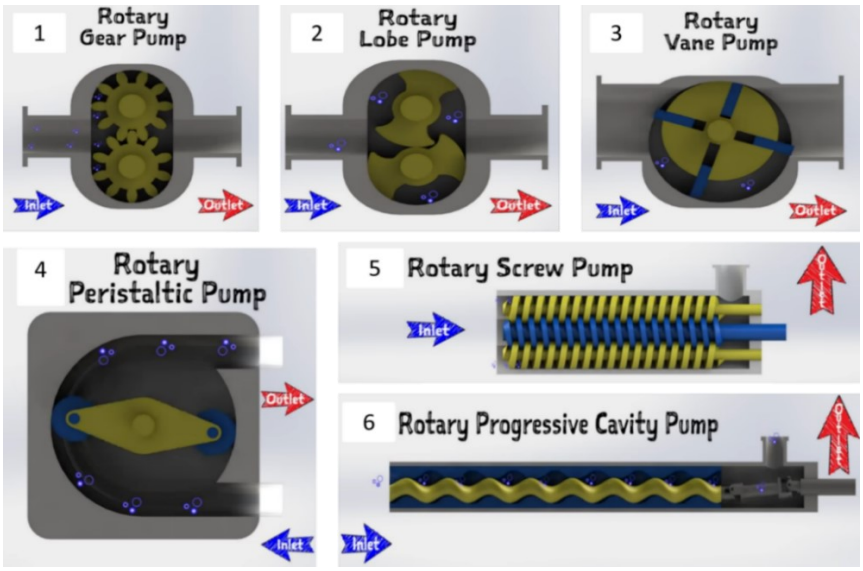

Figure 2.15. Basic rotary pumps design [39]

Unlike displacement pumps, dynamic pumps create pressure and this pressure difference produce flow. Thus, when pressure changes, flow rate also changes [36]. Centrifugal pump is popular among dynamic pumps. Centrifugal pump has two components, impeller and volute casing as it is indicated Figure 2.16. Fluid enters the center of impeller, which is called suction eye. Fluid gains kinetic energy by rotating impeller. Then, this kinetic energy is converted to potential energy when fluid leave from pump.

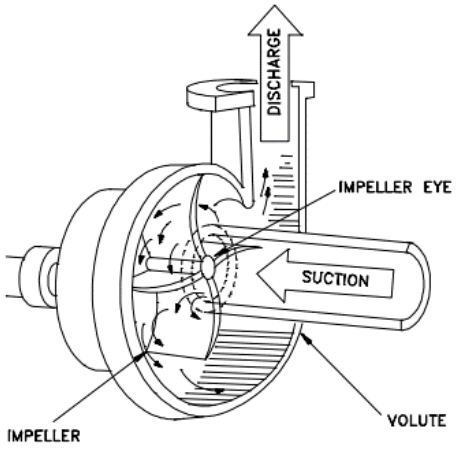

Figure 2.16. Basic centrifugal pumps design [40]

2.7. History of Blood Pumps

2.7.1. Early Pumping Devices for Blood

In the middle of the 19th century, perfusion, which means blood or any solution is injected and pumped via vessels to organs or tissues, was achieved by gravity assisting devices. Simply, it was an open circuit system where continuous circulation did not occur. Blood flowed out and then oxygenated blood transferred into the arterial reservoir. However, process was interrupted due to lack of a pump. The first closed perfusion circuit was designed by Max von Frey and Max Gruber in 1885 [41] which can be seen Figure 2.17. Circulation was accomplished by engine-power syringe pump. A film type oxygenator, valves, pressure measuring device and 10 mL motor-driven syringe were included in this closed circuit.

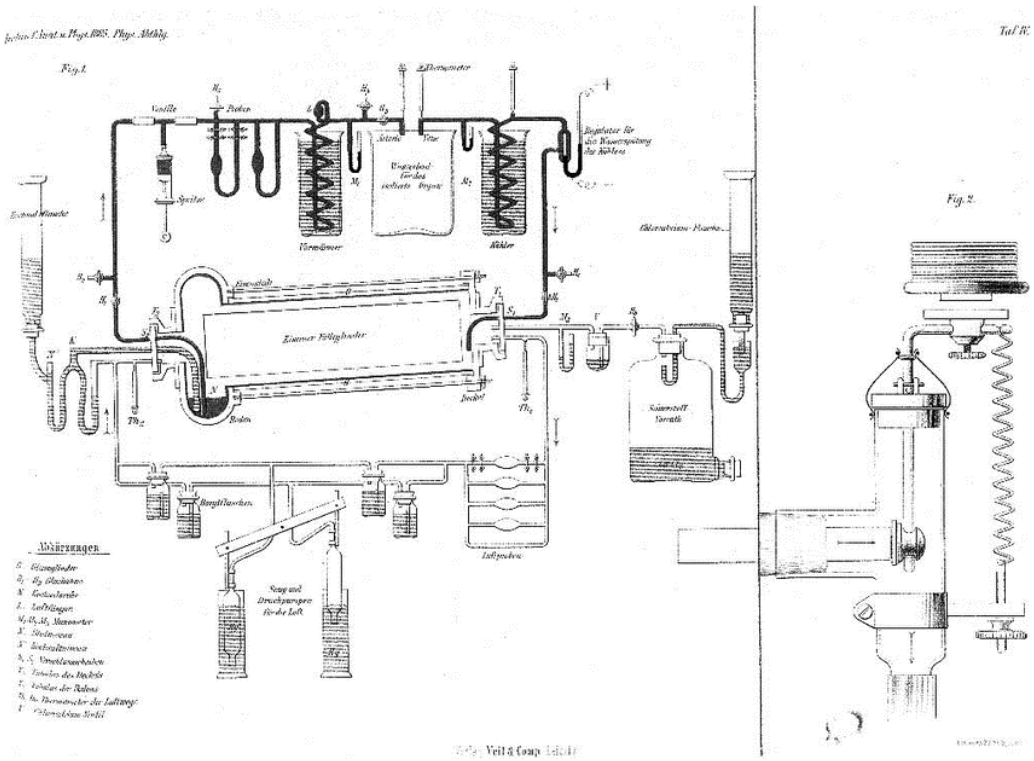

Figure 2.17. Pioneer of today's heart-lung machine [42]

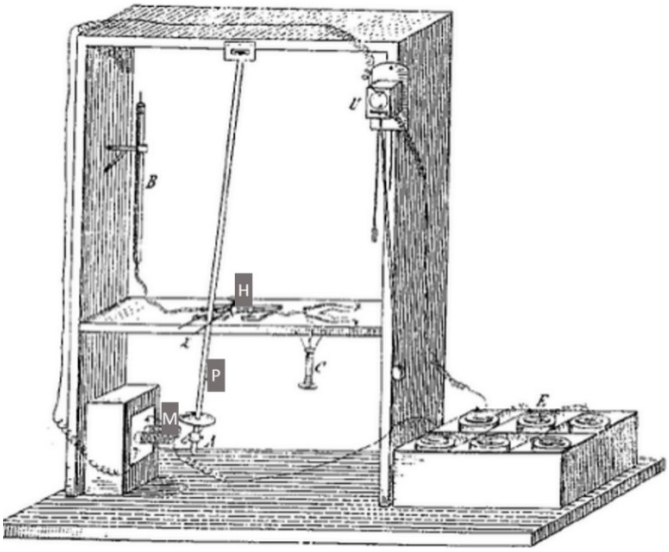

Figure 2.18. Electrical pendular cock developed by Hammel (1889) [43]

In 1887, manually operated roller pump was investigated by Allen. In 1889, Hamel was designed electrical pendular cock to provide pulsatile perfusion [41]. As it is indicated in Figure 2.18, magnet (M) activated pendulum (P) and it opened and closed a stop-cock (H).Because of the pulsatile flow in Hammel's design, tissue edema which is swelling caused by fluid, decreased when compared to continuous flow. Following years, pulsatile pumping devices were studied even further by other researchers due to this advantageous pulsatile flow characterization. In 1890, Jacobj invited rhythmically compressed rubber balloon for pulsatile flow. Pulsatile membrane pump was popular during 1950s [41]. However, because of noisy, vibrate and large size, it has been lose popularity in time. In 1960s, VADs begun to replace cardiopulmonary bypass circuits and researchers interested more with study about VADs [43].

2.7.2. First Generation VADs (1965-1990)

These VADs were displacement pumps, which generates pulsative flow. It had pneumatically or electrically driven models [44]. Direction of blood flow was controlled by inlet and outlet valves. These pumps split by three groups according to connection

parts; left, right- or biventricular assist devices as it can be demonstrated in Figure 2.19. For example, left VADs are connected to LV.

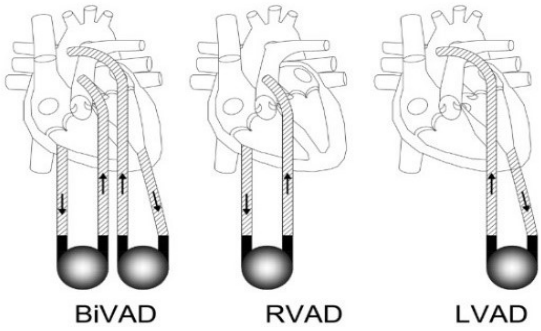

Figure 2.19. Left-, right- and biventricular assist devices [45]

In 1966, DeBakey and Dr. Lioatta used first LVAD during a surgery [44]. Heartmate XVE LVAS, centrimag RVAD and Berlin Heart EXCOR are examples of first generation VADs. Heartmate XVE LVAS is shown in Figure 2.20. However, first generation VADs have some disadvantage. First, these pumps were not small so it created portability problem. Second, they involved many moving parts and that created mechanical problems. Third, there was high possibility of blood damage because of moving parts. Fourth, these pumps had to be changed after two weeks which is very a short time for a patient waiting for heart transplant. Because of these reasons these type of pumps can only be used in a hospital or in a controlled environment [46].

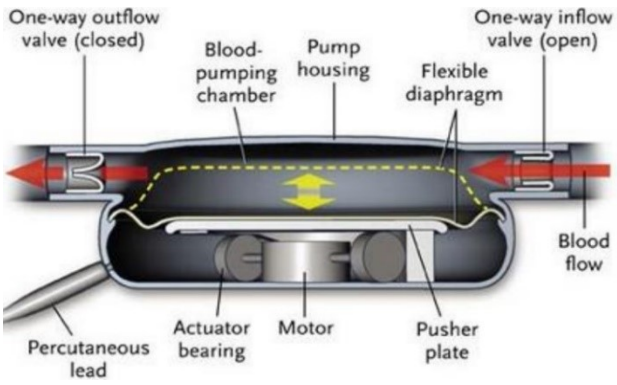

Figure 2.20. Heartmate XVE LVAS - example of first generation LVADs [46]

2.7.3. Second Generation VADs (1990-2000)

In 1990s, second generation VADS were developed for more durability and smaller sizes [47]. These pumps provide continuous flow. Both centrifugal types and axial types were used. High rotational speeds were employed to reached required pressure head. They had mechanical bearings which was the main disadvantage of these types pumps. Because these mechanical bearings and seals cause extensive hemolysis (a.k.a. blood damage). Eveheart and Jarvik 2000 are two examples for centrifugal and axial second generation VADs, respectively as they were shown in Figure 2.21.

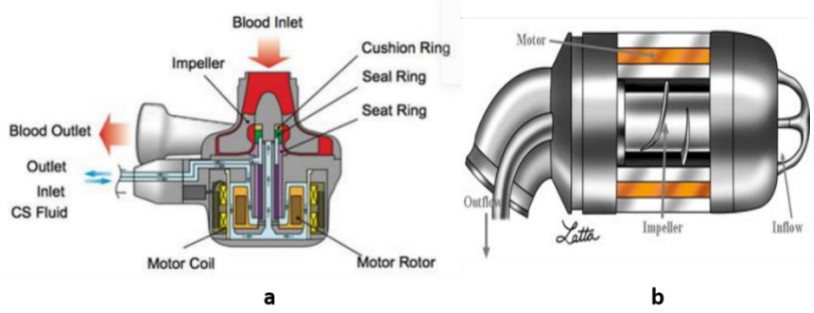

Figure 2.21. Second Generation VADS (a)Eveheart [47] (b)Jarvik 2000 [48]

2.7.1. Third Generation VADs (2000-present)

Generally, blood damage occurs in vicinity of seals and mechanical bearings because of high local shear stress. In this third generation pump type, magnetic bearings, couplings are used, where local shear is eliminated, instead of mechanical ones [49]. Therefore, blood damage decreases considerably. Levitronix CentriMag, MedTech Heart and Berlin Heart INCOR are commercial examples of this pump type [47]. In this generation to lift rotor first hydrodynamic levitation is used. Later magnetic levitation pumps are developed for reasons stated below.

In hydrodynamic levitation, two types of bearings are used; spiral groove and passive magnetic bearing. Spiral groove bearing employed in hydrodynamic bearings without lubricant, is shown in Figure 2.22. These groves create a pressure difference to levitate rotor. However, it cannot provide stability in radial direction. To prevent

imbalance, passive magnetic or permanent magnet bearings, shown in Figure 2.23, are used. These two are used together to provide more stable balance for rotor movement. In Figure 2.24, a simple schematic is given.

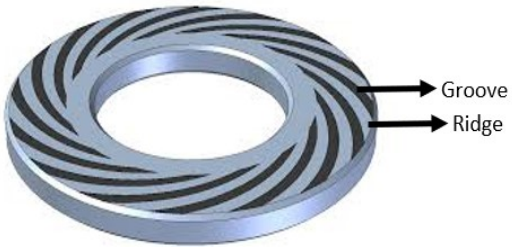

Figure 2.22. Spiral groove bearing profile [50]

In next technology, named maglev, active magnetic bearings are applied in rotor and stator (pump housing) as shown in Figure 2.25. Several positions sensors are placed around rotor to detect rotor positions precisely. This position information is interpreted by a microprocessor and according to rotor position, coils magnetic force is adjusted to conserve equal clearance at all circumference [51]. This gives rotor more stable positions compared to hydraulic levitation method. Control principle of the system is roughly illustrated in Figure 2.26.

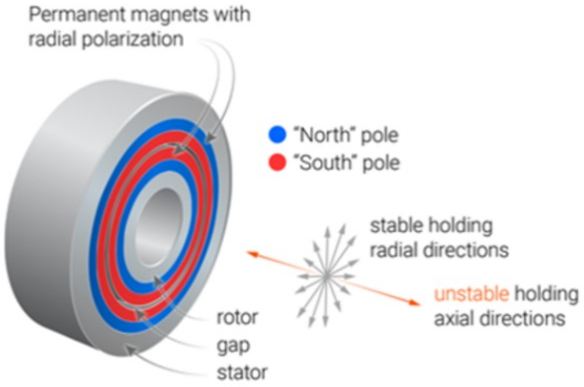

Figure 2.23. Passive magnetic bearing with permanent magnets [51]

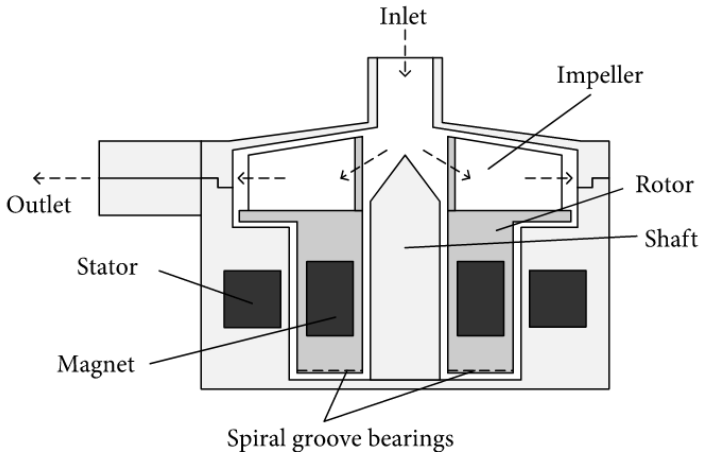

Figure 2.24. Blood pump with hydrodynamic levitation [52]

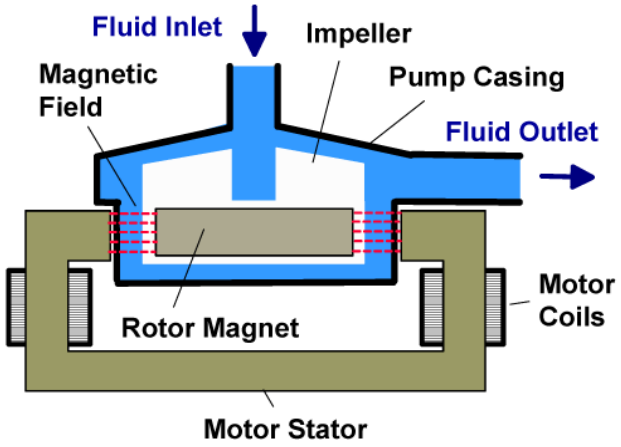

Figure 2.25. Maglev centrifugal pump [53]

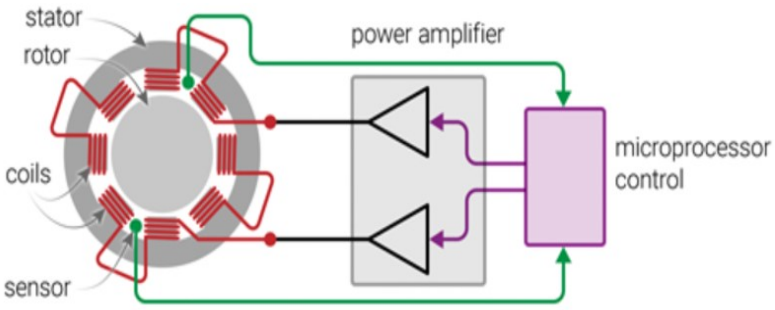

Figure 2.26. Active magnetic bearings [51]

2.8. Blood Pump Types

Pumps has very wide usage nearly in every sector with vital functions. In health care sector, blood pumps are used very commonly, especially for cardiovascular diseases. Blood pumps are divided into two categories according to usage area. If blood pump is placed inside of the body, it is called intracorporeal VAD. This VAD should not be confused with total artificial heart (TAH). When intracorporeal VAD is placed in the body, heart stays at same place and VAD is located just below of heart [54]. However, in TAH surgery, heart is completely removed and replaced with TAH [55]. It functions for both LV, RV and also four cardiac check valves are used. It is demonstrated in Figure 2.27.

Some pumps are designed to placed outside of body. These pump types are extracorporeal VADs. Example of extracorporeal and intracorporeal VADs are shown in Figure 2.28. VADs consists three parts; pump, that is placed inside or outside, console and battery, that placed outside for both pump types [54]. Console is used to change settings and battery provides required power for adequate time.

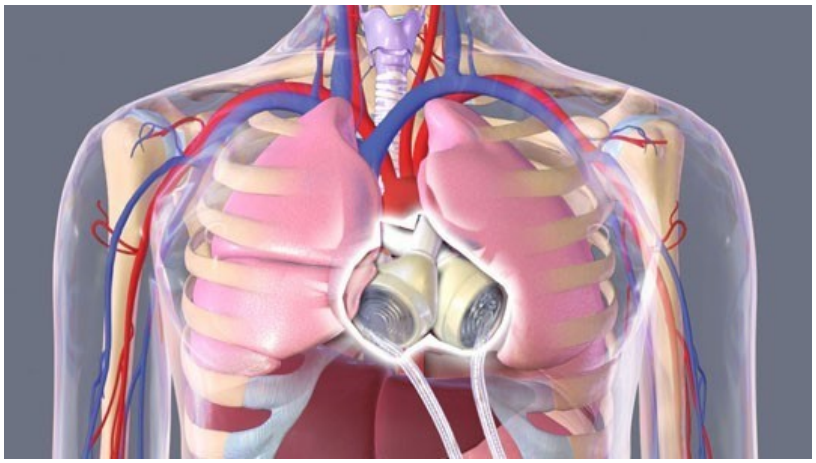

Figure 2.27. Simple sketch of TAH [55]

Intracorporeal pumps are placed inside of the body only by surgically. However, extracorporeal pumps are placed by surgically or percutaneously, which means through the skin [56]. When pump is placed by surgically, one side is connected to chamber and other side connect to vessels. In percutaneous method, both sides are connected to vessels.

Tie-in points for percutaneous is determined according to patient needs. Two different examples of percutaneously extracorporeal connections are indicated in Figure 2.29.

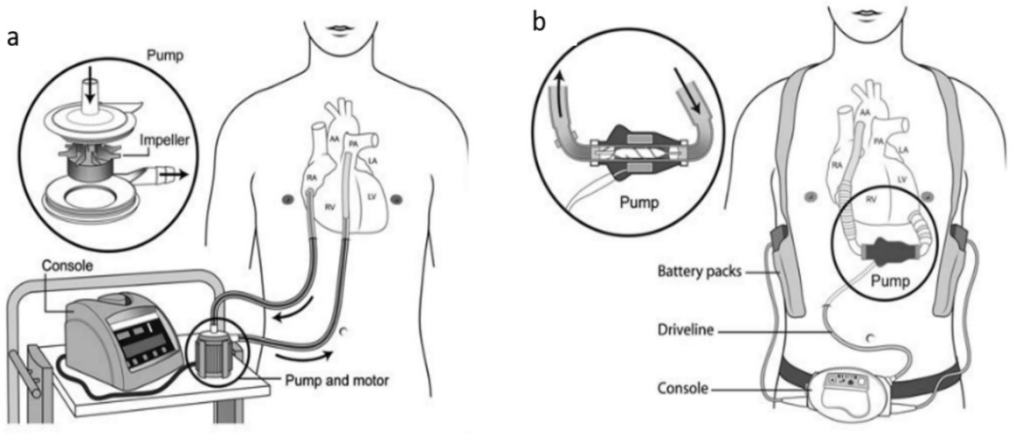

Figure 2.28. Simple sketch of VADs (a) Extracorporeal VADs (b)Intracorporeal VADs [57]

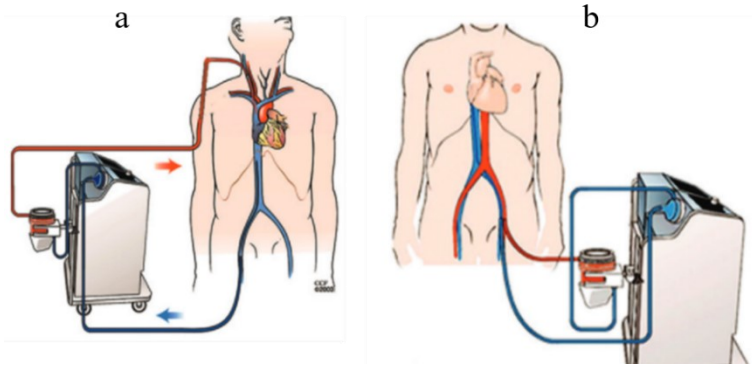

Figure 2.29. Simple sketch of two different percutaneous methods for VADs treatment (a)Venovenous type (b)Venoarterial type[56]

VADs are classified in terms of time period as short-term and long-term. Generally, short-term VADs are used for approximately 7 days. If treatment is over 7 days, it is defined as “prolonged short-term VADs” [58]. Long-term VADs have been developed and nowadays, they can be used up to about 10 years [59]. In long-term treatment, LVAD is more preferred. BIVAD and RVAD are less than 15% of VADs usage for long-term [60].

Generally, intracorporeal VADs are applied for long-term. Long-term extracorporeal VAD trials show 53 out of 69 patients have systematic inflation (SI). SI is observed in blood streams and has effect on whole body. 17% of these patients who have SI have died sooner [61].

Short-term VADs are used in cases like, cardiogenic shock, acute decompensated heart failure and cardiac arrest. Generally, cardiogenic shock result from heart attack. Because heart cannot pump with enough head, blood is not able to reach organs [62]. In acute decompensated heart failure, heart is also insufficient. However, reasons of decompensated heart failure are viruses attacking cardiac muscles, severe infection, allergic reactions, etc. [63]. Hearth attack does not cause acute decompensated heart failure. The other disfunction is cardiac arrest which often confused with heart attack. In heart attack, veins are blocked in hearth and blood flow decreases dramatically even hearth is still beating, on the contrary, in cardiac arrest, heart stop beating although all veins are fine. In other words, heart attack is about circulation problem and cardiac arrest is associated with electrical pulses hearth receives, that creates irregular rhythm [64].

VADs are also separate each other in terms of flow types, that are continuous flow (CF) and pulsatile flow (PF). Heart creates pulsatile flow, which means flow with periodic change, when beating. CF-VADs cause more vascular and aortic valve disease and gastrointestinal bleeding [65]. Vascular and aortic means related with vessels and aorta, respectively. Gastrointestinal concerned about digestion system. In addition, von Willebrand disease appears more frequent with CF-VADs [56]. Von Willebrand is bleeding disorder which effects clotting. Despite of these disadvantages, CF-VADs are smaller, more reliable and more durable [66]. Also, possibility of blood clot formation [67] and infection risk decreases [56]. Therefore, CF-VADs are preferred as it is seen in Figure 2.30.

According to usage purpose, VADs are divided three categories, bridge to transplant (BTT), bridge to recovery (BTR) and destination therapy (DT).

VADs, which is used to survive patient until find suitable donor, are called as BTT-VADs Usually, BTT-VADs are applied more than 6 months and intracorporeal types are preferred for this application [57]. But this treatment is risky for patients over 50 years old. Approximately, donor can be found for 50% of patients in 1 year. However 40% of these patients die when using BTT-VADs. However, patients younger than 30 years old are more enduring for this treatment. 70% of them reach suitable donor and only

13% of them die when supporting with BTT-VADs [68]. In 2008, first CF-BTT-LVAD HeartMate II (Thoratec, Pleasanton, CA) is approved. Before 2008, 70% of patients, who use LVAD, confront serious problems or even die in 1 year. However, after CF-BTT-LVAD application, their life spans prolong up to about 4 years [69].

Rarely, VADs can be used for treatment and they are defined as BTR-VADs. The number of patients, recovering by this method, consists only 5% of all patients, who used VADs. BTR-VADs are applied mostly less than 3 months. In addition, BIVADs are preferred for these patients [70].

Some patients are not suitable candidates for a heart transplant. For these patients DT-VADS are used. These are applied to prolong their life and improve their life quality [71]. Generally, pulsatile flow is preferred for DT-VADs [70].

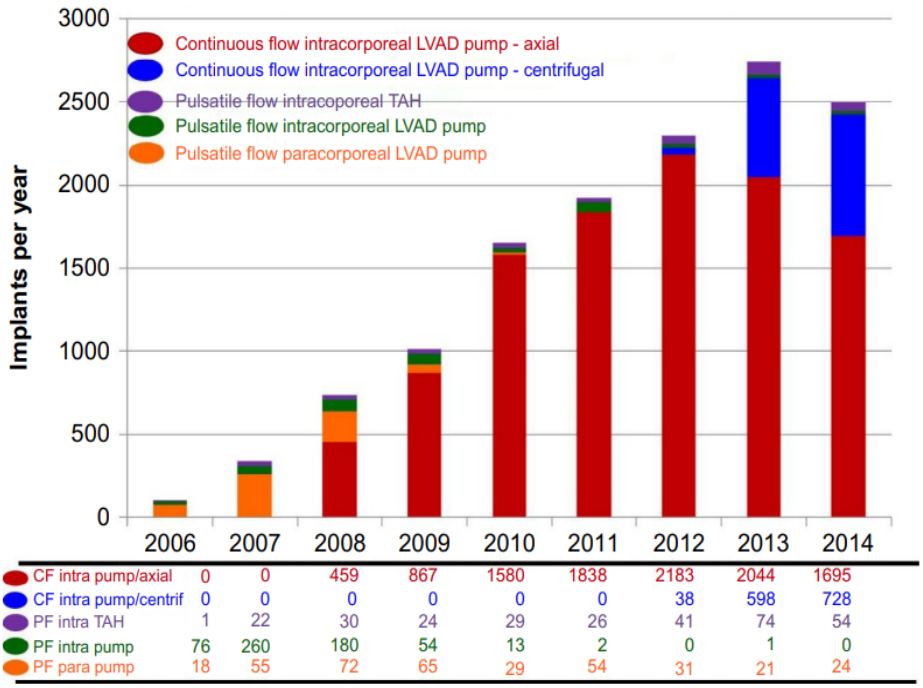

Figure 2.30. Number of implant VADs between 2006 and 2014, reported in INTERMACS database [68]

CHAPTER 3

CENTRIFUGAL PUMP DESIGN

3.1. Pump Sizing

Pump operating point is given as 3.3 L/min, 200 mmHg and 5000 rpm. In this project, design method and all equations are taken from "Pump Handbook" by Igor J. Karassik [37]. This method is mainly employed for common commercial pumps. These pumps have much larger flow rate and considerably lower rpm. To accommodate that difference, pump head is taken as 300 mmHg for calculations. While designing pump, two main parts are considered; impeller and volute. An example calculation for procedure given below is made in Appendix A.

Firstly, specific speed of the pump is calculated to determine the general shape of the impeller. In literature many different specific speed equations could be found. In this project pump specific speed is calculated with Eq. 3.1 given below.

$$N_{sm} = \frac{N\sqrt{Q}}{H^{0.75}} \tag{3.1}$$

where; N is rpm, Q is m^3/s and H is m-blood. According to specific speed value, impeller orientation is decided as shown in Figure 3.1. For designed blood pump specific value is about 14. Accordingly, high head radial impeller type is chosen.

After impeller shape is determined, slip factor should be calculated. Slip factor shows ratio between, absolute peripheral component velocity of impeller discharge to theoretical peripheral component velocity of impeller discharge as given in Eq. 3.2. This difference arises from three main reasons; non uniform velocity distribution on impeller, flow separation and accumulation on boundary layer. Since the velocities in Eq. 3.2 are all unknowns, this can be estimated by many different empirical correlations such as the one given by Stodola [37] in Eq. 3.3.

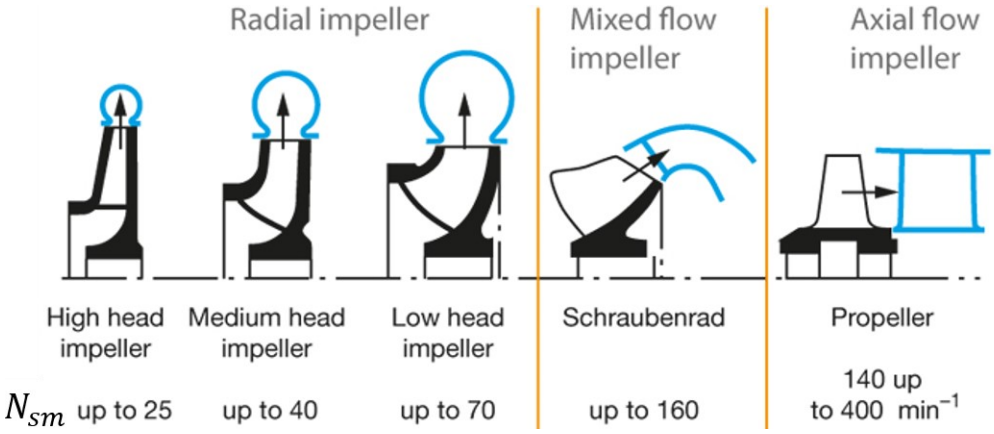

Figure 3.1. Impeller design for different specific speed [72]

$$\mu = \frac{c'_{u3}}{c_{u3}} \tag{3.2}$$

$$\mu = 1 - \frac{\pi sin\beta_2}{z} \tag{3.3}$$

where; z is blade number and β_2 is blade discharge angle. β_2 can be taken from Figure 3.2. According to calculated specific speed, β_2 can be chosen from an interval. For designed pump β_2 range from 20^0 to 90^0. This is a base parameter that have the highest uncertainty. Because of that, many different β_2 values have been investigated in this thesis, results are given in CFD results part. For blade numbers, six is chosen according to literature research and commercial pump investigations. Basically, blade number should be kept at minimum, to prevent flow blockage which increases shear rate for a great amount. According to Qein at al. (2002), blade number should be kept between 5-7 to minimize hemolysis for β_2 values between 20^0 and 40^0. Their test results indicate that for 30^0 minimum hemolysis is achieved with 6 blades [73]. Also Peng Fang et. Al. (2020) achieved similar results with Qein at al. They tested 5-8 blades with β_2 ranging from 0^0-40^0. According to results scalar shear stress is found minimum at 6 blades [75].

In next step, hydraulic efficiency of pump, η is assumed. Actually, it is possible to calculate this parameter but, designed pump is small and has higher rpm accordingly commonly applied pumps in industry. Because of that reasons using these equations does not give accurate results. So, instead of calculation, hydraulic efficiency is assumed by

using ref [73] and Figure 3.3 as 30%. This value will be checked later with CFD calculation.

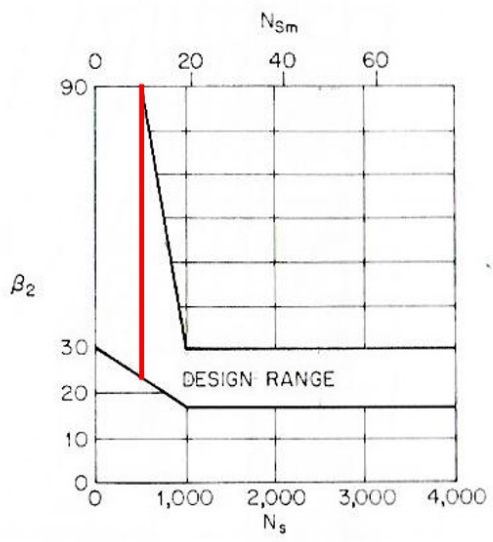

Figure 3.2. Impeller discharge angle vs specific speed [37]

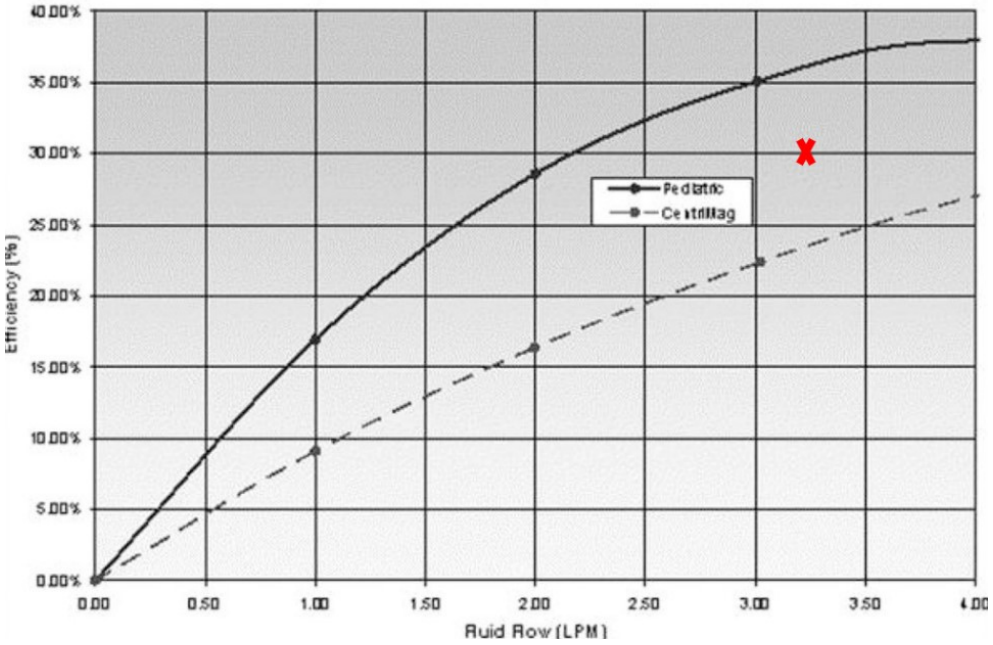

Figure 3.3. Hydraulic efficiency vs volumetric flow rate of PediVAS compared with CentriMag pump systems [75]

Peripheral speed of impeller discharge, u_2, is calculated according to Eq. 3.4 given below, where ψ is head coefficient and H is total head. Head coefficient is defined for characterizing pump head for specific operating conditions. Note that total head (300 mmHg) should be taken as meter of blood column. Head coefficient is taken as 1 from 'pump types table' in ref [76] regard to specific speed.

$$u_2 = \sqrt{\frac{2gH}{\psi}} \tag{3.4}$$

Based on peripheral speed of impeller discharge and specific speed, theoretical meridional velocity of impeller discharge calculated by using Eq. 3.5 and Figure 3.4. Then meridional absolute speed; c_{m3} is used to calculate the theoretical peripheral component velocity of impeller discharge, c_{u3} with Eq. 3.6.

$$c_{m3} = \left(\frac{c_{m3}}{u_2}\right)_{graph} u_2 \tag{3.5}$$

$$c_{u3} = u_2 - c_{m3} cot\beta_2 \tag{3.6}$$

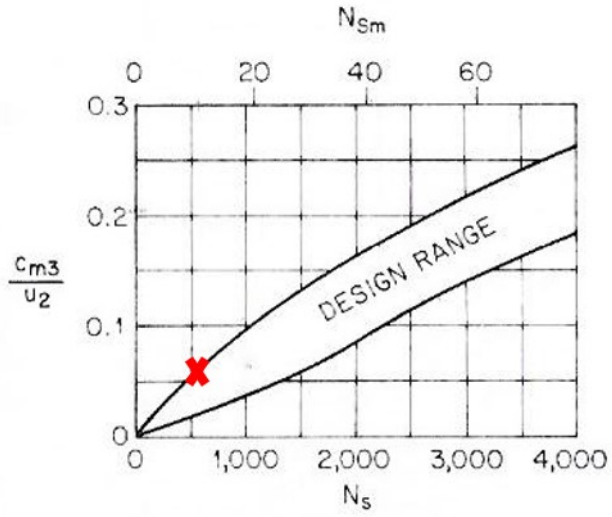

Figure 3.4. c_{m3}/u_2 vs N_{sm} [37]

In next step absolute peripheral component velocity of impeller discharge is calculated by using slip factor with Eq. 3.2. Velocities calculated up to here is given schematically in Figure 3.5. Then impeller discharge diameter can be calculated with Eq. 3.7. At this point a base size for pump can be predicted. This calculations lead to another important step, calculating discharge impeller width b_2 with Eq. 3.8. b_2 is also shown schematically in Figure 3.6.

$$D_2 = \frac{60*u_2*1000}{\pi N} \tag{3.7}$$

$$b_2 = \frac{Q*10^6}{2\pi r_2 c_{m3}} \tag{3.8}$$

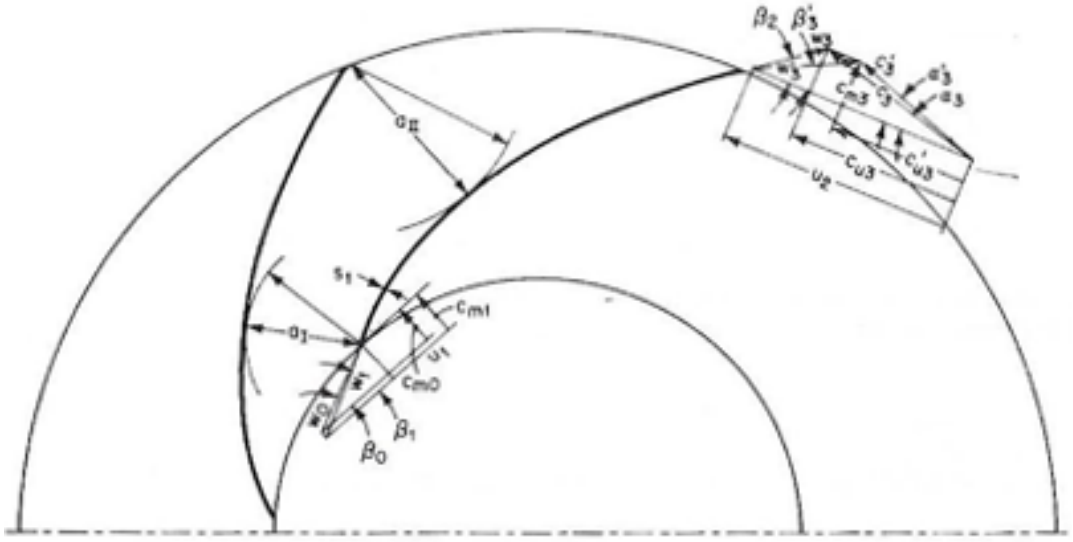

Figure 3.5. Velocity triangles [37]

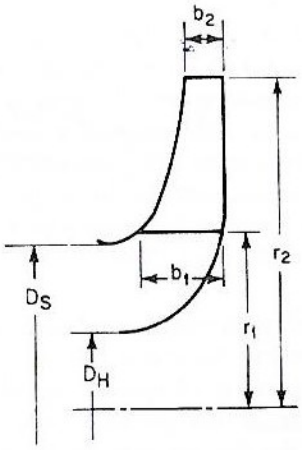

Figure 3.6. Impeller cross-section [37]

Q is volumetric flow rate, β_0 is flow angle and k is the hub ratio defined in Eq. 3.10 where D_h is hub diameter , D_s is suction diameter. For designed pump D_s is taken as 8 mm for compatibility with medical devices. Also designed pump does not have hub on

impeller. For this case or when Eq. 3.10 result is close to zero, in other words hub ratio can be taken as 1.

β_0 is an important value when calculating $NPSH_R$. This pump will operate about normal body temperature which could be assumed as 37 C^0. At these temperatures water vapor pressure is very low and because of dissolved substances blood vapor pressure is lower than water vapor pressure. For this reasons cavitation is not expected and $NPSH_R$ value is not critical. In cases like this it is acceptable to take β_0 as 17^0.

$$r_1 = \frac{1}{2} * 2897 * (\frac{Q}{kNtan\beta_0}) \tag{3.9}$$

$$k = 1 - (\frac{D_H}{D_S})^2 \tag{3.10}$$

Assumptions made up to this point is justified by checking r_{1m} ratio to r_2. This ratio should be smaller than 0.5 to ensure assumptions made are acceptable [37]. r_{1m} is called as mean inlet radius and calculated by Eq. 3.11 given below, where r_H is hub radius and r_1 is inlet radius.

$$r_{1m} = \sqrt{\frac{r_1^2 + r_H^2}{2}} \tag{3.11}$$

After finding r_1 with Eq 3.9 and checking assumptions, c_{m0}, theoretical meridional velocity of impeller eye and u_1, peripheral speed of impeller eye is calculated with Eq. 3.12 and 3.13 respectively.

$$c_{m0} = \frac{Q*10^6}{\pi r_1^2} \tag{3.12}$$

$$u_1 = \frac{\pi r_1 N}{30*1000} \tag{3.13}$$

Based on assumed value of β_0, blade inlet angle, β_1, is calculated with Eq. 3.14. Where z is blade number, s_1 is inlet blade thickness, r_1 is impeller eye radius as shown in Figure 3.7. For designed pump inlet blade thickness s_1 is taken as 1 mm. Also to simplify impeller production whole blade thickness is assumed as 1mm and CFD calculations are made accordingly.

$$tan\beta_1 = \frac{tan\beta_0}{1 - \frac{zs_1}{2\pi r_1 sin\beta_1}} \tag{3.14}$$

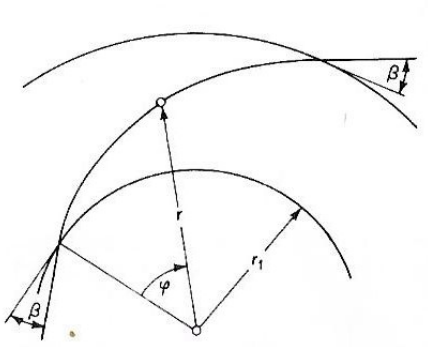

Figure 3.7. Schematic illustrating r_1 measurement [37]

After calculating all these parameters summarized in Table 3.1, all required information is found and now it is possible to design the blade shape.

For impeller design two different methods are commonly employed; circular arc and point by point method. In point by point method blade is divided into smaller pieces and more precises calculation could be done. This method is generally used for bigger impellers. But in smaller ones, circular arc method is adequate. There are two different ways to implement circular arc method; single arc and double arc method. As can be interpreted in single arc method only one curve is used for to determine vane shape. Considering designed pump diameter and for practical reasons, single arc method is applied for this pump. Drawing of single blade by single arc method is demonstrated in Figure 3.8.

To apply single arc method firstly two circles is drawn with D_2 and D_1 diameters which found by eq. 3.8 and 3.10 respectively. After an arbitrary point B is chosen on circle with D_2 diameter and this point is connected with center of circles. This creates [OB] line. After this [BN] line is created having β_2 angle respect to [OB] line. Then a [OK] line is created from circle center having $\beta_1 + \beta_2$ angle respect to [OB] line. After, a line is drawn through point B on outer circle passing from point K on inner circle. This line intersects again with inner circle on point A. From middle point of [BA] line a perpendicular line is drawn which intersects with [BN] line on point G. Point G is the center of arc drawn from point A to point B. This arc gives blade shape.

Table 3.1. Parameters to design blade shape

Description	Symbol	Value	Unit
specific speed	N_{sm}	14	-
impeller discharge angle*	B_2	25	degree
slip factor*	μ*	0.78	-
hydraulic efficiency**	η	30	%
head coefficient**	ψ	1	-
peripheral speed of impeller discharge	u_2	8.7	m/s
theoretical meridional velocity of impeller discharge	c_{m3}	0.5	m/s
theoretical peripheral component velocity of impeller discharge*	c_{u3}*	7.6	m/s
absolute peripheral component velocity of impeller discharge*	c_{u3}'*	5.9	m/s
impeller discharge diameter	D_2	35	mm
impeller radius	r_2	17.5	mm
impeller discharge width	b_2	0.9	mm
impeller eye diameter	D_1	10	mm
impeller eye radius	r_1	5	mm
mean inlet radius	r_{1m}	3.5	mm
blade inlet angle	$\beta 1$	28	degree
theoretical meridional velocity of impeller eye	c_{m0}	0.7	m/s
peripheral speed of impeller eye	u_1	2.6	m/s

* These parameters change accordinly with $\beta 2$

** These parameters taken from references (Not calculated).

After completing impeller design, volute shape is designed by following calculations. Firstly inlet area between blades; A_1 and discharge area between blades; A_2 are calculated by following Eq. 3.16 and 3.17 respectively where s_2 is discharge blade thickness. As mentioned above outlet blade thickness and inlet blade thickness are taken as 1 mm in this project.

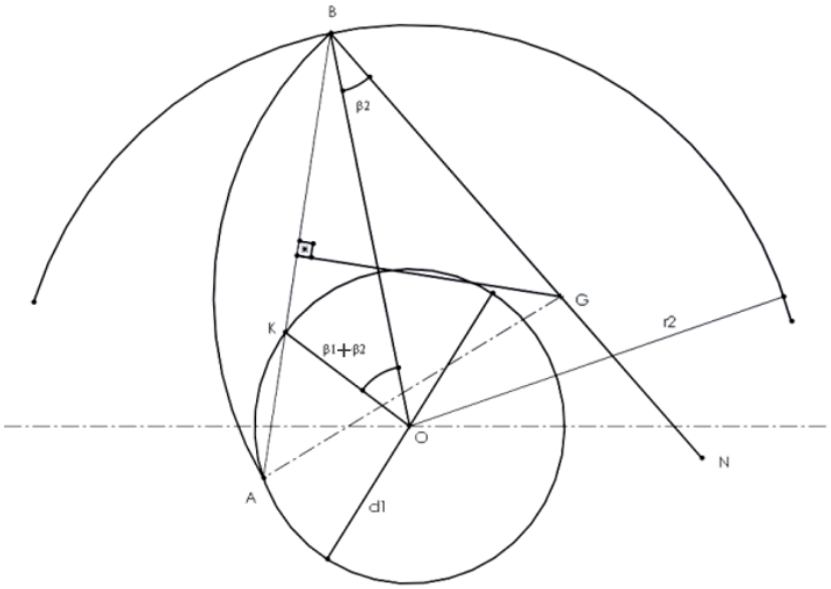

Figure 3.8. Drawing of single blade by using single arc method [77]

$$A_1 = \pi r_1^2 sin\beta_1 \tag{3.16}$$

$$A_2 = b_2(2\pi r_2 sin\beta_2 - zs_2) \tag{3.17}$$

Then a quick check for ratio between A_2 to A_1 is made. If ratio is less than 1.3, values are acceptable.

For next step throat velocity c_{thr} is calculated by using Figure 3.9 and Eq. 3.18 where u_2 is peripheral speed of impeller discharge. This figure is generated for common usage pumps having much larger diameter and lower rpm than designed pump. So, it is not logical to use graph directly. When values are taken directly from graph, c_{thr} is about 5 m/s which is a very high velocity for blood flow. To ensure more reasonable speed, c_{thr} is taken as 1.4 m/s which similar to outlet flow velocity.

$$c_{thr} = \left(\frac{c_{thr}}{u_2}\right)_{graph} u_2 \tag{3.18}$$

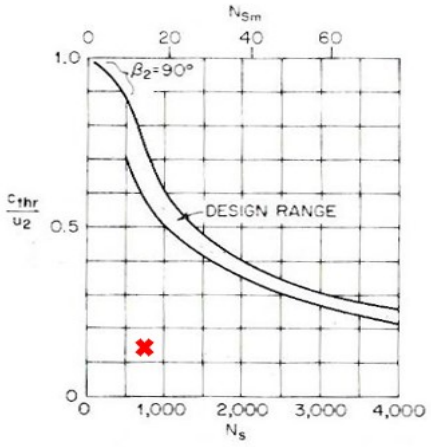

Figure 3.9. C_{thr}/u_2 vs N_{sm} [37]

After that, according to throat velocity, required throat area and throat radius is calculated by Eq. 3.19 and 3.20 respectively.

$$A_{thr} = \frac{Q*10^6}{c_{thr}} \tag{3.19}$$

$$r_{thr} = \sqrt{\frac{A_{thr}}{\pi}} \tag{3.20}$$

Tongue clearance, which is an important parameter indicating minimum distance of blade tips to volute is calculated by Eq. 3.21. This distance generally taken as 7% of impeller diameter because of mechanical reasons.

$$t = 0.07 * r_2 \tag{3.21}$$

With calculated values it now possible to find r_4 by Eq. 3.22 which gives distance of the throat center from the impeller center indicated in Figure 3.11.

$$r_4 \cong r_2 + t + r_{thr} \tag{3.22}$$

Volute area, shown in Figure 3.10, is calculated by Eq. 3.23. A_{thr} is illustrated in Figure 3.11. φ_v is called as central angle and takes multiples of 45^0 starting form 0^0 up to 360^0.

$$A_v = A_{thr} * \frac{\varphi_v}{360} \tag{3.23}$$

When calculating r_{short}, illustrated in Figure 3.10, volute height should also be considered. In this design, volute height is taken as 8mm. r_{long} is 4 mm, found by dividing volute height by two. Then r_{short} is calculated by using Eq. 3.24.

$$r_{short} = \frac{A_v}{\pi r_{long}} \tag{3.24}$$

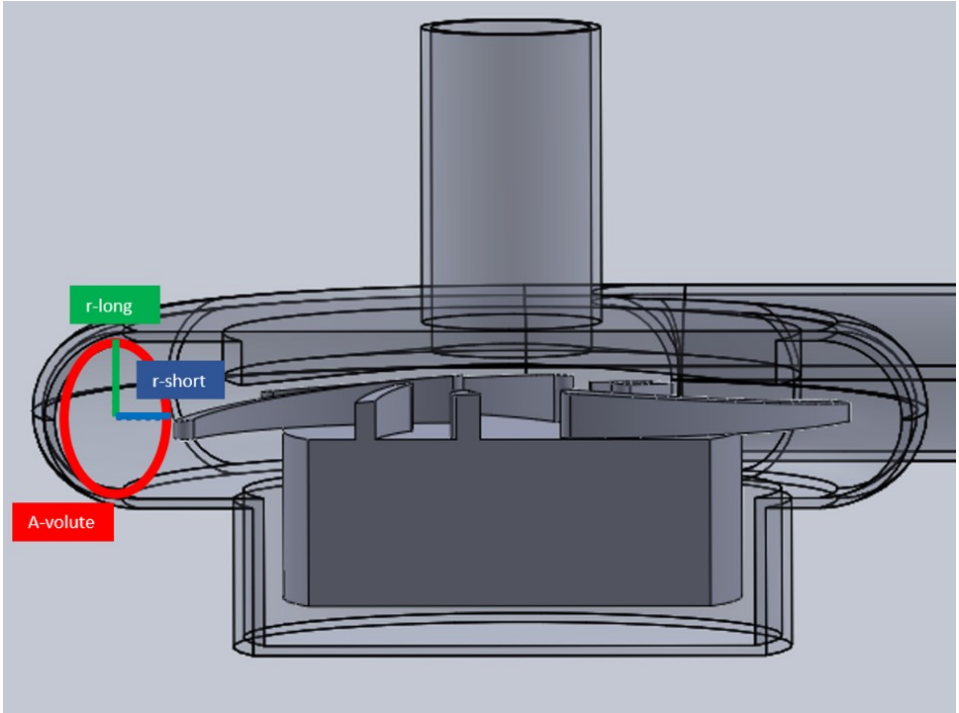

Figure 3.10. Cross-sectional area of 3D centrifugal pump from SolidWorks

Volute area varies with respect to central angle. While r_{long} stays same, r_{short} changes with central angle. r_{short} values directly used for drawing volute and give volute, its helix shape, which characterizes shape of centrifugal pump, as demonstrated in Figure 3.12. Small circles placed around impeller circumference are called spiral area, total 8 of them are drawn for each φ_v value. r_{short} values are defined as radius of A_{sp} circles and these values are used to find r_v, shown in Figure 3.11, by using Eq. 3.25. Also, volute area should be checked according to fluid velocity by using Eq. 3.26. Results should be nearly same with throat velocity. Because theoretically, as central angles increases, mass flow rate should also increase proportionally at volute area. To accommodate velocity increase, volute area should also increase at least same proportion.

$$r_v = r_2 + t + r_{short} \tag{3.25}$$

$$v = \frac{Q * \frac{\varphi_v}{360}}{A_v * 10^{-6}} \tag{3.26}$$

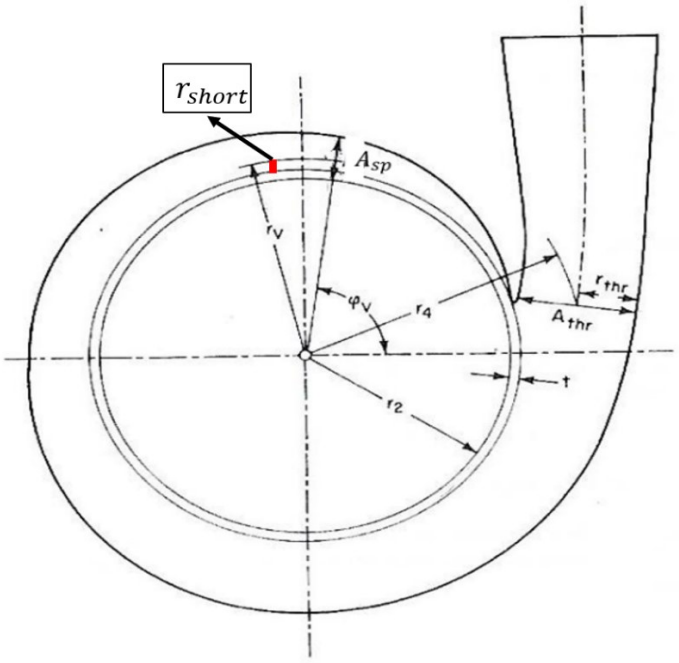

Figure 3.11. Volute casing [37]

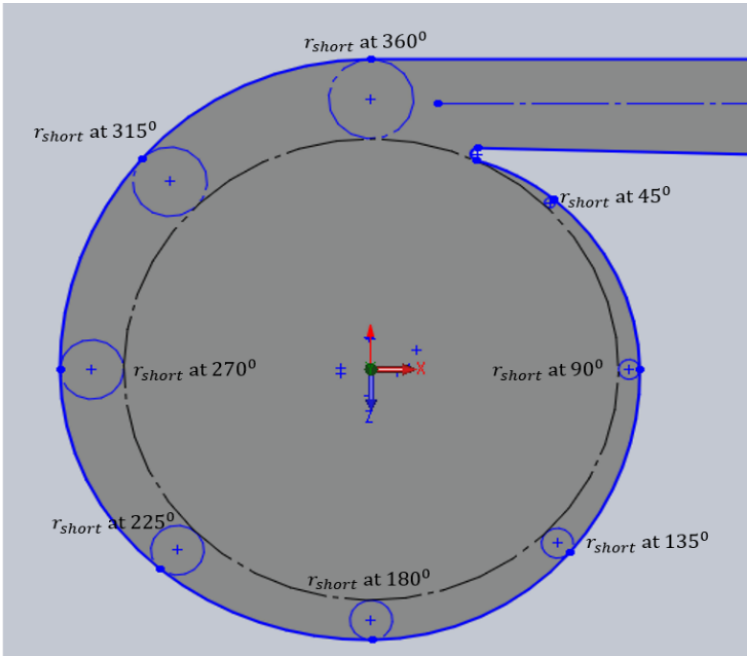

Figure 3.12. Volute casing from SolidWorks

3.2. Designed Pump Shape Considerations

Designed blood pump production method aims to be compatible with 3D printer technology. This feature makes it easier to produce different sized pumps for experiments less time consuming and cost efficient. To achieve this volute is designed in two separate pieces shown in Figure 3.13. After production these pieces can easily combined together.

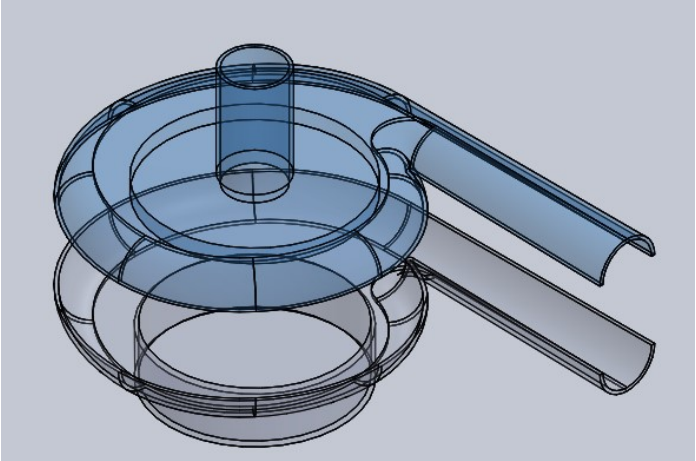

Figure 3.13. Upper and lower volutes

Mentioned above pump will be using magnetic levitation for rotor movement. For this application passive magnets should be embedded inside rotor. Because of that a part under impeller is left for magnet placement with 8.5 mm height and 11.5 mm radius as shown in Figure 3.14. Accordingly lower part of volute should have the same shape with rotor as demonstrated in Figure 3.15. Clearance between rotor and volute in lower part is taken as 2 mm both from circumference and bottom, shown in Figure 3.16. Also lower volute part should be compatible with active magnet system. When in operation pump will be placed on active magnet drive system. Up clearance value firstly assumed as 2 mm, illustrated in Figure 3.16, but different values are also tried in CFD. Suction and discharge diameters is taken as 8 mm as shown in Figure 3.16. Other parts dimensions are directly used from values found in section 3.1 and pump modelled as 3D in SolidWorks.

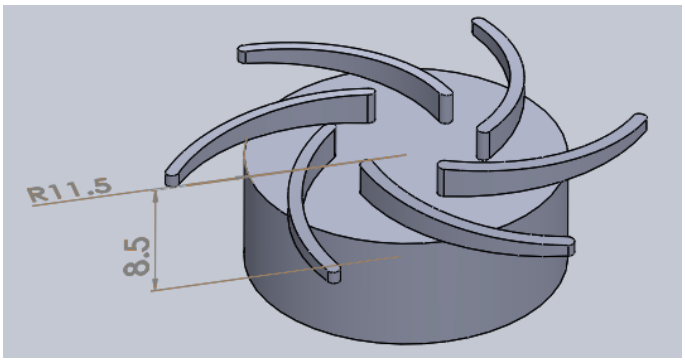

Figure 3.14. Rotor height and radius

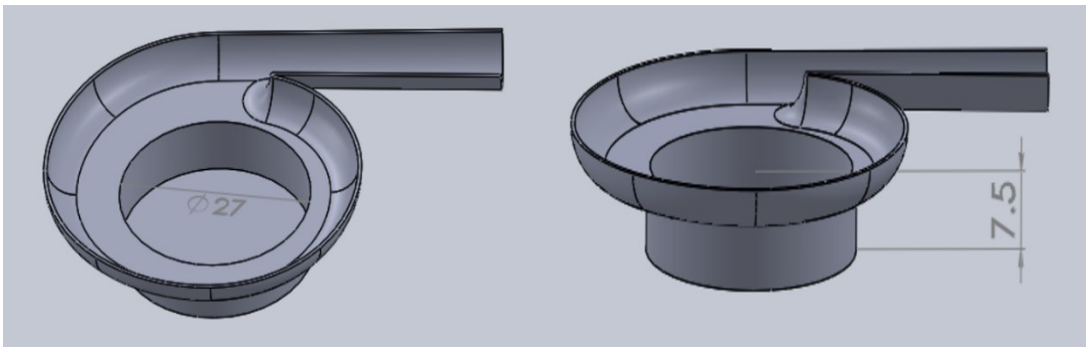

Figure 3.15. Lower volute height and diameter

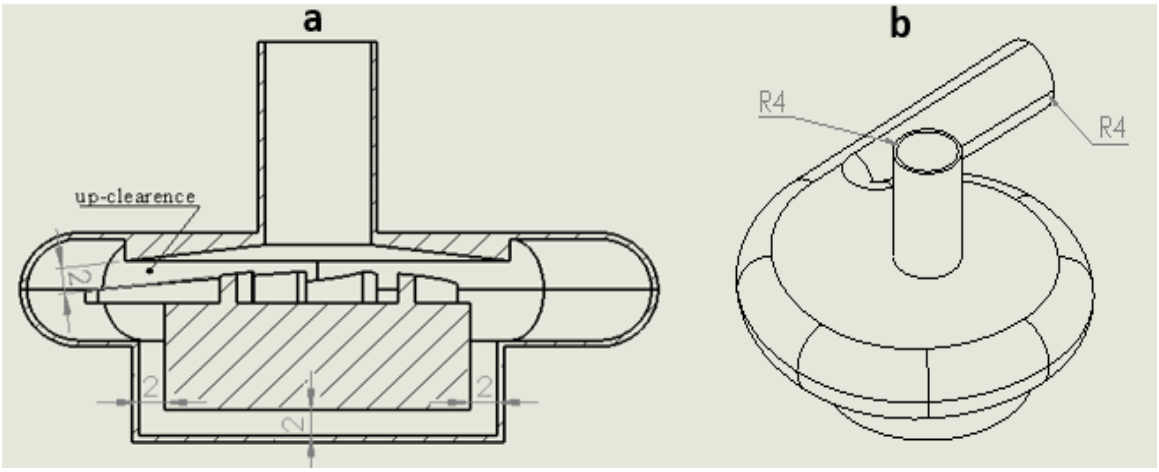

Figure 3.16. (a) Pump section view (b) Suction and discharge radius

CHAPTER 4

CFD MODELLING

Firstly, pump modeled 3D in SolidWorks according to details given in Chapter 3. Pump is drawn in three different parts; upper volute, lower volute and rotor. Then these parts are assembled and exported to Ansys SpaceClaim. In SpaceClaim a 2D interface is drawn between rotor and volute parts as shown in Figure 4.1. Interface is drawn along middle points between rotor and volutes. This interface will be useful for defining rotating parts and stationary parts of pump. Then model is opened in Ansys DesignModeler and 2D interface is rotated around rotor axis and a 3D thin surface is created between rotor and volute as illustrated in Figure 4.2. After that, in the same software fluid parts of pump is defined and model is exported to meshing.

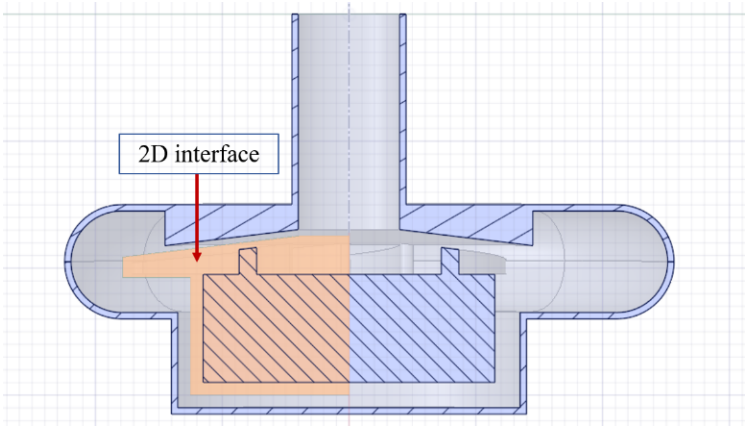

Figure 4.1. 2D interface drawing in Ansys SpaceClaim

In meshing, software divides fluid space in smaller pieces according to given parameters. A well-structured mesh is very important for an accurate CFD solution. The most important parameter is skewness which is an indication of mesh quality and defined as difference between the shape of the cell and shape of an equilateral cell of equivalent volume, illustrated in Figure 4.3. Generally, values under 0.95 is acceptable.

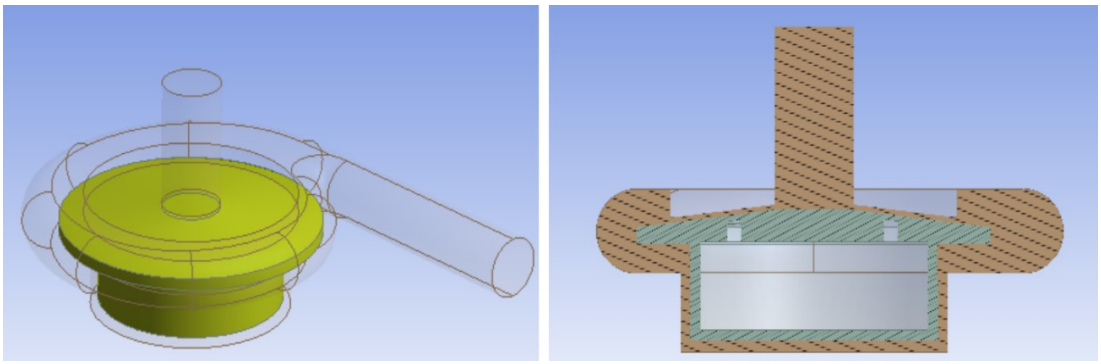

Figure 4.2. 3D isometric and cross-sectional view of interface in Ansys DesignModeler

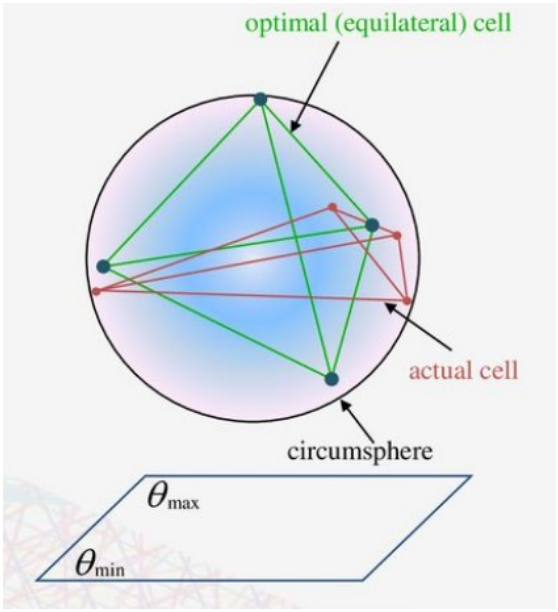

Figure 4.3. Schematically equilateral cell [78]

Also, for more accurate results, special consideration is taken for boundary layers at solid surfaces where velocity gradients are expected to be large. In Ansys Fluent, inflation meshing can be used at boundary to cover boundary layers with several layers mesh. Inflation type meshing is applied at these locations to improve boundary layer results quality which in turn improves overall results accuracy. For inflation first layer thickness type is selected. For this type user should define first layer thickness of boundary layer, mesh size growth rate, and number of maximum boundary layers. First layer thickness is actually thickness of the first mesh elements near walls. Mesh grow rate

defines, increase in element edge length for each upper layers of mesh. Mesh structure which is used in this study shown particularly in Appendix B. Number of maximum boundary layer indicate, number of mesh layers that should be in inflation zone. To decide these values, one should consider y^+ value. y^+ is a non-dimensional wall distance of which non-dimensional turbulence velocity is defined, this is also known as wall function. For clear understanding, an illustration is given in Figure 4.4.

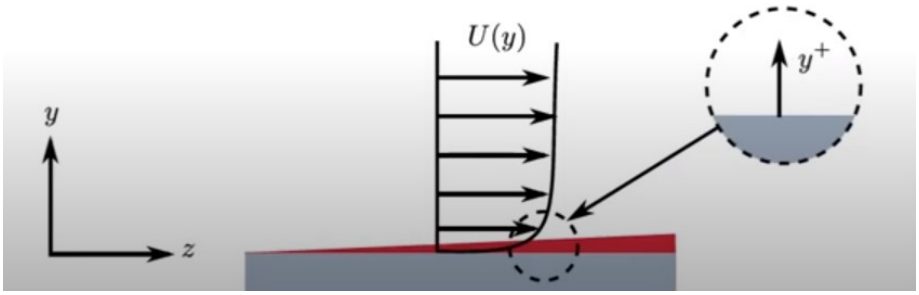

Figure 4.4. Representation of y^+ in 2D [79]

Theoretically dimensionless y^+ can be calculated with Eq. 4.1 given below. But for complex systems calculating y^+ with this equation is not possible, generally numerical solutions or empirical equations are used. Another likewise dimensionless wall function is U+ which is calculated by Eq. 4.2 given below.

$$y^+ = \frac{\rho y \sqrt{\tau_w/\rho}}{\mu} \quad (4.1)\ [79]$$

$$U^+ = \frac{U}{\sqrt{\tau_w/\rho}} \quad (4.2)\ [79]$$

Based on these two walls function a numerical experiment is conducted and results are summarized in Figure 4.4. U+ and y+ are corelated with each other for different boundary layer sections with Eq 4.3 and 4.4 for viscous sub-layer and log-law region respectively. In Figure 4.5, green line represents Eq. 4.3, blue line represents Eq. 4.4 and black line represent experimental and directly numerical solution results. But this graph is built for a zero pressure gradient flow and no flow separations. According to y+ value, CFD software uses Eq. 4.3 or 4.4, based on y+ range. Generally, recommendation is to

have y+ value around one so that it occurs in the viscous sub-layer section. Because, in this, region Reynolds number does not have big impact on velocity profile. So, for models where high pressure gradients and flow separation occur, more accurate results are obtained in this region with these empirical equations. So, to begin CFD calculations logical guessed first layer thickness value "y" is given to software. Then in post processing part y+ results are checked. If results are not in intended range, meshing is repeated with different first layer thickness values. In this project this procedure is repeated until y+ results are around one.

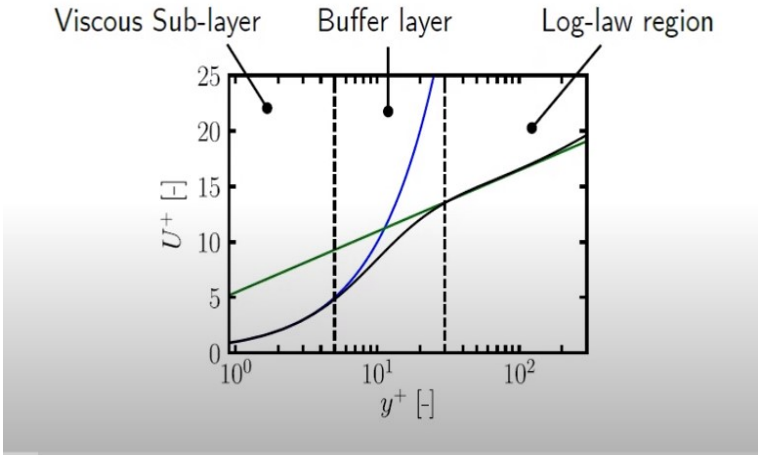

Figure 4.5. U^+ vs y^+ [79]

$$U^+ = y^+ \qquad y^+<5 \quad (4.3)\ [79]$$

$$U^+ = \frac{1}{\kappa}\log(Ey^+) \qquad 30<y^+<200 \quad (4.4)\ [79]$$

So, with all of these preprocessing part of CFD is completed and it is now possible to move CFD solver part. Boundary conditions are created, like inlet, outlet, rotating walls, stationary walls. Inlet and outlet boundary conditions are demonstrated in Figure 4.6. At walls no slip boundary condition is assumed. Two zones are defined in Fluent for rotating and stationary volumes. To define rotor rotation rpm is stated 5000 as absolute to frame at rotating zone and 0 rpm is stated for stationary zone relative to absolute frame. Rotating walls are defined as 0 rpm for relative to adjacent cell zone which is rotating at

5000 rpm relative to absolute frame. Stationary walls are defined as 0 rpm relative to absolute frame to make sure walls are stationary.

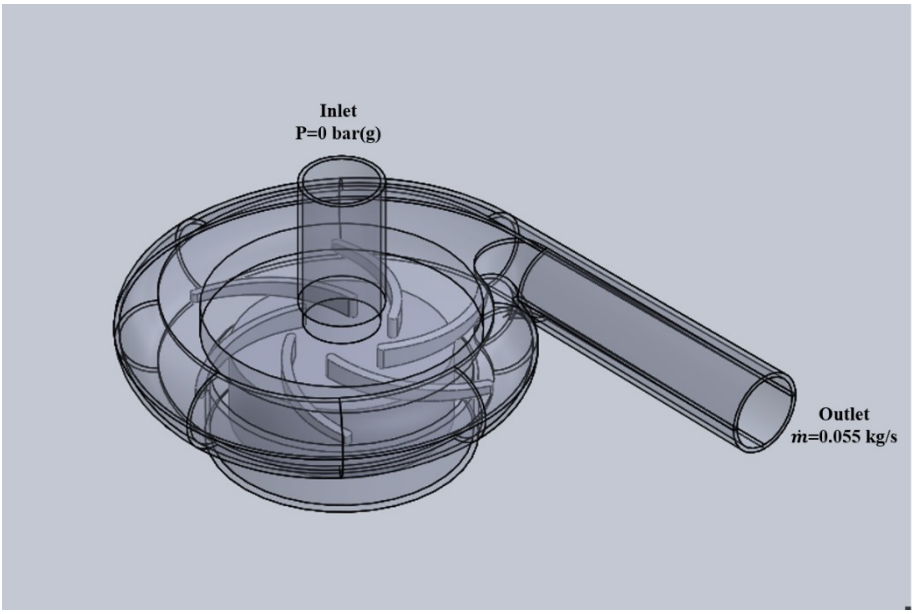

Figure 4.6. Inlet and outlet boundary conditions

Then appropriate solving model should be selected according to problem's nature. There are eleven different main viscous models available in the Fluent software. These models can be divided into three main categories; scale resolving simulation (SRS), Reynolds Averaged Navier Stokes (RANS), unsteady RANS (URANS) where their sub-models are shown in Figure 4.7. In SRS, large eddies are calculated by using Navier Stokes and little eddies are modeled. Therefore, this model is chosen for large separated flows like strongly swirling flows and acoustics where unsteady events and large turbulent scales becomes important sources of noise generation. In RANS and URANS simulations, average flow equations are solved but all eddies are modeled, so their computational requirements are much less than SRS's. However, URANS is used in special cases like periodic or quasi-periodic flows. If flow is steady or unsteady and aperiodic, RANS is usually preferred and used for almost all industrial applications.

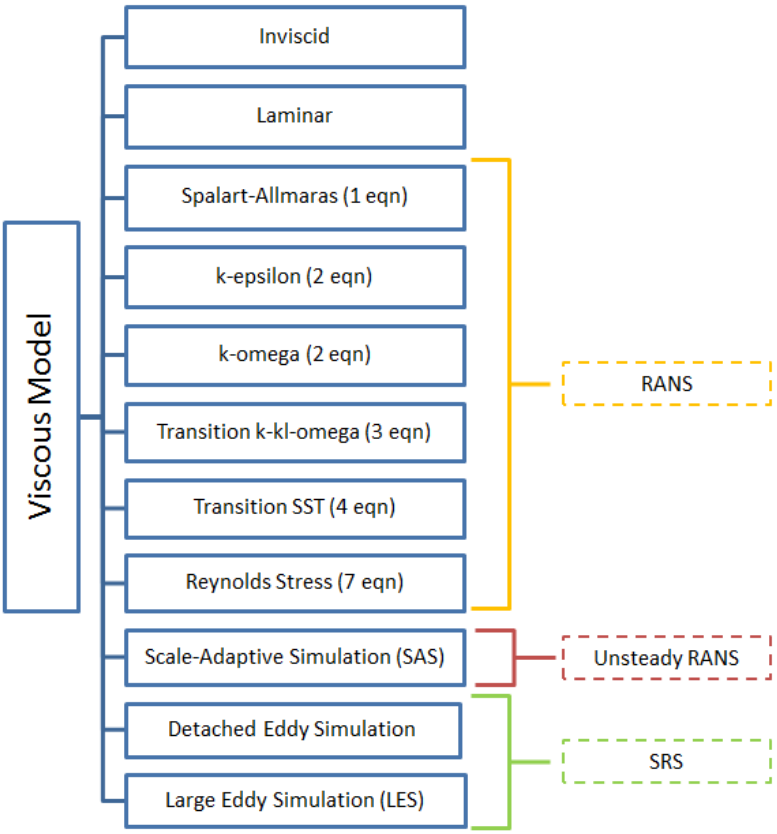

Figure 4.7. Models in ANSYS fluent

RANS equation is given Eq. 4.5 where the last term is Reynolds Stress. This term should be modelled for CFD solving. Generally, Boussinesq hypothesis is used to calculate Reynolds Stress. However, in this hypothesis μt is assumed as isotropic scalar quantity. In Fluent, Spalart-Allmaras, k-epsilon and k-omega models utilize Boussinesq hypothesis. Boussinesq hypothesis approach has low computational cost and calculated with Eq. 4.6 given below.

$$\frac{\partial(\rho u_i)}{\partial t} + \frac{\partial}{\partial x_j}\left(\rho u_i u_j\right) = -\frac{\partial p}{\partial x_i} + \frac{\partial}{\partial x_j}\left[\mu\left(\frac{\partial u_i}{\partial x_j} + \frac{\partial u_j}{\partial x_i} - \frac{2}{3}\delta_{ij}\frac{\partial u_l}{\partial x_l}\right)\right] + \frac{\partial}{\partial x_j}\left(-\overline{\rho u_i' u_j'}\right) \quad (4.5)\ [80]$$

$$-\overline{\rho u_i' u_j'} = \mu_t\left(\frac{\partial u_i}{\partial x_j} + \frac{\partial u_j}{\partial x_i}\right) - \frac{2}{3}\left(\rho k + \mu_t\frac{\partial u_i}{\partial x_i}\right)\delta_{ij} \quad (4.6)\ [80]$$

Difference between k-epsilon and k-omega models arises from calculation of μ_t called as "Eddy Viscosity". In k-epsilon model μt is calculated by Eq. 4.7 and in k-omega it is calculated by Eq. 4.8. Epsilon is defined as turbulence dissipation rate whereas omega is defined as the specific turbulence dissipation rate both of which are a measure of viscous forces converting kinetic energy to heat.

$$\mu_t = \frac{\rho C_\mu k^2}{\epsilon} \quad (4.7) [79]$$

$$\mu_t = \frac{\rho k}{\omega} \quad (4.8) [79]$$

Generally for centrifugal pump simulation, k-omega model is employed. In Fluent, there are three different options for k-omega model; standard, baseline (BSL) and shear stress transport (SST). BSL model was proposed by Menter in 1992 [81]. BSL model uses combination of k-epsilon and k-omega models where k-epsilon is used far away from wall flows and k-omega is used for the near wall locations of the boundary layers. So, ω isn't extremely sensitive in freestream [82]. In 1994, Menter developed SST k-omega model to accurately estimate adverse pressure gradient cases. Also it includes viscosity limiter which gives better results at mildly separated flows compared to other models [83].

SST k-omega was used in previous studies and verified with experimental results [85]. One very similar project where SST k-omega model has been used is by Yue Wu (2017) et al. They investigated blood flow through a centrifugal pump and compare experimental and model results. Comparison of the experimental data and SST k-omega model is presented in Figure 4.8. As can be seen head vs. volumetric flowrate results are well matched between experimental and model. Except for the higher flow rates at a lower rotational speeds where separated regions are expected to be large, agreement is very good. Since this design will be operating between 2000-5000 rpms, even better agreement should be expected.

In another project, flow and hemolytic performance of UltraMag blood pump is investigated by Ertan Taskin et al.(2010) [85] by SST k-omega turbulence model. Head-volume flow rate curves are indicated at different rotational speeds; 5000, 7000 and 9000 rpm in Figure 4.9. It is seen that the experimental results are slightly under predicted but trend is matched very closely.

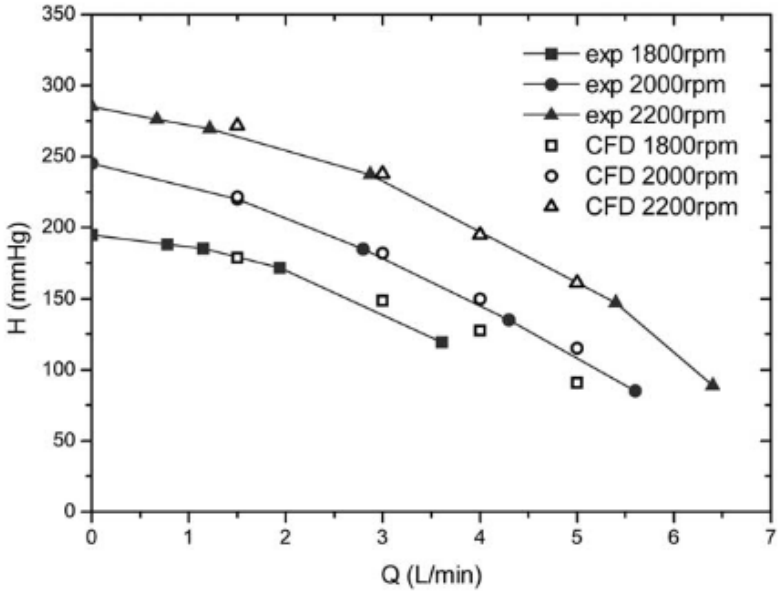

Figure 4.8. Comparison of experimental and SST k-omega numerical pressure head of the pump [84]

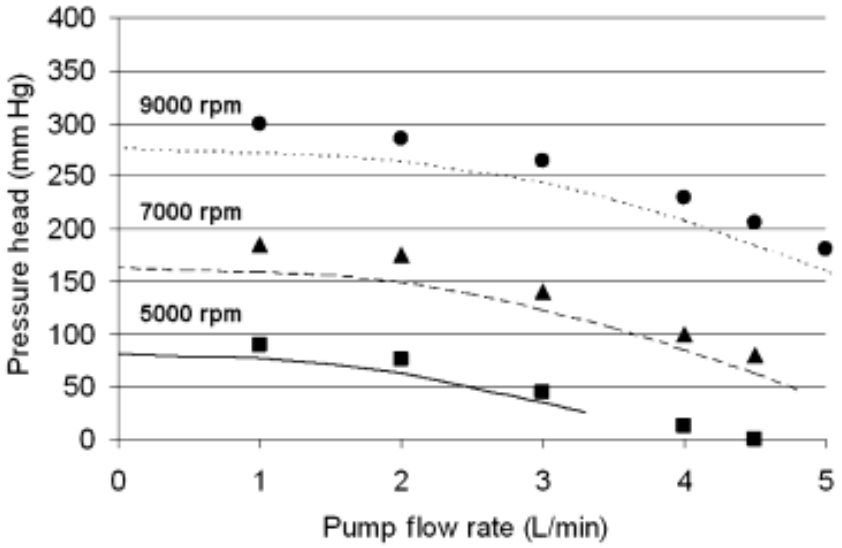

Figure 4.9. Comparison of experimental and SST k-omega numerical pressure head of the pump [83]

Although SST k-omega model is commonly used for centrifugal blood pump CFD simulations, there are also many studies which employs realizable k-epsilon model. A well-established study is made by Jeffrey Kennington et al, in which experimental results are compared with CFD results [87]. They have investigated a pump with 0.5 – 4.4 l/min flow rate at 1000-5000 rpm interval which is similar to one that is studied in this thesis. In Figure 4.10, experimental results and CFD results are given in head vs volume flow rate graph. At high rpm's, experimental data closely matched with CFD results.

This thesis can be interpreted as preliminary work to determine base parameters. So, trying many different combinations was first priority which is time consuming. When solving times are compared, k-omega model took almost three times longer than k-epsilon model to converge for designed pump case. So, to reduce calculation time, realizable k-epsilon enhanced wall model is employed in this thesis.

Fluid is chosen as water as to simulate an incompressible liquid flow, but density and viscosity of blood is used instead as of default values. Because of incompressible flow, pressure based solver is chosen. In solution method part, coupled algorithm is employed. In discretization part, pressure is 2nd order, momentum is 2nd order upwind, turbulent kinetic energy and turbulent dissipation rate are 1st order upwind.

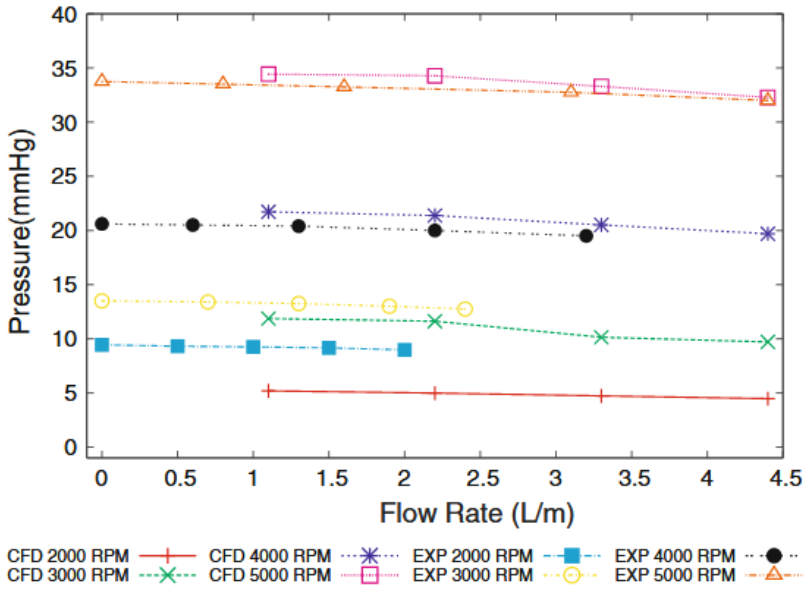

Figure 4.10. Comparison of experimental and enhanced k-epsilon numerical pressure head of the pump [86]

Stated in Chapter 2 blood damage calculation is made by power law model with Giersiepen constants in Lagrangian form. For this Discrete Phase Model(DPM) particle injection is used in Fluent. Massless particle type is used. Total 100 particle is injected from inlet. Then results are exported to Post CFD software. In this software Eq. 2.4 is entered. For t, particle time step is used and $\bar{\tau}$ is calculated by Eq. 4.9 for every time step of particle. Then according to Eq 2.5, D is summed for every time step to find total D on the particle path line.

$$\bar{\tau} = \left[\begin{array}{c} \frac{1}{3}\left(\tau_{ii}^2 + \tau_{jj}^2 + \tau_{kk}^2\right) - \frac{1}{3}\left(\tau_{ii}\tau_{jj} + \tau_{jj}\tau_{kk} + \tau_{kk}\tau_{ii}\right) \\ +\left(\tau_{ij}^2 + \tau_{jk}^2 + \tau_{ki}^2\right) \end{array} \right]^{1/2} \quad (4.9)\ [87]$$

CHAPTER 5

CFD RESULTS & DISCUSSION

In this thesis, important parameters that has direct impact on pump performance are studied primarily. Firstly impeller discharge angle impact on pump head is investigated. β_2 values ranging from 20^0 to 40^0 with 5^0 intervals for 2.00 mm up-clearance are studied and results are given in Figure 5.1. As can be seen from figure higher β_2 values leads to higher pump head specially for lower flow rates. But after 4.0 L/min pump with β_2 40^0, pump head decreases more rapidly than other discharge angles. Considering pump BEP capacity is 5.0 L/min, the pump head in 4.0-7.0 L/min range should not degrade as seen with β_2 40^0.

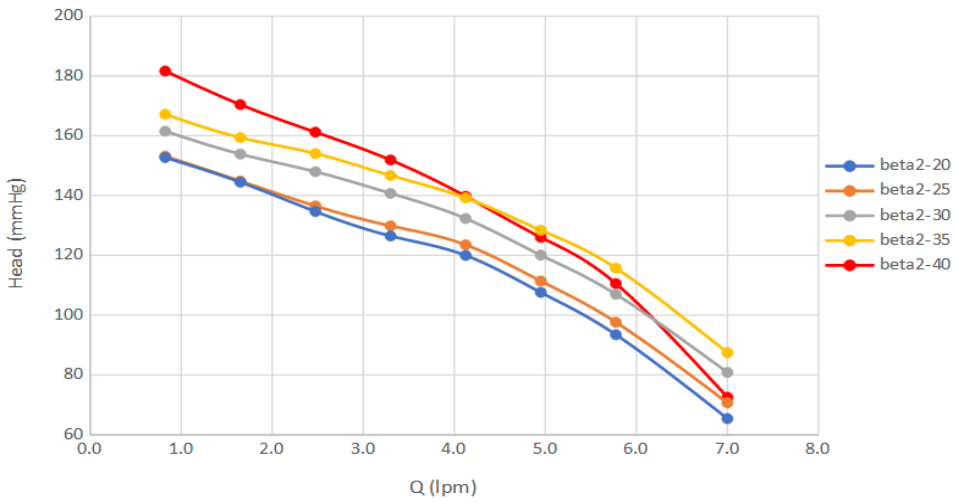

Figure 5.1. Head vs Q for different β_2

Hydraulic efficiency calculation Eq. 5.1 is used where P_{shaft} is power given to rotor, and P_{fluid} is the energy fluid gained in pump. P_{shaft} is taken directly from CFD software while P_{fluid} is calculated according to Eq.5.2. Flow rate Q is in m^3/s, pump head is in m of blood, fluid density ρ is in kg/m^3, earth acceleration constant in m/s^2. Hydraulic efficiency of pump is checked for all β_2 values with different flow rates as shown Figure 5.2. Although efficiency is nearly same for low flow rates, after 4.0 L/min, β_2 35^0 shows

better performance which was expected. So accordingly, β_2 pump is chosen as 35^0 and further studies are performed.

$$\eta = \frac{P_{shaft}}{P_{fluid}} \tag{5.1}$$

$$P_{fluid} = QH\rho g \tag{5.2}$$

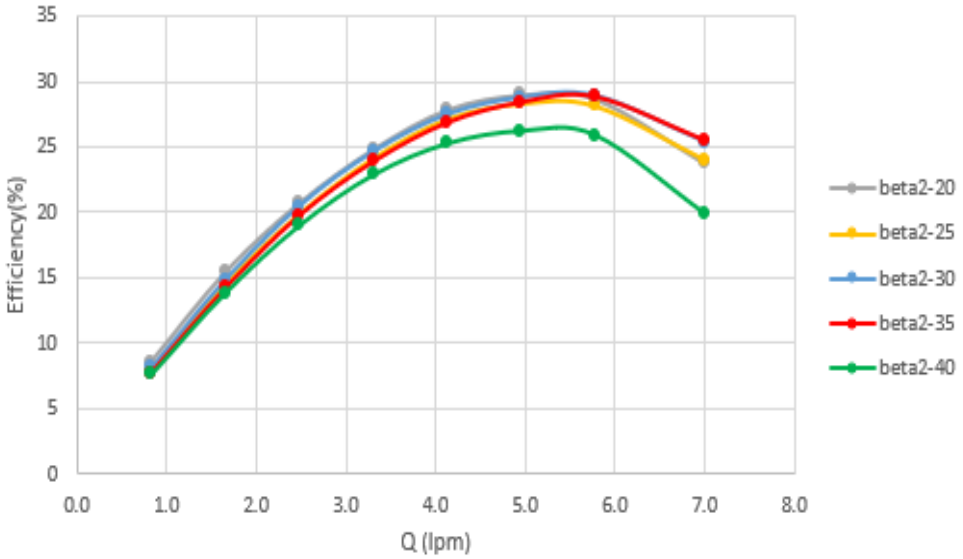

Figure 5.2. Efficiency vs Q for different β_2

Highest efficiency is achieved with 5.8 L/min when β2 is 35 and up-clearance is 2.00 mm. In this configuration, 116 mmHg pump head is achieved with 29% hydraulic efficiency for 2.00 mm up-clearance. Pressure profiles at impeller cross-section for different β2 values at 5.8 L/min, which is BEP, are given in Appendix C. Suction pressure at impeller eye location increases with increasing β_2 values which shows us that $NPSH_R$ is decreasing for higher β_2 values. Blade shape also effects lowest pressure points at blade inlet tips. Lowest pressure values are decreasing with increasing β_2 values at blade tips. Also, velocity profiler for all β2 is given in Appendix C.

Six different up-clearance values between 2mm and 0.1mm are investigated for β_2 35^0. Head vs flow rate and hydraulic efficiency vs flow rate graphics are given in Figure 5.3 and 5.4. As expected, lower up-clearance values results in head increase. This occurs

due to less leakage flow. Pressure profiles and velocity profiles are illustrated in Appendix D.

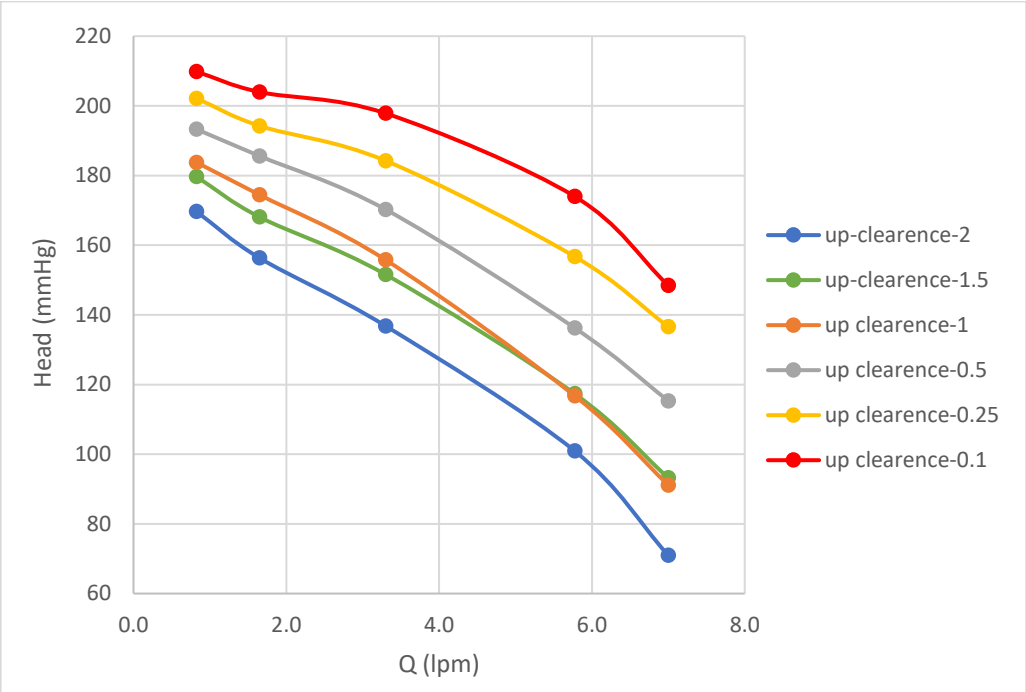

Figure 5.3. Head vs Q for different up-clearance

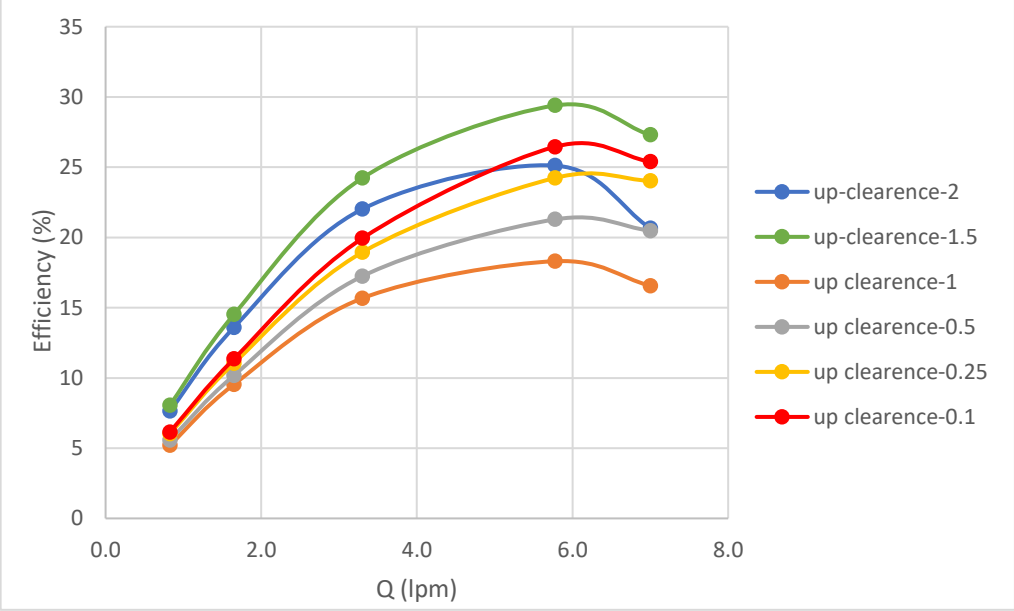

Figure 5.4. Efficiency vs Q for different up-clearance

Efficiency vs flow rate results are a bit more complex then head difference. For lower up-clearance, results are found proportional, with decreasing up-clearance efficiency increases. But for 1.50 mm and 2.00 mm efficiency is higher. This is due to sudden decrease in shaft power for 1.50 mm and 2.00 mm. Shaft powers and fluid powers are summarized in Table 5.1 for 5.8 L/min and 35^0 β_2.

Table 5.1. P_{shaft} and P_{fluid} for different up-clearence at 5.8 L/min and 35^0 β_2

Up-clearance (mm)	P_{shaft} (W)	P_{fluid} (W)
2.00	5.16	1.3
1.50	5.12	1.5
1.00	8.18	1.5
0.50	8.22	1.8
0.25	8.30	2.0
0.10	8.44	2.2

After investigating results, it is seen that required pump head is accomplished with 0.10 mm up-clearance at 35^0 β_2 for 3.3 L/min. Efficiency of pump, 20%, is also satisfactory.

Hemolysis values for different up-clearance values are also studied. Firstly to have an rough idea about where hemolysis occurs more aggressively, wall shear stress values are investigated both for stationary and rotating walls, given in Figure 5.5 and 5.6 respectively. As can be seen from Figure 5.5 at stationary walls, higher up clearance values like 2.00 and 1.50 mm wall shear stress increases at pump throat which is expected and inevitable. This increase can only be lowered by increasing throat clearance which impacts pump head severely. For smaller up clearance values, this increase at stationary walls spreads to upper area of volute. For rotating walls, shear stress decreases with decreasing up-clearance values contrary to stationary walls. As expected shear stress accumulated on blade tips and blade surfaces where blade stand out from rotor. This effects lowers as up-clearance value decreases and average wall shear decreases.

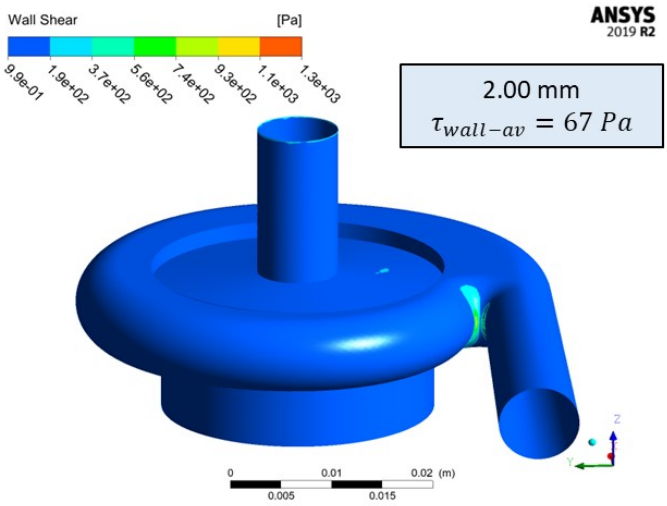
Wall Shear
[Pa]
9.9e-01
1.9e+02
3.7e+02
5.6e+02
7.4e+02
9.3e+02
1.1e+03
1.3e+03
ANSYS
2019 R2
2.00 mm
$\tau_{wall-av} = 67\ Pa$
0
0.01
0.02 (m)
0.005
0.015

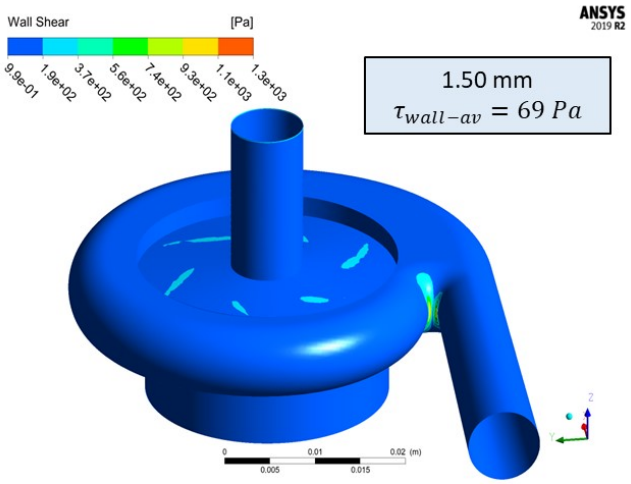
Wall Shear
[Pa]
9.9e-01
1.9e+02
3.7e+02
5.6e+02
7.4e+02
9.3e+02
1.1e+03
1.3e+03
ANSYS
2019 R2
1.50 mm
$\tau_{wall-av} = 69\ Pa$
0
0.01
0.02 (m)
0.005
0.015

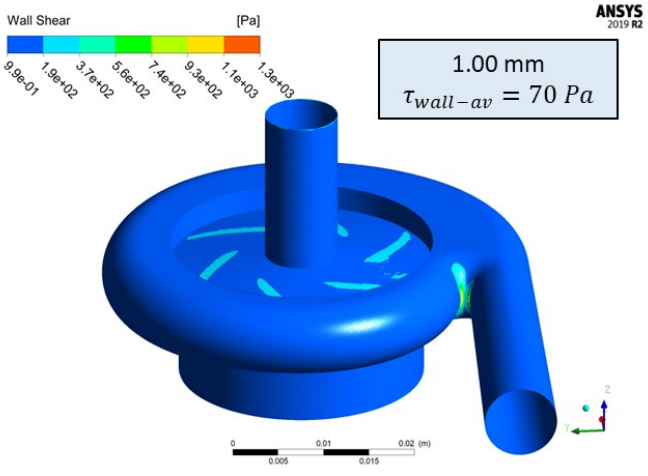
Wall Shear
[Pa]
9.9e-01
1.9e+02
3.7e+02
5.6e+02
7.4e+02
9.3e+02
1.1e+03
1.3e+03
ANSYS
2019 R2
1.00 mm
$\tau_{wall-av} = 70\ Pa$
0
0.01
0.02 (m)
0.005
0.015

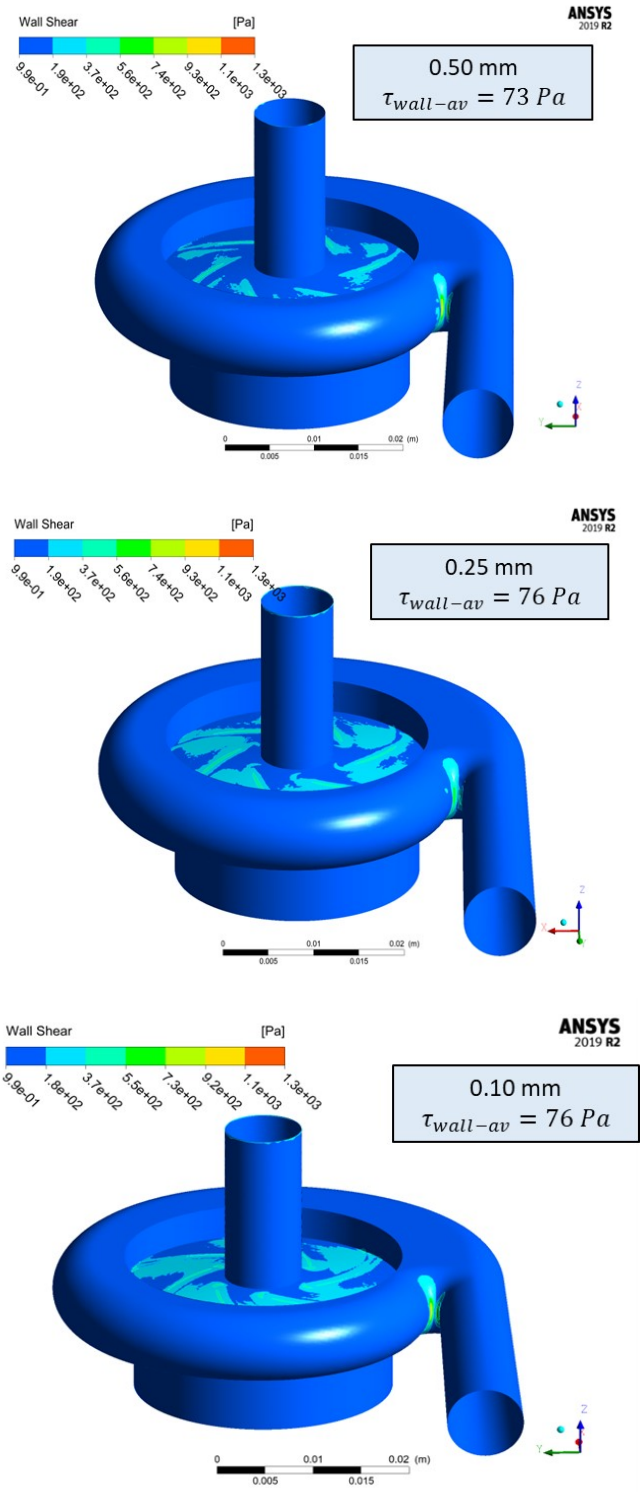

Figure 5.5. Stationary wall shear stress for different up-clearance for 35^0 β_2 at 5.8 L/min

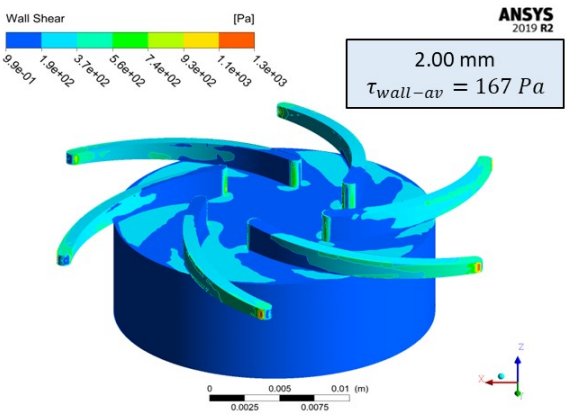
Wall Shear
[Pa]
9.9e-01
1.9e+02
3.7e+02
5.6e+02
7.4e+02
9.3e+02
1.1e+03
1.3e+03
ANSYS
2019 R2
2.00 mm
$\tau_{wall-av} = 167\ Pa$
0
0.005
0.01 (m)
0.0025
0.0075

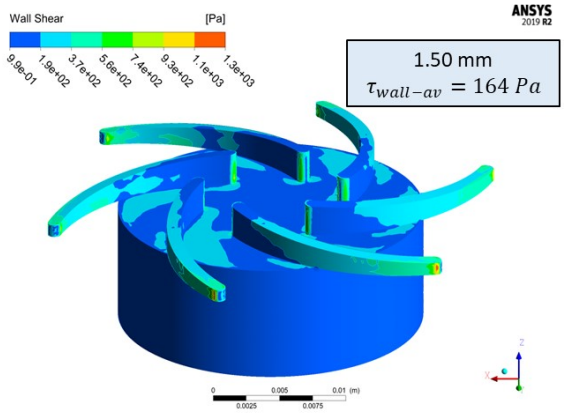
Wall Shear
[Pa]
9.9e-01
1.9e+02
3.7e+02
5.6e+02
7.4e+02
9.3e+02
1.1e+03
1.3e+03
ANSYS
2019 R2
1.50 mm
$\tau_{wall-av} = 164\ Pa$
0
0.005
0.01 (m)
0.0025
0.0075

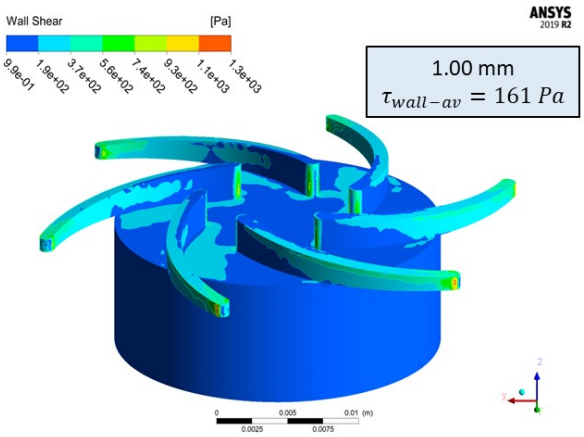
Wall Shear
[Pa]
9.9e-01
1.9e+02
3.7e+02
5.6e+02
7.4e+02
9.3e+02
1.1e+03
1.3e+03
ANSYS
2019 R2
1.00 mm
$\tau_{wall-av} = 161\ Pa$
0
0.005
0.01 (m)
0.0025
0.0075

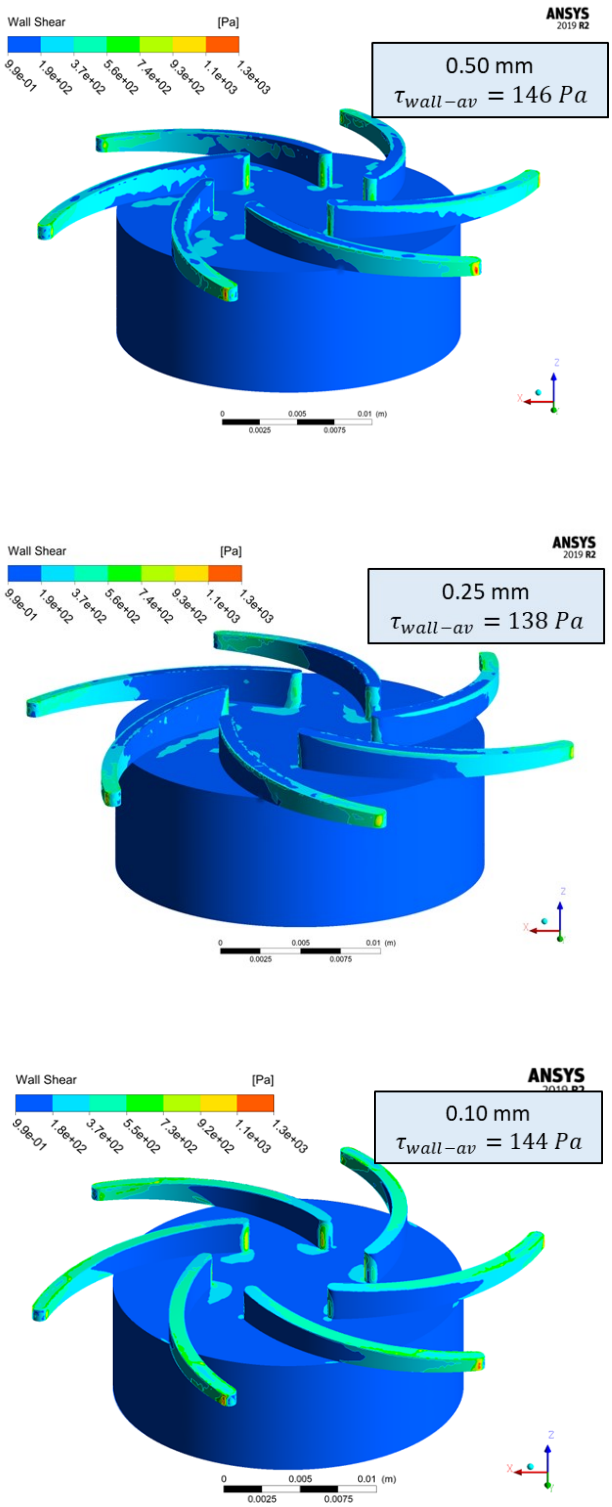

Figure 5.6. Rotating wall shear stress for different up-clearance for 35^0 β_2 at 5.8 L/min

To investigate further scalar shear stress percentage distribution graphics are also examined and given in Figure 5.7 where y axis shows percentage of elements. These distribution graphics are generated for all flow domain not only particle path ways. All histograms show similar patterns but average scalar shear stress decreases with decreasing up-clearance.

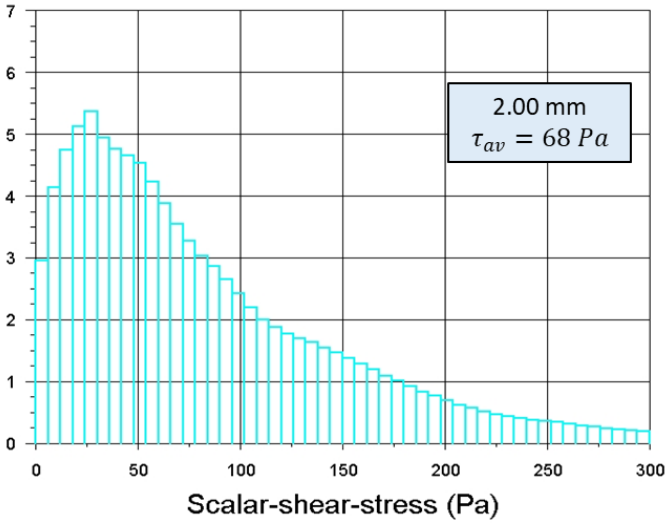

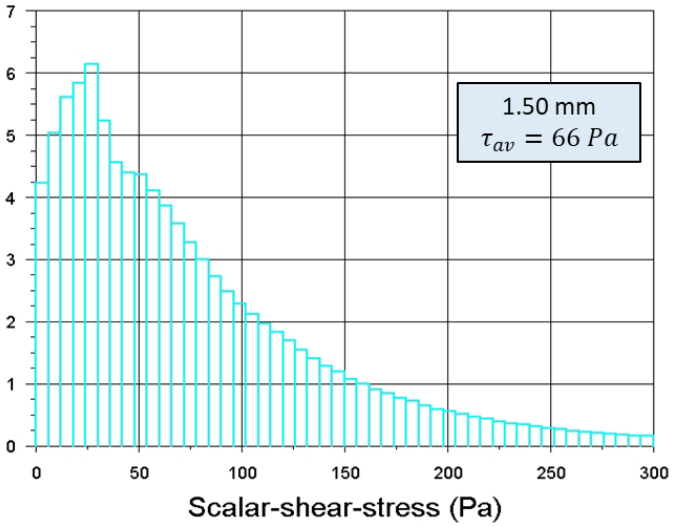

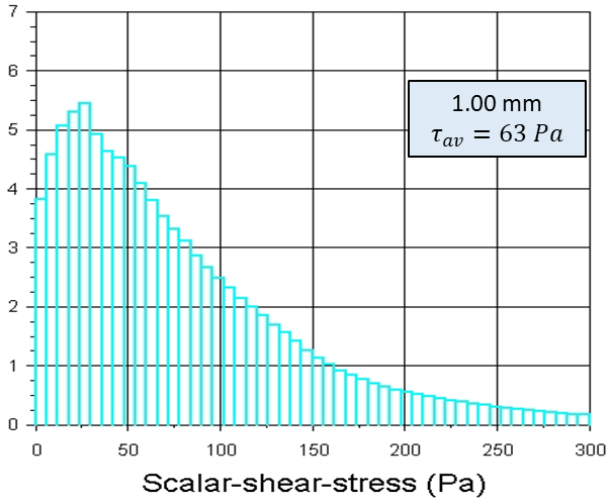
1.00 mm
$\tau_{av} = 63\ Pa$
0
1
2
3
4
5
6
7
0
50
100
150
200
250
300
Scalar-shear-stress (Pa)

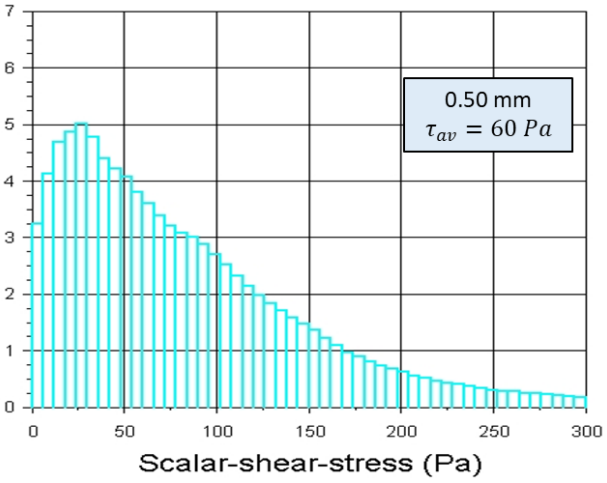
0.50 mm
$\tau_{av} = 60\ Pa$
0
1
2
3
4
5
6
7
0
50
100
150
200
250
300
Scalar-shear-stress (Pa)

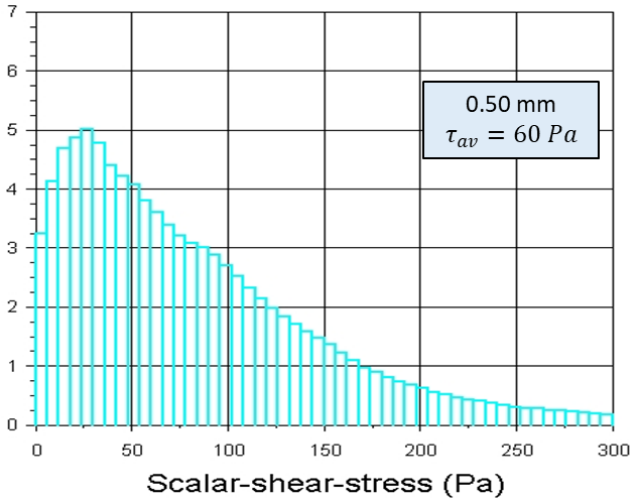
0.50 mm
$\tau_{av} = 60\ Pa$
0
1
2
3
4
5
6
7
0
50
100
150
200
250
300
Scalar-shear-stress (Pa)

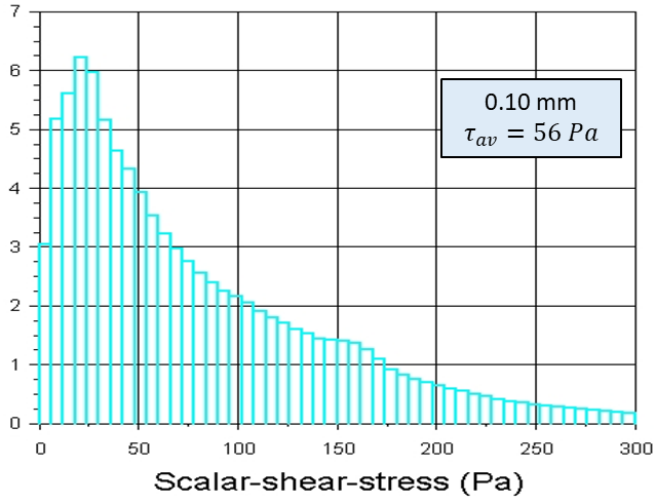

Figure 5.7. Scalar shear stress of all domain for different up-clearance for 35^0 β_2 at 5.8 L/min

Although D index is calculated individual particle time steps and summed, total particle time residence is investigated to have an idea about how quickly particles pass through pump and how does up-clearance effect residence time. Population distribution of particle residence time is given in Figure 5.8 for different up-clearance values. Generally average particle residence time is about 0.2 seconds and residence time ranging from 0.05 to 1.2 seconds. Unfortunately, a clear relationship between up-clearance and residence time is not found. Expectation was to observe decrease in residence time with decreasing up-clearance. This contradiction may arise from several reasons;

- While modelling pump in SolidWorks, 15 mm inlet and 30 mm outlet piping is considered. Particle injection point located at pipe inlet boundary and particles are traced up to outlet pipe boundary. It means a lot of data while calculating these values are come from inlet and outlet piping. This issue may shadowing important data for volute and rotor part.
- In DPM, 100 particles are used to investigate flow properties along path lines. This sampled particles may not represent whole flow domain properties. So more analysis should be made with increased particle number and results should be compared.

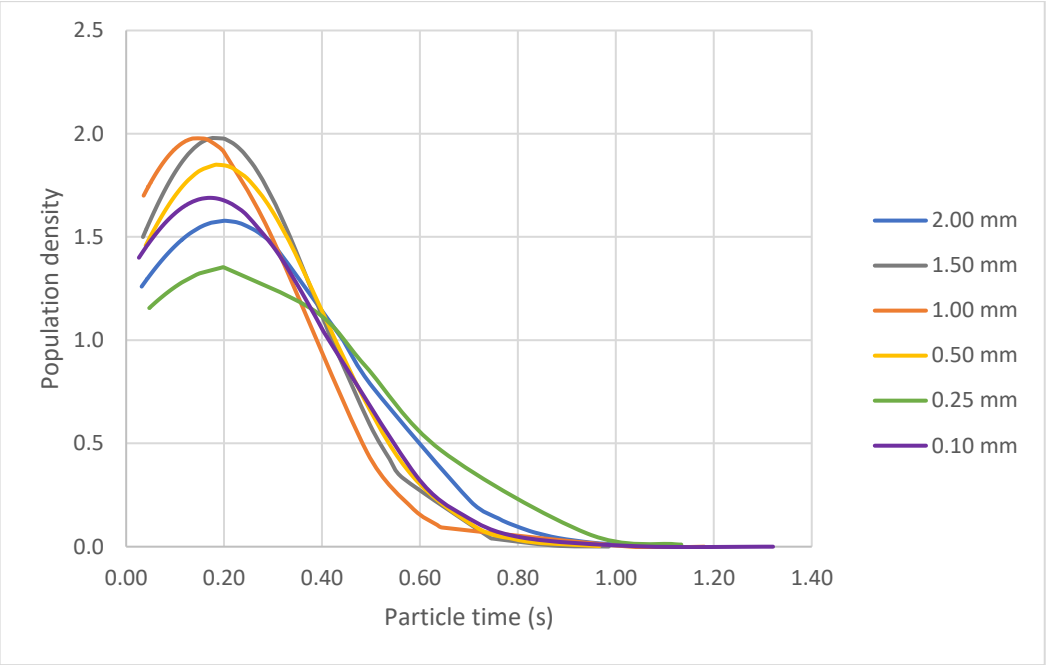

Figure 5.8. Particle time population distribution for different up-clearance for 35^0 β_2 at 5.8 L/min

D-index population distribution is also generated for different up-clearance values given in Figure 5.9. As seen in figure and given in Table 5.2 average D-index for particles range between 0.05 and 0.1 which means 5-10% of total hemoglobin is leaking to plasma for one pass. This value is abnormally high. As seen in Figure 5.10, at tip of the blade scalar shear stress is too high. Probably, these points results in very high D-index. Normally, any point should not exceed 250 Pa which is threshold for hemolysis [34].In Figure 5.11 shows iso-contour which exceeds to 250 Pa. In addition, like particle residence time a clear relationship could not be found with up-clearance. Same reasons stated for residence time is also applicable for D-index. Eulerian method could be employed to overcome particle sampling issues for D-index.

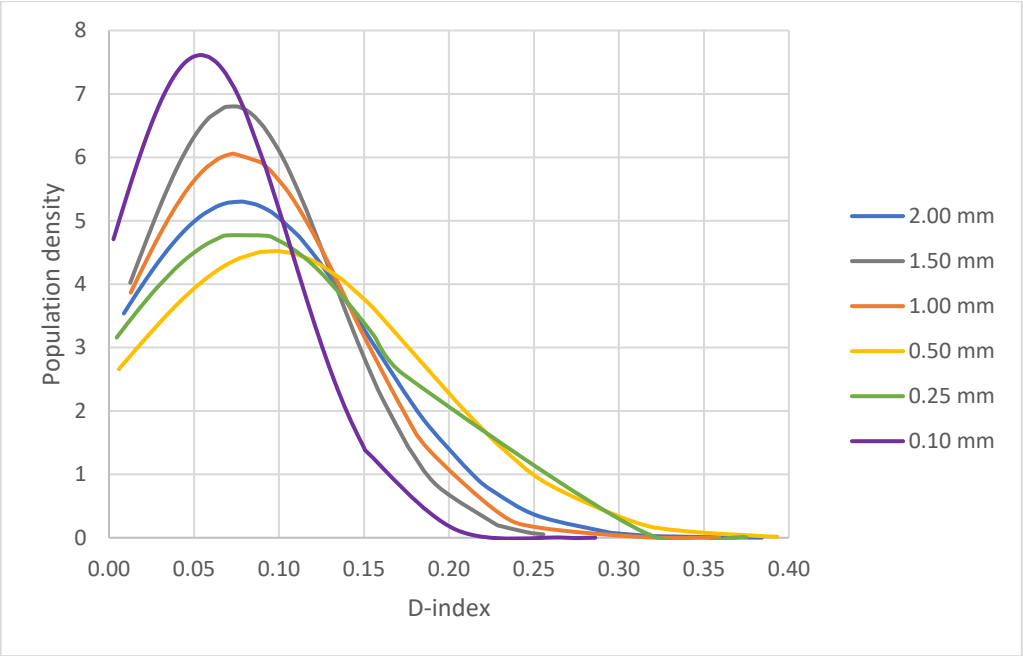

Figure 5.9. D-index population distribution for different up-clearance for 35^0 β_2 at 5.8 L/min

Table 5.2. Average scalar shear stress, particle time and D-index for different up-clearance for 35^0 β_2 at 5.8 L/min

Up-clearance (mm)	Average scalar shear stress (Pa)	Average particle time (s)	Average D-index
2.00	68	0.20	0.08
1.50	66	0.18	0.07
1.00	63	0.15	0.08
0.50	60	0.19	0.10
0.25	56	0.21	0.08
0.10	56	0.17	0.05

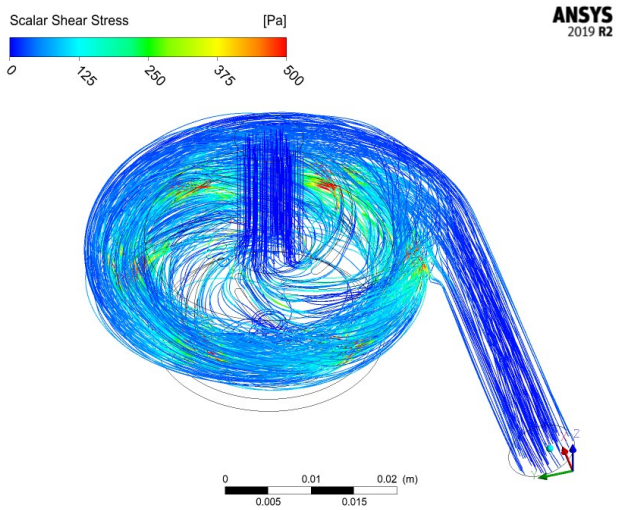

Figure 5.10. Scalar shear stress on particle path lines for 35^0 β_2 at 5.8 L/min for 0.10 mm up-clearance

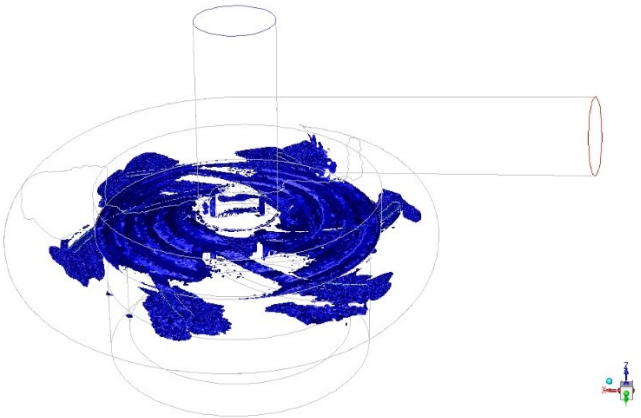

Figure 5.11. Iso-contour higher than 250 Pa for 35^0 β_2 at 5.8 L/min for 0.10 mm up-clearance

To eliminate some possible reasons stated above further investigations is made for particle number and solution domain. Firstly, to decrease generated data and focus on pump impeller zone, inlet and outlet piping of pump is trimmed as shown in Figure 5.12. Comparison between new case and old one for average scalar shear stress in given in Table 5.3. As can be seen table, eliminating inlet and outlet piping does not lead to a visible difference. Still average scalar shear stress is decreasing with decreasing up-clearance values. After trimming inlet and outlet piping, average values for all up-

clearance values are increased as expected because in piping region scalar shear stress is very low.

After that, particle number independence is studied. For 1.0 mm up-clearance, surface injection is applied which corresponds to 978 particles. After particle number is decreased to 600, 400, 200 and finally 100. For 978, 600, 400 and 200 results are very similar but at 100 particles, results diverge. Particle time and D-index for different particle numbers are given at Figure 5.13 and 5.14 respectively for 1.0 mm up-clearance. According to this study it is decided that 200 particles will be applied for comparison of different up-clearance values.

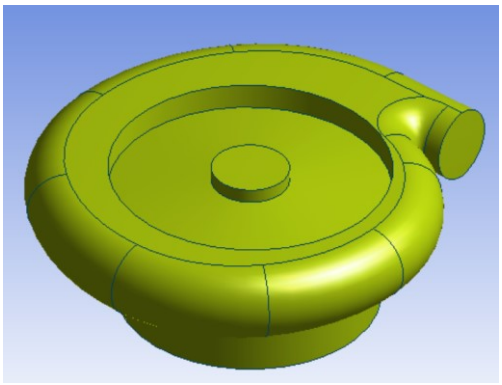

Figure 5.12. Trimmed inlet and outlet of pump

Table 5.3. Average scalar shear stress for different up-clearance for 35^0 β_2 at 5.8 L/min (trimmed case)

Up-clearance (mm)	Average scalar shear stress (Pa)
2.00	80
1.50	77
1.00	73
0.50	70
0.25	68
0.10	68

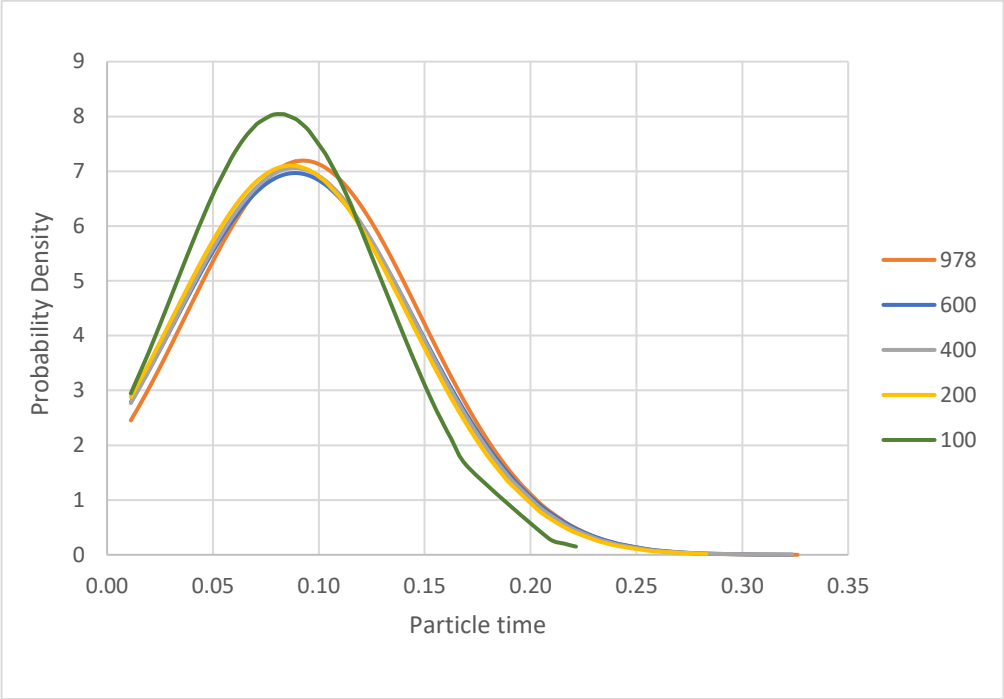

Figure 5.13. Particle time population distribution for different particle number for 35^0 β_2 at 5.8 L/min

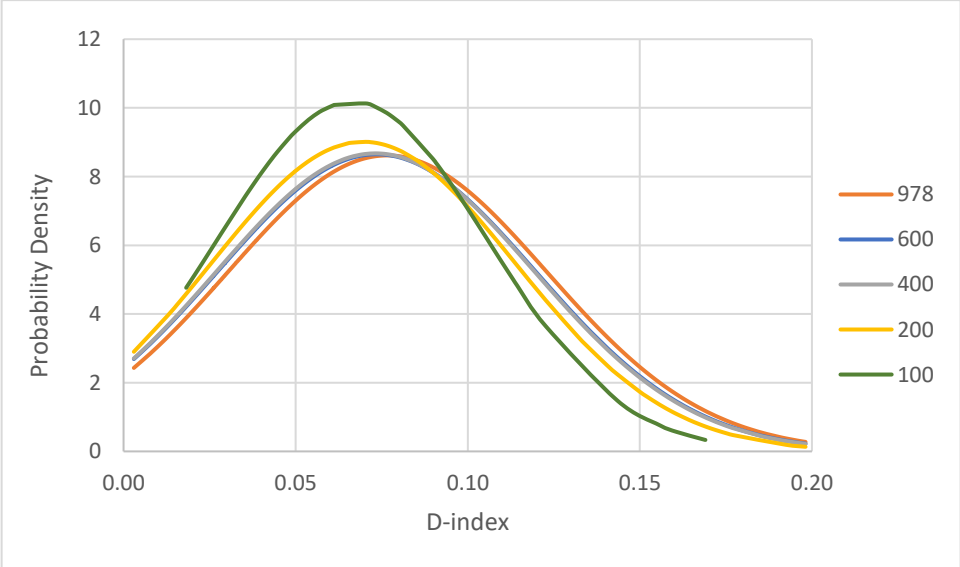

Figure 5.14. D-index population distribution for different particle number for 35^0 β_2 at 5.8 L/min

Population distribution and comparison are given in Figure 5.15 and 5.16 for particle time and D-index respectively. For higher up-clearance values distribution is wider which means at these designs there are more spots with high hemolysis. Also average values are given in Table 5.4. In previous study which was applied 100 particles, there is no any relation with up-clearance and particle time. However, when used 200 particles, it is seen that particle time decreasing by decreasing up-clearance. If D-index is checked for 200 particles, again there is no exact relation but more stable than trial of 100 particles. The least D-index is observed at 0.25 and 0.10 mm up-clearance as previous one. According to this D-index, %4 of total hemoglobin is leaking to plasma for one pass. This value is again too high for blood pump design. Hemolysis does not change greatly.

In further study, hemolysis should be calculated and compared for different impeller discharge angles. Because, the maximum hemolysis is observed at tip of the impeller.

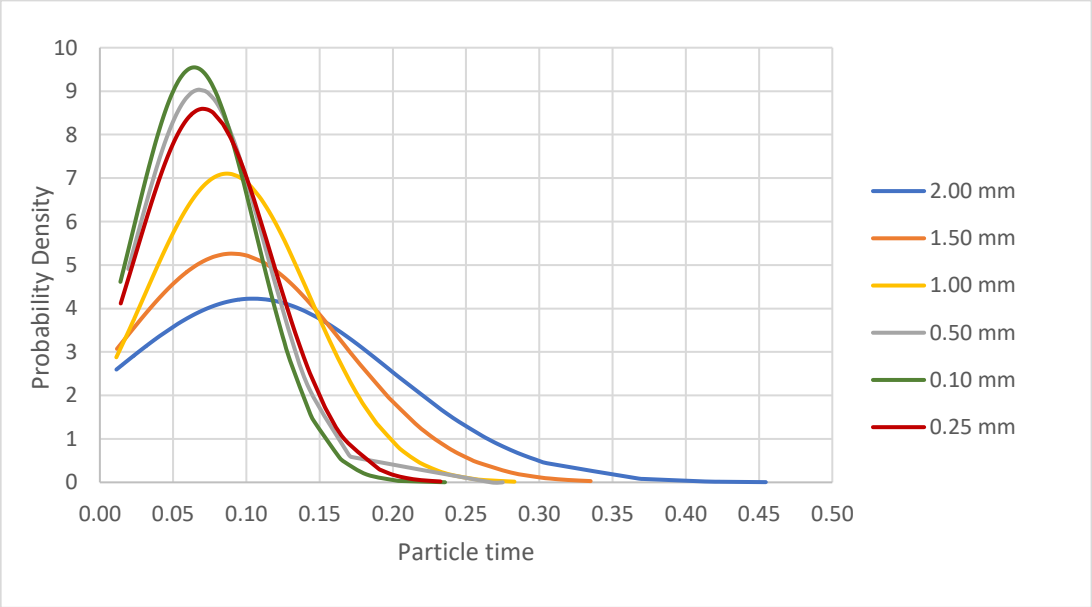

Figure 5.15. Particle time population distribution for different up-clearance for 35^0 β_2 at 5.8 L/min (200 particles)

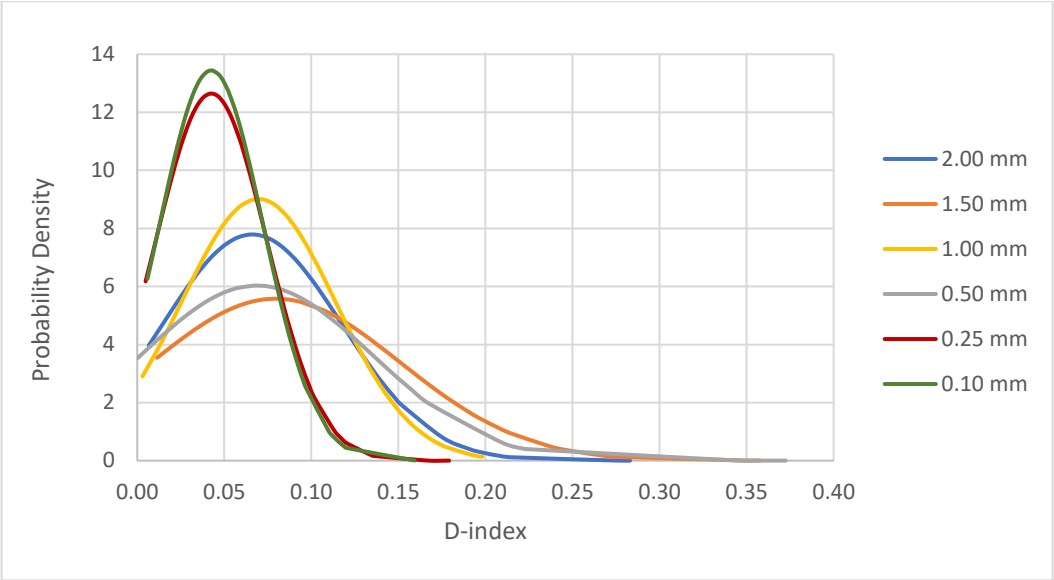

Figure 5.16. D-index population distribution for different up-clearance for 35^0 β_2 at 5.8 L/min (200 particles)

Table 5.4. Particle time and D-index for different up-clearance for 35^0 β_2 at 5.8 L/min (200 particles)

Up-clearance (mm)	Average particle time (s)	Average D-index
2.00	0.10	0.07
1.50	0.09	0.08
1.00	0.09	0.08
0.50	0.07	0.07
0.25	0.07	0.04
0.10	0.06	0.04

REFERENCES

1. 2020. The top 10 causes of death. December 9. Accessed April 18, 2019. https://www.who.int/news-room/fact-sheets/detail/the-top-10-causes-of-death.

2. 2019. *What to know about cardiovascular disease.* July 26. Accessed April 25, 2020. https://www.medicalnewstoday.com/articles/257484.

3. Hannah Ritchie, et al. 2019. *Causes of Death.* December. Accessed January 21, 2020. https://ourworldindata.org/causes-of-death.

4. *Heart Valve Disease.* Accessed May 21, 2020. https://www.montefiore.org/heart-valve-disease.

5. Hannah Ritchie, et al. 2019. *Causes of Death.* December. Accessed January 21, 2020. https://ourworldindata.org/causes-of-death.

6. Accessed February 3, 2020. http://fetaltonewborn.org/hypoplastic-left-heart-syndrome-hlhs/normalheartbloodflow/.

7. Accessed February 4, 2020. https://www.lidco.us/education/cardiac-output.

8. Klabunde, Richard E. 2017. *Cardiovascular Physiology Concepts.* November 22. Accessed May 12, 2019. https://www.cvphysiology.com/Blood%20Pressure/BP019.

9. *Pumping Loss Simple Analysis.* Accessed February 21, 2020. http://zigherzog.net/stirling/DrIz/simple/pumping.html.

10. Kamiya, Akira. 1984. "Adaptive Regulation of Wall Shear Stress Optimizing Vascular Tree Function." In *Mathematical Biology*, 127-137.

11. Sissonss, Claire. 2020. *How much blood is in the human body?* June 7. Accessed July 3, 2020. https://www.medicalnewstoday.com/articles/321122.

12. Tombak, Anıl. 2019. "Introductory Chapter: Erythrocytes - Basis of Life."

13. Çetin, Ayşe. 2018. *YÖK Tez Merkezi.* Accessed 2020. https://tez.yok.gov.tr/UlusalTezMerkezi/tezDetay.jsp?id=gPf_dXPlKj9NHeAyWPDhCA&no=flpUynnDPDTJW1Sf1RWHjw.

14. Pittman, Roland N. 2011. "Regulation of Tissue Oxygenation." *NCBI.* Accessed 2020. https://www.ncbi.nlm.nih.gov/books/NBK54104/.

15. Franco, R. S. 2017. "Measurement of Red Cell Lifesspan and Aging." In *Transfusion Medicine and Hemotherapy*, 302-307.

16. Aryal, Sagar. 2018. *Differences Between Red Blood Cells (RBC) and White Blood Cells (WBC).* June 23. Accessed 2019. https://microbiologyinfo.com/differences-between-red-blood-cells-rbc-and-white-blood-cells-wbc/.

17. Fred G. Pluthero, et al. 2018. *The Birth and Death of Platelets in Health and Disease.* April 11. Accessed 2020.

18. Sonker, Deepak. 2018. "Photoacoustic signal computation from different erythrocytes." *ResearchGate.* August. Accessed 2020. https://www.researchgate.net/publication/329427875_Photoacoustic_signal_computation_from_different_erythrocytes.

19. Maslak, Peter. 2004. *Rouleaux Formation.* December 07. Accessed 2019. https://imagebank.hematology.org/image/2673/rouleaux-formation--1?type=upload.

20. C.R. Huang, et al. 1973. "Rheogoniometric studies of whole human blood at shear rates down to 0.0009 sec−1." In *Biorheology*, 23-28.

21. Ching-Rong Huang, et al. 1995. "Viscoelastic-thixotropy of blood." In *Clinical Hemorheology and Microcirculation*, 25-36.

22. Juntao Zhang, et al. 2006. "Computational and Experimental Evaluation of the Fluid." *Artificial Organs* 171.

23. Dmitry A. Fedosov, et al. 2011. "Predicting human blood viscosity in silico." *PNAS* 11772-11777.

24. "Disease in patients with obstructive sleep apnea syndrome (OSAS)." *Folia Histochemica et Cytobiologica* 206-210.

25. Leo, Jeffrey A. 2019. "Shear-thinning behaviour of blood in response to activehyperaemia: Implications for the assessment of arterial shearstress-mediated dilatation." *Experimental Physiology* 244-257.

26. Samuel J. Hund, et al. 2016. "A Quasi-Mechanistic Mathematical Representation for Blood Viscosity." *MDPI.* November 16. Accessed 2020. https://www.mdpi.com/2311-5521/2/1/10/htm.

27. Young, Wen-Bin. 2002. "Underfill Viscous Flow Between Parallel Plates and Solder Bumps." *IEE Transactions on Components and PAckaging Technologies* 695-700.

28. Ken-ichi Tsubota, et al. 2010. "Elastic force of red blood cell membrane during tank-treading motion: Consideration of the membrane's natural state." *International Journal of Mechanical Sciences* 356-364.

29. Jules Dupire, et al. 2012. "Full dynamics of a red blood cell in shear flow." *PNAS.*

30. Arora, Dhruv. 2004. "A Tensor-based Measure for Estimating Blood Damage." *Artificial Organs* 1002-1015.

31. *Strain.* Accessed 2020. http://www.continuummechanics.org/strain.html.

32. 2006. "Computational hemodynamics: Hemolysis and viscoelasticity." *RICE.* Accessed 2020. https://scholarship.rice.edu/handle/1911/18870.

33. 2018. *Serum free hemoglobin test.* January 19. Accessed 2020. https://www.ucsfhealth.org/medical-tests/serum-free-hemoglobin-test.

34. Hai Yu, et al. 2017. "A Review of Hemolysis Prediction Models for Computational Fluid Dynamics." *Artificial Organs* 603-621.

35. Tanu Goyal, et al. 2015. "Validation of Hemolysis Index Thresholds Optimizes Detection of Clinically Significant Hemolysis ." *American Journal of Clinical Pathology* 579-583.

36. *Castle Pumps.* Accessed 2020. https://www.castlepumps.com/info-hub/positive-displacement-vs-centrifugal-pumps/.

37. Karassik, Igor J. 1986. "Introduction: Classification and Selection of Pumps & Centrifugal Pump Theory." In *Pump Handbook*, 1.3-2.31.

38. *Useful information on positive displacement pumps.* Accessed 2020. https://www.michael-smith-engineers.co.uk/resources/useful-info/positive-displacement-pumps.

39. B., Adam. 2016. *Positive Displacement Pump Types.* August 25. https://www.youtube.com/watch?v=4OJTN0M1DBk.

40. *Centrifugal Pump: Chemical Files.* Accessed 2020. https://chemicalscouts.wordpress.com/2011/07/14/centrifugal-pump/.

41. Wolfgang Boettcher, et al. 2003. "History of Extracorporeal Circulation:The Invention and Modification of Blood Pumps." *The Journal of The American Society of Extra-Corporeal Technology* 184-191.

42. Wolfgang Boettcher, et al. 2003. "History of Extracorporeal Circulation: The Conceptional and Developmental Period." *The Journal of Extra-corpereal Technology* 172-183.

43. Jooli Han, et al. 2019. " Cardiac Assist Devices: Early Concepts, Current Technologies, and Future Innovations." *Bioengineering* 6-18.

44. Anatol Prinzig, et al. 2016. "Left ventricular assist devices—current state and perspectives." *Journal of Thoracic Disease* 8.

45. Ruangpratyakul. 2018. *Ventricular Assist Device.* May 13. Accessed 2019. https://www.slideshare.net/degnarog/ventricular-assist-devices-96876335.

46. Kahan. 2018. *Design Analysis and Development of Miniature Blood Pump.* July. Accessed 2020. https://tez.yok.gov.tr/UlusalTezMerkezi/.

47. Önder. 2019. *Design and hydraulic performance determination of a centrifugal blood pump with hydrodynamic journal bearing.* December. Accessed 2020. https://tez.yok.gov.tr/UlusalTezMerkezi/.

48. John, Ranjit. 2008. "Current Axial-Flow Devices—the HeartMate II and Jarvik 2000 Left Ventricular Assist Devices." *ScienceDirect* 264-272.

49. Toptop. 2013. *Computational Fluid Dynamics Analysis of Axial Flow Left Ventricular Flow Assist Device.* Accessed 2020. https://tez.yok.gov.tr/UlusalTezMerkezi/.

50. 2016. *Spiral groove bearings.* December 4. Accessed 2020. http://www.omega-dot.com/air-bearings/spiral-groove-thrust/.

51. Toulas. (2019, October 21). *Magnetic Bearings – The mechanical engineer's guide*. Retrieved from engineeringclicks: https://www.engineeringclicks.com/magnetic-bearing/

52. Yang Fu, e. a. (2019). The Impact of Pulsatile Flow on Suspension Force for Hydrodynamically Levitated Blood Pump. *Journal of Healthcare Engineering*, 1-6.

53. Thomas Lile, e. a. (2016, August 3). *Cardiac Pump For Fontan Patients.* Retrieved from http://courses.washington.edu/bioeteam/ProposalPresents2016/TeamPresentation_LLL_Fontanella.pdf

54. *Ventricular Assist Devices.* https://www.texasheart.org/heart-health/heart-information-center/topics/ventricular-assist-devices/.

55. Joy. 2016. *Living for Years Without a Heart Is Now Possible.* September 6. Accessed 2019. https://healthblog.uofmhealth.org/heart-health/living-for-years-without-a-heart-now-possible.

56. Inas Mohammed, et al. 2014. "Building a Bridge to Save a Failing Ventricle: Radiologic Evaluation of Short- and Long-term Cardiac Assist Devices." *RadioGraphics* 327-356.

57. Harris. 2012. "Ventricular Assist Devices." *Continuing Education in Anaesthesia Critical Care & Pain* 145-151.

58. Mohite, Prashant. 2014. "Short-term ventricular assist device in post-cardiotomy. ." *Artif Organs.*

59. Otman. 2018. *Popular HeartMate 3 Now Available for Long-Term Use.* November 29. Accessed 2020. https://labblog.uofmhealth.org/rounds/popular-heartmate-3-now-available-for-long-term-use.

60. Briks. 2019. *Intermediate- and long-term mechanical circulatory support.* March 22. Accessed 2020. https://sso.uptodate.com/contents/intermediate-and-long-term-mechanical-circulatory-support?topicRef=1492&source=see_link.

61. Sasaoka, Taro. 2010. "Improved long-term performance of pulsatile extracorporeal left ventricular assist device." *ScienceDirect* 220-228.

62. Valluvan Jeevanandami, et al. 2020. *Short-term mechanical circulatory assist devices.* September 3. Accessed 2020. https://sso.uptodate.com/contents/short-term-mechanical-circulatory-assist-devices?topicRef=3459&source=see_link.

63. 2020. *Heart Failure.* May 29. Accessed 2020. https://www.mayoclinic.org/diseases-conditions/heart-failure/symptoms-causes/syc-20373142.

64. 2015. *Heart Attack and Sudden Cardiac Arrest Differences.* July 31. Accessed 2019. https://www.heart.org/en/health-topics/heart-attack/about-heart-attacks/heart-attack-or-sudden-cardiac-arrest-how-are-they-different.

65. Suneet N. Purohit, et al. 2018. *Living Without a Pulse.* June 14. Accessed 2019. https://www.ahajournals.org/doi/10.1161/CIRCHEARTFAILURE.117.004670.

66. **A**llen Cheng, et al. 2014. *Comparison of continuous-flow and pulsatile-flow left ventricular assist devices: is there an advantage to pulsatility?* . November. Accessed 2020. http://www.annalscts.com/article/view/5143.

67. Baric. 2014. "Why pulsatility still matters: a review of current knowledge." *Croatian Medical Journal* 609-620.

68. Millar. 2018. "Chapter 25 - The past, present, and future." *ScienceDirect.* Accessed 2020. https://www.sciencedirect.com/science/article/pii/B9780128104910000254.

69. Igor Gosev, et al. 2018. "Long-Term Survival in Patients Receivinga Continuous-Flow Left Ventricular Assist Device." *The Annals of Thoracic Surgery* 696-701.

70. Vural. 2008. "Ventricular assist device applications." *Anadolu Kardiyoloji Dergisi* 117-130.

71. *What are the differences between LVAD and the TAH.* Accessed 2020. https://syncardia.com/patients/media/blog/2018/05/what-are-the-differences-between-an-lvad-and-the-tah/.

72. Gazi Kocak, et al. 2017. "Energy efficiency analysis of a ship's centralcooling system using variable speed pump." *Journal of Marine Engineering & Technology.*

73. Timms. 2005. *Design, Develpment and Evaluation of Centrifugal Ventricular Assist Devices.* Accessed 2020. https://core.ac.uk/download/pdf/10885541.pdf.

74. Peng Fang, et al. 2020. "Impeller (straight blade) design variations and their influence on the performance of a centrifugal blood pump." *The International Journal of Artificial Organs* 782-795.

75. Kurt A. Dasse, et al. 2012. "Assessment of Hydraulic Performance and Biocompatibility of a MagLev Centrifugal Pump System Designed for Pediatric Cardiac or Cardiopulmonary Support." *NCBI.* February 23. Accessed 2020. https://www.ncbi.nlm.nih.gov/pmc/article.

76. Gülich. 2008. "Pump types and performance data." In *Centrifugal Pumps*, 65.

77. Tuğrul. 2015. *Design, Construction and Performance Evaluation of a Centrifugal Pump for an Energy Efficient Dishwasher.* December. Accessed 2020. http://etd.lib.metu.edu.tr/upload/12619588/index.pdf.

78. İpci. *Karmaşık Mühendislik Problemlerinin Çözümünde Meshin Önemi.* Accessed 2020. https://slideplayer.biz.tr/slide/14760959/.

79. Wimshurst. 2018. *[CFD] What are Wall Functions and How do they work?* September 22. Accessed 2019. https://www.youtube.com/watch?v=fJDYtEGMgzs.

80. 2001. *Chapter 10. Modeling Turbulence.* Accessed 2020. https://www.afs.enea.it/fluent/Public/Fluent-Doc/PDF/chp10.pdf.

81. 2015. *Langley Research Center Turbulence Modeling Resource.* Accessed 2020. https://turbmodels.larc.nasa.gov/bsl.html.

82. Voigt, Lars Køllgaard. 2007. *Comparison of Turbulence Models for Numerical Calculation of Airfow in an annex 20 Room.* Accessed 2020. http://www.adaptive-research.com/pdfs/turbulent%20models%20-%20comparison.pdf.

83. 2016. *Considerations of Stress Limiter for the SST Turbulence Model in Dual Throat Nozzle Predictions.* Accessed 2020. http://iccfd9.itu.edu.tr/assets/pdf/papers/ICCFD9-2016-123.pdf.

84. Yue Wu, et al. 2017. "Design and Hemocompatibility Analysis of a Double-Suction Injection Suspension Blood Pump Using Computational Fluid Dynamics Methods." *Artificial Organs* 979-987.

85. Taskin, M. Ertan. 2010. *Computational Characterization of Flow and Hemolytic.* Accessed 2020. https://onlinelibrary.wiley.com/doi/pdf/10.1111/j.1525-1594.2010.01017.x.

86. Kennington, J. R. 2011. "Design Optimization and Performance Studies of an Adult Scale Viscous Impeller Pump for Powered Fontan in an Idealized TotalC avopulmonary Connection." *Cardiovascular Engineering and Technology* 237–243.

87. Tetsuya Yano, et al. 2003. "An Estimation Method of Hemolysis within an Axial Flow Blood Pump by Computational Fluid Dynamics Analysis ." *Artificial Organs* 920-925.

APPENDICES

APPENDIX A. CALCULATION FOR DESIGN

Example calculation given in this appendices are based on values given below.

Table A.1. Design Parameters

Symbol	Unit	Value
N	rpm	5000
Q	L/min	3.3
H	mmHg	300

$P = mgH = \rho QgH$

$\rho_{Hg} Q g H_{Hg} = \rho_{blood} Q g H_{blood}$

Q and g are same for mercury and blood so it can be simplified this equation as below.

$\rho_{Hg} H_{Hg} = \rho_{blood} H_{blood}$

$13.53 \frac{g}{cm^3} * 300\ mmHg = 1.06 \frac{g}{cm^3} * H_{blood}$

$H_{blood} = 3.82\ mblood$

$Q = 3.3 \frac{L}{min} * \frac{10^{-3} m^3}{1\ L} * \frac{1\ min}{60\ s} = 5.5 * 10^{-5}\ m^3/s$

$N_{Sm} = \frac{N\sqrt{Q}}{H^{0.75}} = \frac{5000 * \sqrt{(5.5 * 10^{-5})}}{3.82^{\ 0.75}} = 14$

$\mu = 1 - \frac{\pi sin\beta_2}{z} = 1 - \frac{\pi \sin(25^0)}{6} = 0.78$

$u_2 = \sqrt{\frac{2gH}{\psi}} = \sqrt{\frac{2 * 9.81 * 3.82}{1}} = 8.7\ m/s$

$c_{m3} = \left(\frac{c_{m3}}{u_2}\right)_{graph} u_2 = 0.06 * 8.7 = 0.5\ m/s$

$$c_{u3} = u_2 - c_{m3}cot\beta_2 = 8.7 - 0.5 * \cot(25^0) = 7.6\ m/s$$

$$c'_{u3} = \mu c_{u3} = 0.78 * 7.6 = 5.9\ m/s$$

$$D_2 = \frac{60 * u_2 * 1000}{\pi N} = \frac{60 * 8.7 * 1000}{\pi * 5000} \cong 35\ mm$$

$$r_2 = \frac{D_2}{2} = \frac{35}{2} = 17.5\ mm$$

$$b_2 = \frac{Q * 10^6}{2\pi r_2 c_{m3}} = \frac{5.5 * 10^{-5} * 10^6}{2\pi * 0.0175 * 0.5} = 0.9\ mm$$

$$D_1 = 2897 * \left(\frac{Q}{kNtan\beta_0}\right) = 2987 * \left(\frac{5.5 * 10^{-5}}{1 * 5000 * \tan(17^0)}\right)^{\frac{1}{3}} = 10\ mm$$

$$r_1 = \frac{D_1}{2} = \frac{10}{2} = 5\ mm$$

$$r_{1m} = \sqrt{\frac{r_1^2 + r_H^2}{2}} = \sqrt{\frac{5^2 + 0^2}{2}} = 3.5\ mm$$

$$\frac{r_{1m}}{r_2} = \frac{3.5}{17.5} = 0.2 < 0.5$$

Below equation was solved by using 'excel solver'.

$$tan\beta_1 = \frac{tan\beta_0}{1 - \frac{zs_1}{2\pi r_1 sin\beta_1}} \rightarrow\ \beta_1 = 28^0$$

$$c_{m0} = \frac{Q * 10^6}{\pi r_1^2} = \frac{5.5 * 10^{-5} * 10^6}{\pi * 5^2} = 0.7\ m/s$$

$$u_1 = \frac{\pi r_1 N}{30 * 1000} = \frac{\pi * 5 * 5000}{30 * 1000} = 2.6\ m/s$$

$$A_1 = \pi r_1^2 sin\beta_1 = \pi * 5^2 * \sin(28^0) = 37\ mm^2$$

$$A_2 = b_2(2\pi r_2 sin\beta_2 - zs_2) = 0.9 * (2 * \pi * 17.5 * \sin(25^0) - 6 * 1) = 36\ mm^2$$

$$\frac{A_2}{A_1} = \frac{36}{37} = 0.97 < 1.3$$

$$c_{thr} = \left(\frac{c_{thr}}{u_2}\right)_{graph} \quad u_2 = 0.15 * 8.7 = 1.3\ m/s$$

$$A_{thr} = \frac{Q * 10^6}{c_{thr}} = \frac{5.5 * 10^{-5} * 10^6}{1.3} = 42\ mm^2$$

$$r_{thr} = \sqrt{\frac{A_{thr}}{\pi}} = \sqrt{\frac{42}{\pi}} = 3.6\ mm$$

$$t = 0.07 * r_2 = 0.07 * 17.5 = 1.2\ mm$$

$$r_4 \cong r_2 + t + r_{thr} = 17.5 + 1.2 + 3.6 = 22.3\ mm$$

For volute central angle is 45^0;

$$A_v = A_{thr} * \frac{\varphi_v}{360} = 42 * \frac{45}{360} = 5.3\ mm^2$$

$$r_{long} = 4\ mm$$

$$r_{short} = \frac{A_v}{\pi r_{long}} = \frac{5.3}{\pi * 4} = 0.4\ mm$$

$$r_v = r_2 + t + r_{short} = 17.5 + 1.2 + 0.4 = 19.1\ mm$$

$$v = \frac{Q * \frac{\varphi_v}{360}}{A_v} = \frac{5.5 * 10^{-5} * \frac{45}{360}}{5.3 * 10^{-6}} = 1.3\ m/s$$

Table A.2. Results for drawing volute

Symbol	**Unit**	**Value**								
φ_v	degree	**0**	**45**	**90**	**135**	**180**	**225**	**270**	**315**	**360**
A_v	mm^2	0	5.3	10.5	15.8	21.0	26.3	31.5	36.8	42
r-short	mm	0	0.4	0.8	1.3	1.7	2.1	2.5	2.9	3.3
r_v	mm	18.7	19.1	19.4	20.0	20.4	20.8	21.2	21.6	22.0
v	m/s	-	1.3	1.3	1.3	1.3	1.3	1.3	1.3	1.3

APPENDIX B. MESH STRUCTURE

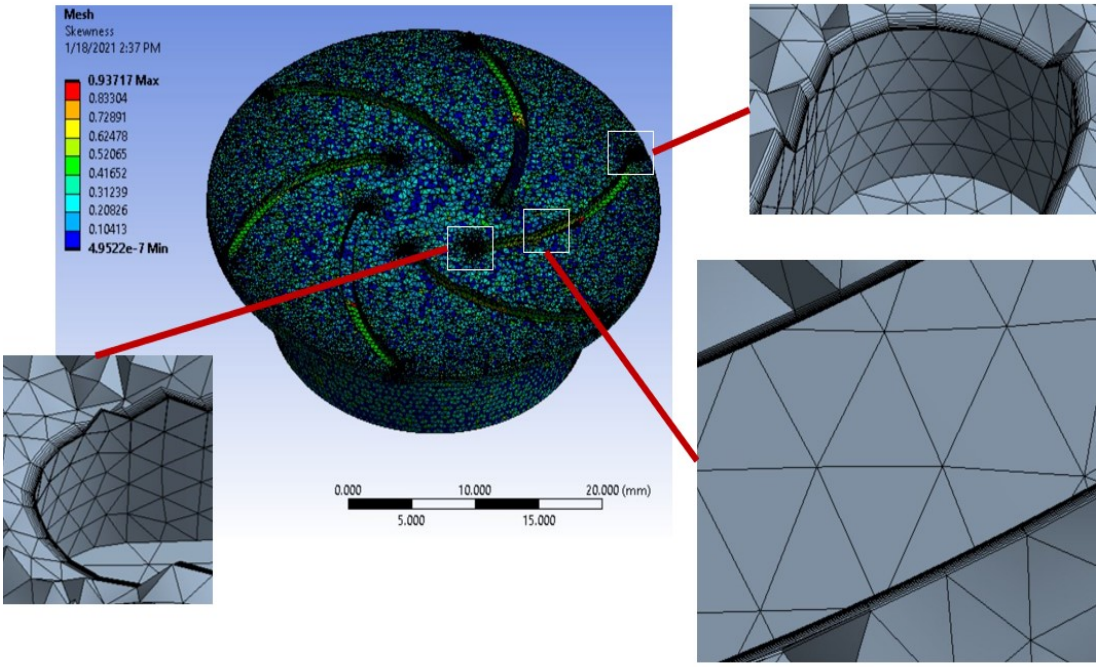

Figure B.1. Mesh structure from top view

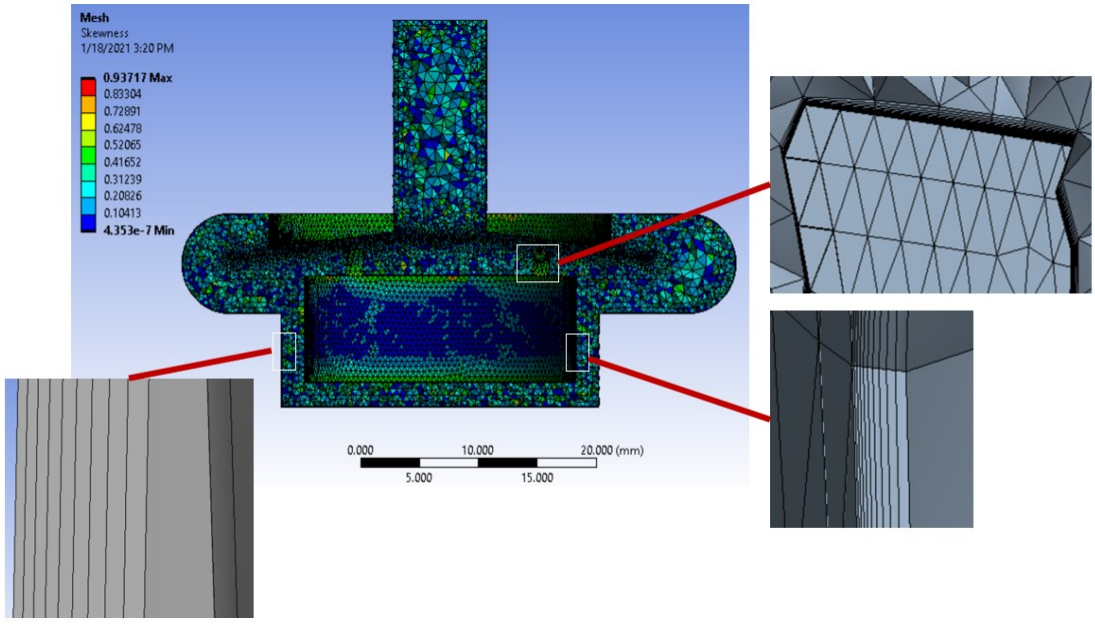

Figure B.2. Mesh structure from side view

APPENDIX C. PRESSURE & VELOCITY PROFILES FOR DIFFERENT β_2

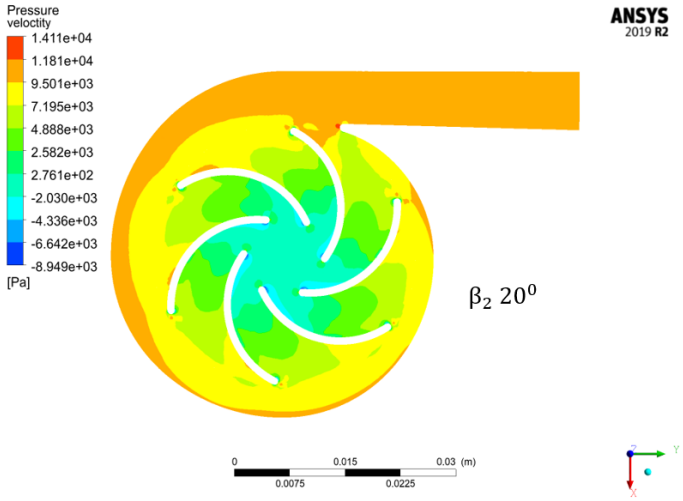

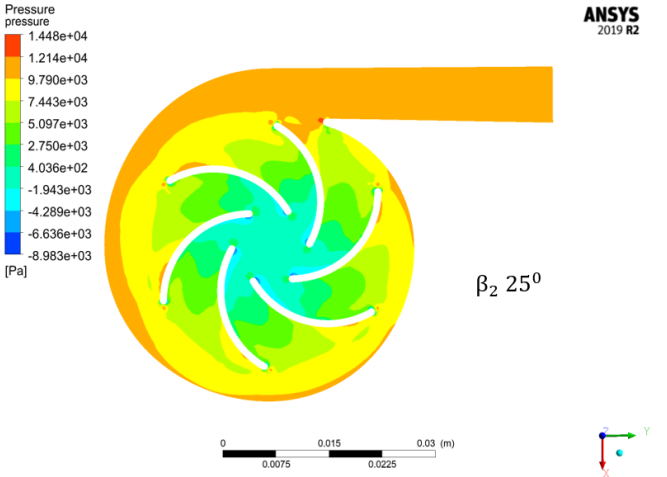

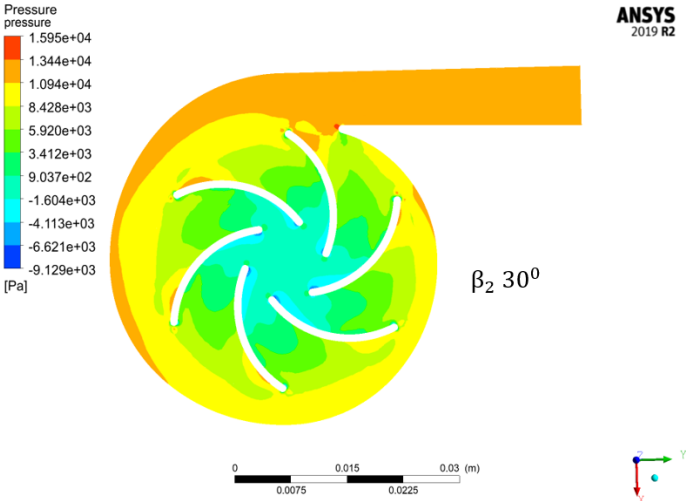

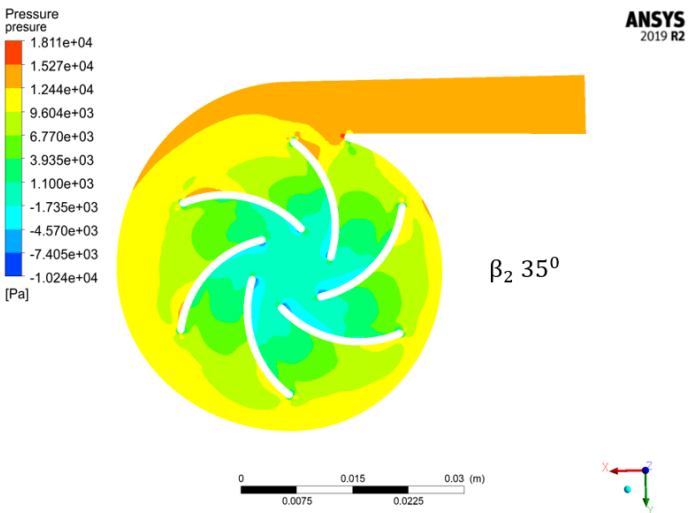

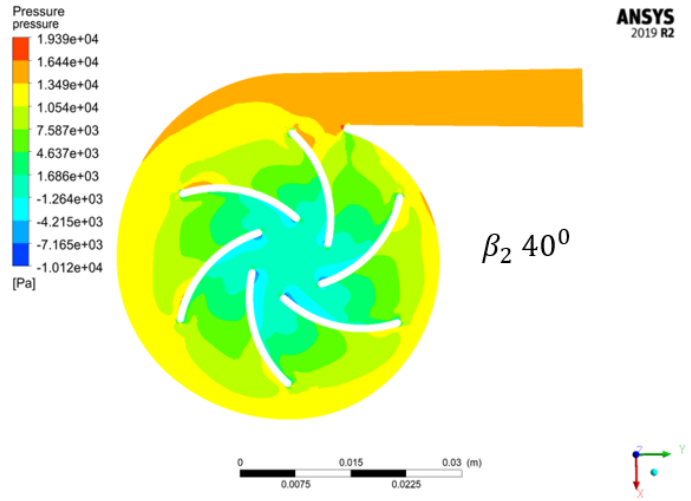

Figure C.1. Pressure profiles for different β2 for up-clearance 2.00 mm at 5.8 L/min

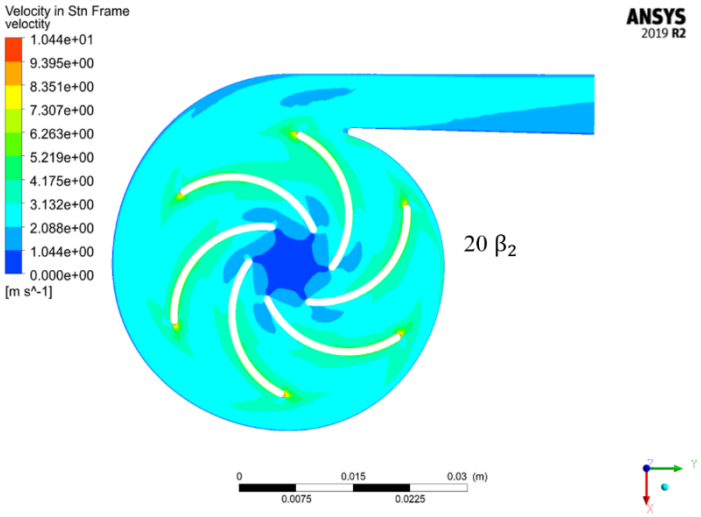
Velocity in Stn Frame
velocity
1.044e+01
9.395e+00
8.351e+00
7.307e+00
6.263e+00
5.219e+00
4.175e+00
3.132e+00
2.088e+00
1.044e+00
0.000e+00
[m s^-1]
ANSYS
2019 R2
20 β2
0
0.015
0.03 (m)
0.0075
0.0225

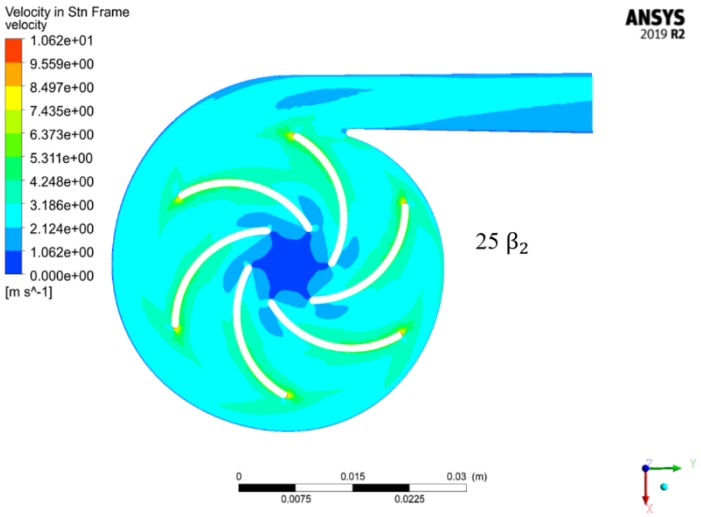
Velocity in Stn Frame
velocity
1.062e+01
9.559e+00
8.497e+00
7.435e+00
6.373e+00
5.311e+00
4.248e+00
3.186e+00
2.124e+00
1.062e+00
0.000e+00
[m s^-1]
ANSYS
2019 R2
25 β2
0
0.015
0.03 (m)
0.0075
0.0225

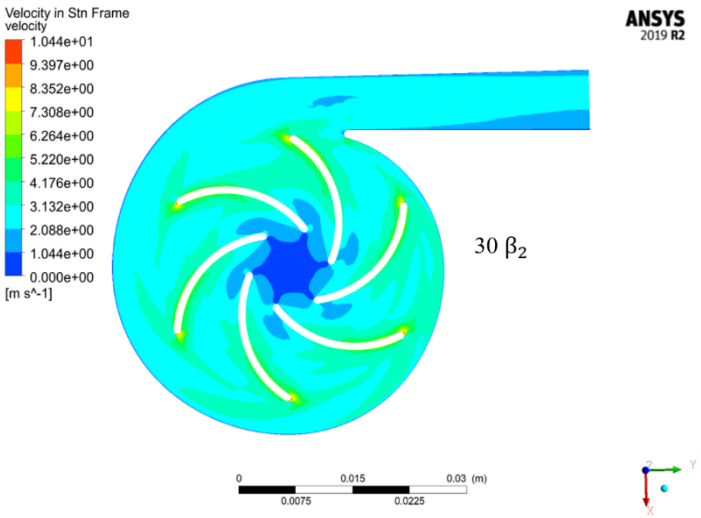
Velocity in Stn Frame
velocity
1.044e+01
9.397e+00
8.352e+00
7.308e+00
6.264e+00
5.220e+00
4.176e+00
3.132e+00
2.088e+00
1.044e+00
0.000e+00
[m s^-1]
ANSYS
2019 R2
30 β2
0
0.015
0.03 (m)
0.0075
0.0225

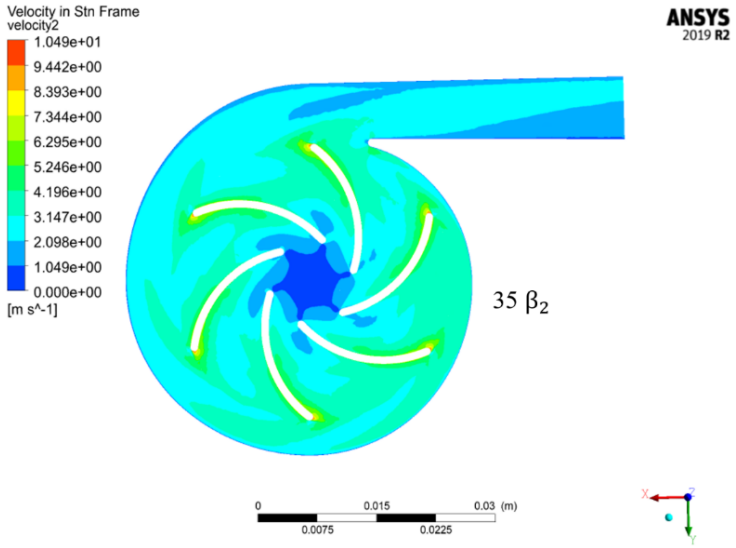

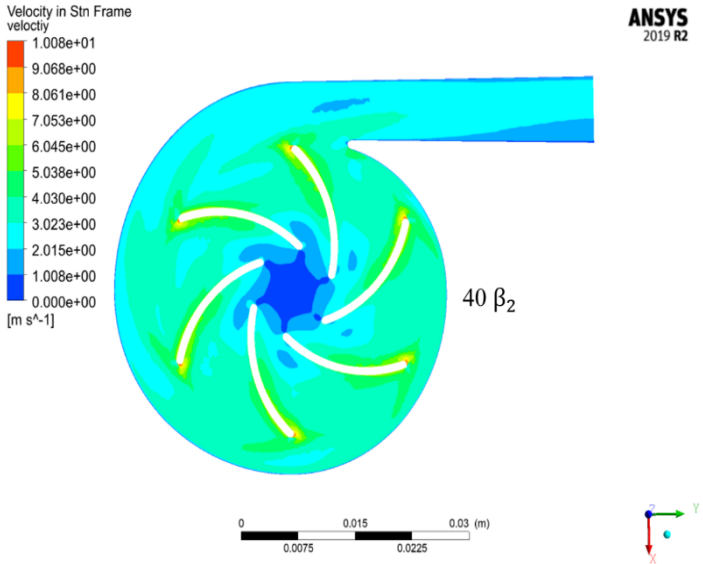

Figure C.2. Velocity profiles for different β_2 for up-clearance 2.00 mm at 5.8 L/min

APPENDIX D. PRESSURE PROFILES FOR DIFFERENT UP-CLERANCES

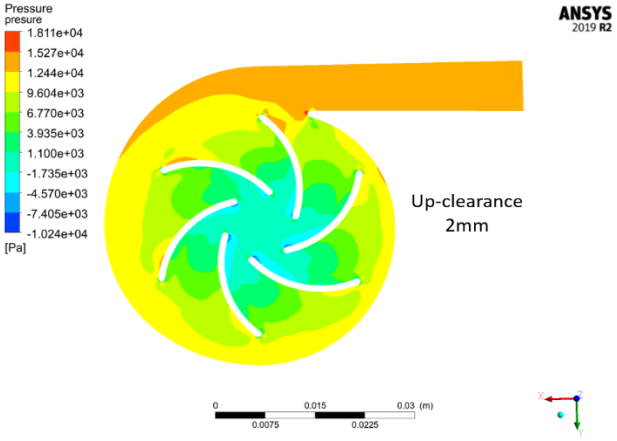

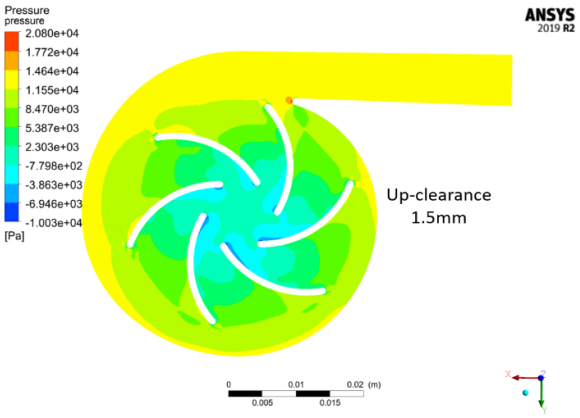

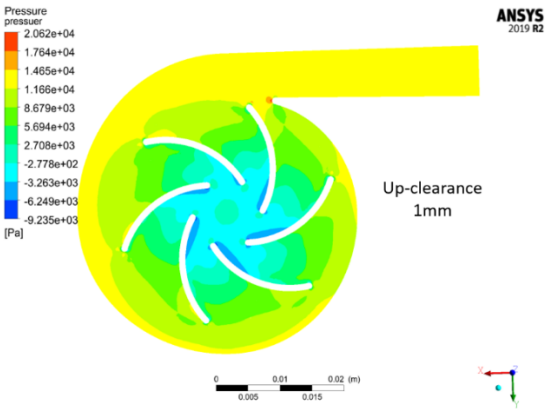

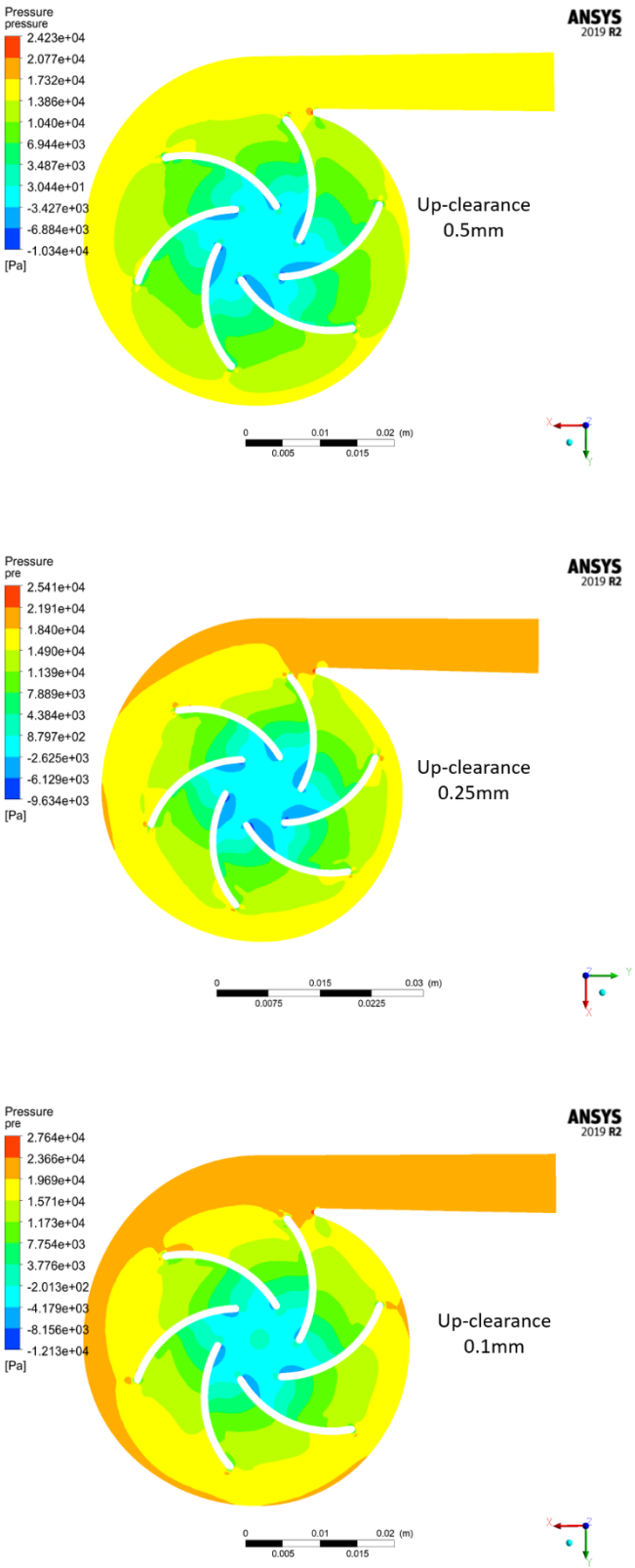

Figure D.1. Pressure profiles for different up-clearance for 35^0 β_2 at 5.8 L/min

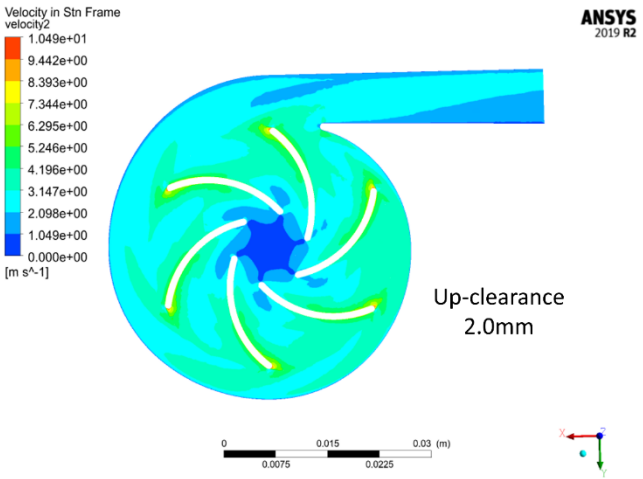
Velocity in Stn Frame
velocity2
1.049e+01
9.442e+00
8.393e+00
7.344e+00
6.295e+00
5.246e+00
4.196e+00
3.147e+00
2.098e+00
1.049e+00
0.000e+00
[m s^-1]
ANSYS
2019 R2
Up-clearance
2.0mm
0
0.015
0.03 (m)
0.0075
0.0225

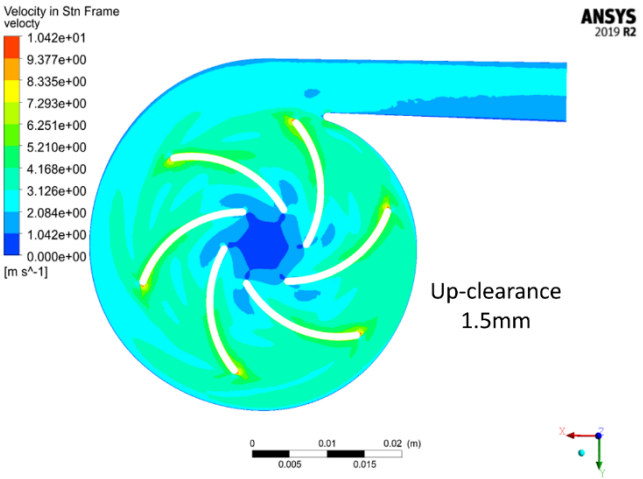
Velocity in Stn Frame
velocty
1.042e+01
9.377e+00
8.335e+00
7.293e+00
6.251e+00
5.210e+00
4.168e+00
3.126e+00
2.084e+00
1.042e+00
0.000e+00
[m s^-1]
ANSYS
2019 R2
Up-clearance
1.5mm
0
0.01
0.02 (m)
0.005
0.015

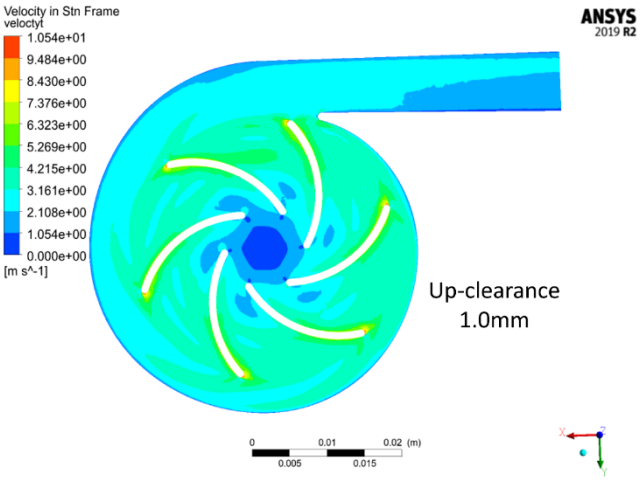
Velocity in Stn Frame
velocty
1.054e+01
9.484e+00
8.430e+00
7.376e+00
6.323e+00
5.269e+00
4.215e+00
3.161e+00
2.108e+00
1.054e+00
0.000e+00
[m s^-1]
ANSYS
2019 R2
Up-clearance
1.0mm
0
0.01
0.02 (m)
0.005
0.015

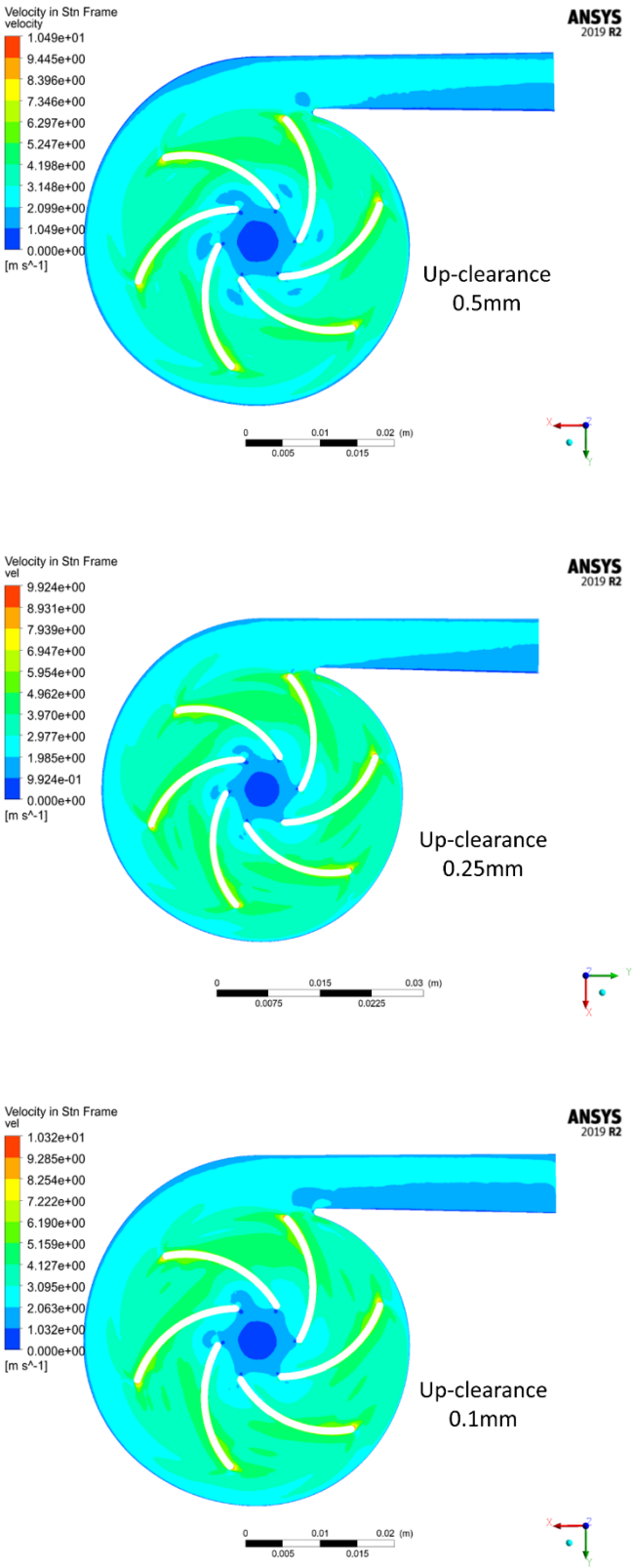

Figure D.2. Pressure profiles for different up-clearance for 35^0 β_2 at 5.8 L/min